THE DYNAMICS AND TOXICITY OF QUANTUM DOTS

THE DYNAMICS AND TOXICITY OF QUANTUM DOTS IN THE *CAENORHABDITIS ELEGANS* EMBRYO

By

SHYEMAA SHEHATA, B.Eng.Mgt

A Thesis

Submitted to the School of Graduate Studies

In Partial Fulfillment of the Requirements

For the Degree

Master of Applied Science

McMaster University

MASTER OF APPLIED SCIENCE (2009) McMaster University

(Biomedical Engineering) Hamilton, Ontario

TITLE: The Dynamics and Toxicity of Quantum Dots in the *Caenorhabditis Elegans* Embryo

AUTHOR: Shyemaa Shehata, B.Eng.Mgt (McMaster University)

SUPERVISOR: Professor C. Fradin

NUMBER OF PAGES: 105

ABSTRACT

Quantum dots are semiconductor nanocrystals with unique optical properties that give them the potential to be excellent probes for bio-imaging applications. However, before quantum dots can be employed for such applications, their toxicity and cellular interactions need to be thoroughly assessed. The *Caenorhabditis elegans* (*C. elegans*) embryo was chosen as a test environment to study both the toxicity and dynamics of carboxyl terminated CdSe/ZnS quantum dots. Using confocal imaging, it was found that the C. elegans embryo is not morphologically affected by the introduction of quantum dots up to a concentration of about 100nM. However, the embryo was observed to respond to the nanomaterial by packaging it into aggregates during development in a dose and time dependant manner. Image analysis and fluorescence correlation spectroscopy revealed that this packaging process happens from the nm scale to the μm scale and that it reduces quantum dot mobility over development. This work shows that the dynamics of the quantum dots are highly influenced by the cellular environment in the embryo, as they appear to aggregate and possibly also interact with cellular structures and organelles in the embryo.

ACKNOWLEDGMENTS

I am grateful to my supervisor Dr. Cécile Fradin, for her constant support and guidance, and for her gift of always being able to see the good in an experiment gone bad. Her patience and encouragement were so important in getting me through this project. Many thanks go to Dr. Bahgwati Gupta for always having his door open to enlighten me about the world of *C. elegans*. I am grateful to all of the members of the Fradin group for providing such a collegial and supportive research atmosphere. I especially benefited from the fruitful discussions that I had with Asmahan Abu-Arish and Felix Wong. I would also like to thank Ajit Thakur and Ashwin Seetharaman for the training that they provided me on *C. elegans* techniques. In addition, I am grateful to Tony Collin for the support that he provided for all of my imaging needs.

I am indebted to my parents for their continuous support and encouragement over the years. I thank my brother Zezo for always encouraging me to think critically, and also for being such an animated roommate for the last year. Finally, I would like to express my gratitude towards to my husband Mohamed for being both my greatest support pillar and my outlet for venting on difficult experiment days. Shoukran ya Mohamed for enduring with me this long separation so that I may complete my degree.

TABLE OF CONTENTS

Page

LIST OF TABLES

LIST OF FIGURES

Chapter 1 Background

1.1 Quantum dots

1.1.1 General properties of quantum dots

Quantum dots (QDs) are colloidal semiconductor nanocrystals that have core diameters ranging between about 1.5nm-6nm [1]. They are made from hundreds to thousands of atoms from the II-VI (e.g. CdSe, CdTe) or III-V groups (e.g. GaAs, InP) [1, 2]. QDs share some properties with their bulk counterparts, such as their ability to fluoresce. The ground state of both bulk semiconductors and QDs consists of a valence band fully occupied with electrons [3]. This band is energetically separated from a conduction band, as shown in Figure 1. If the nanocrystal absorbs a photon with energy greater than that which separates the two bands (the band gap), then the nanocrystal will become excited. This will cause an electron in the valence band to be promoted to the conduction band, leaving a hole behind in the valence band. The electron-hole pair is referred to as an exciton. When the electron recombines with the hole, it can emit a photon with a wavelength that is longer than that of the originally absorbed photon, thereby emitting fluorescence.

QDs also have properties that distinguish them from bulk semiconductors and that arise as a consequence of their 'smallness'. A nanocrystal only becomes a QD when its dimensions are smaller than the exciton Bohr radius, which is the physical distance between an excited electron and its corresponding hole in the bulk material [4]. Once a semiconductor nanocrystal makes this transition, it becomes governed by the physics of quantum confinement, and its fundamental properties change [5]. The band gap increases and the energy levels become discrete and size dependent, with smaller QDs having larger band gaps and therefore fluorescing at shorter wavelengths [4]. This size dependence is depicted in Figure 1.

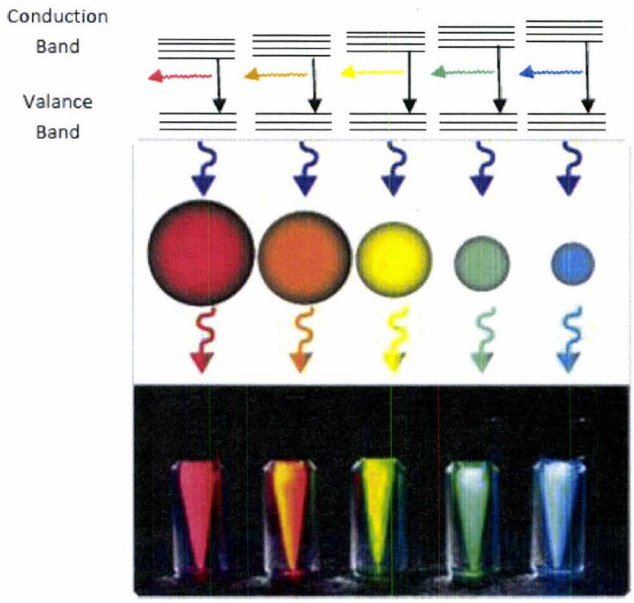

Figure1. A QD fluoresces when an electron in the conduction band recombines with a hole in the valence band. The emission wavelength of a QD is dependent upon its size. Adapted from [6]

The properties of QDs that arise from quantum confinement make them desirable candidates for a range of applications. In the field of optoelectronic, QDs are being employed in the development of solar cells, LEDs, and diode lasers [3]. Here we will focus on the applications of QDs in biotechnology and on the properties that make them good candidates for such applications. CdSe QDs are the most commonly used in bio-imaging because their emission bands span the entire visible spectrum [7].

1.1.2 Synthesis of quantum dots

QDs can be fabricated to emit from 400-1350nm (UV to infrared) by controlling their size and composition [8]. The size of QDs can be controlled by the fabrication time, temperature, as well as by the ligand molecules used for synthesis [8]. QDs are typically synthesized at high temperatures in non-polar organic solvents such as tri-n-octylphosphine oxide (TOPO) and hexadecylamine [4]. As a result of this procedure, the QDs are capped with a monolayer of the organic ligands in which they were prepared,

and therefore soluble only in nonpolar hydrophobic solvents. Further functionalizing layers can then be added to the QDs in order to make them water soluble. Water based synthesis has been shown that produces water soluble QDs with smaller hydrodynamic radii [9]. However, these methods are not as well developed as methods of synthesis in organic solvents.

1.1.3 Passivation of quantum dots

The optical properties of QDs depend strongly on the properties of their surface [3]. After fabrication, the surface of a semiconductor contains defects that can trap electrons and holes, preventing radiative recombination from occurring, and degrading the QDs' optical and electrical properties [5]. These defects can be minimized by coating the QDs with a passivating layer, resulting in a dramatic improvement of their optical properties. Passivation bonds the QD surface atoms to a material with a higher band gap, which effectively eliminates the traps. This introduces an abrupt jump in the chemical potential at the surface, thereby confining electrons and holes within the core [5]. ZnS is often used as a passivating layer for CdSe QDs, producing CdSe/ZnS (core/shell) QDs. One to two monolayers of ZnS can produce the highest improvements in optical properties, but thicker layers will offer the core better protection against oxidation [10].

1.1.4 Optical properties of quantum dots

One of the properties of QDs that are enhanced by passivation is photostability [8]. Photostabilty is one of features of QDs that make them such an attractive imaging candidate over organic dyes and fluorescent proteins. QDs are reportedly several thousand times more photostable than organic fluorophores [2]. In one study, QDs were illuminated continuously for 14 hours and were still fluorescent, while fluorescein completely photobleached in less than 20 minutes [11]. Similar findings were found when the photostability of QDs was tested against other dyes including Alexa Red, which is considered to be from a superior dye family in terms of photostability [12].

QDs also generally outperform organic dyes and fluorescent proteins in molecular brightness. This results from a combination of their high quantum yields and molar extinction coefficients. Molar extinction coefficients of QDs are about 10-100x that of organic dyes, and quantum yields can be as high as 90% [8, 10]. Their high molecular brightness makes QDs good candidates for single molecule studies, as well as for in vivo imaging, which suffers from attenuation due to scattering and absorption of light [2]. The two-photon absorption cross section of CdSe/ZnS QDs was also found to be two to three times more than that of conventional dyes, again making them useful for in vivo multiphoton imaging [13].

1.1.5 Emission and excitation spectra of quantum dots

The emission and excitation of organic fluorophores are dependent on the chemical structure of the fluorophore, and tuning them requires changing this chemical structure [9]. In contrast, the emission wavelength of a QD is controlled by its band gap, and so can be tuned by simply changing its size [8]. In addition, the molar extinction coefficient of QDs increases at shorter wavelengths, resulting in a broad absorption spectrum [14]. The emission of QDs is also characteristically narrow compared to that of organic dyes, with the full width half maximum (FWHM) of a single QD being as narrow as 13nm [14]. This allows for a large Stokes shift with easy separation of absorption and emission. In contrast, organic dyes generally have narrow absorption spectra and relatively broad emission spectra with a small Stokes shift [15]. Figure 2 shows a comparison of the spectral features of QDs and organic dyes.

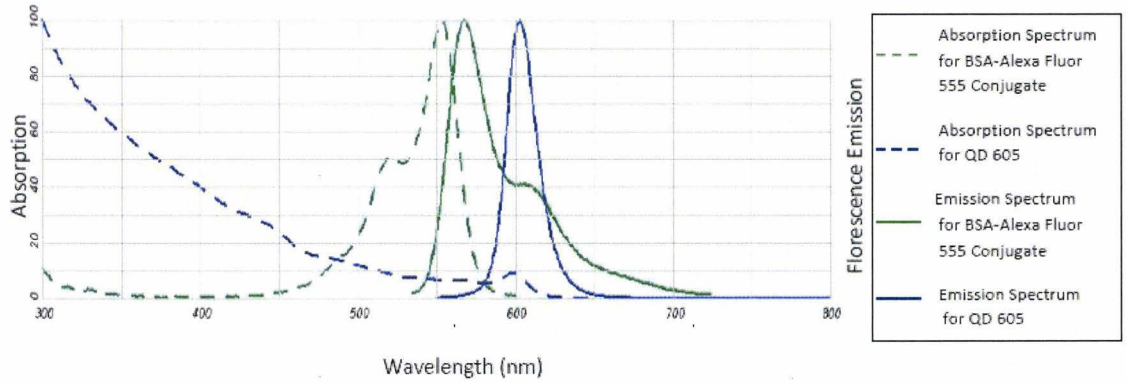

Figure 2. A comparison of the absorption and emission spectra of the organic dye fluorescein and CdSe/ZnS QDs. Adapted from [16]

The broad absorption spectra of QDs allows all QDs to be excited by a single wavelength [8]. This is in contrast to organic fluorophores that may need as many excitation sources as there are fluorophores. Their narrow well separated emission spectra allow several different colors of QDs to be used to distinguish between different biomolecules or processes [11], or for colocalization studies [8].

1.1.6 The fluorescence lifetimes of quantum dots

Another property that distinguishes QDs from organic dyes is fluorescence lifetime. The lifetimes of organic fluorophores are typically less than 5ns, and their decay can be described with a simple single exponential [15]. QD lifetimes are longer and have been reported to be between five and hundreds of nanoseconds. Although this allows for QDs to be easily temporally discriminated from background sources of fluorescence, such as autofluorescence (lifetime ~2ns), using time-gated measurements, their lifetime decay is typically multiexponential and is influenced by a host of parameters such as size, surface properties and wavelength [15, 17].

The lifetime of a QD decreases as its size increases [3]. Additionally, lifetime has been found to be dependent upon the QD emission intensity. At high intensities, it was found to be nearly exponential, while at lower emission intensities the lifetime was shorter and multiexponential.

The lifetimes of CdTe QDs have been investigated in a cellular environment by one group [18]. It was found that the QD lifetimes were dependent on the cell location. Lifetimes near the cell membrane were longer than lifetimes in endosomes or in the nuclear region of the cell. It was also discovered that QD lifetimes in the cell were shorter than in solution.

There is disagreement between studies about whether two, three or four exponential decay components are required to fit QD lifetime decays [14, 18-21]. So although all studies agree that the lifetime of QDs is longer than that of organic fluorophores, characterizing the lifetimes has proven to be challenging. It may only be practical to use lifetime multiplexing for distinguishing between the lifetime of a QD and an organic dye or background, but not for distinguishing between multiple QDs [15].

1.1.7 Quantum dot blinking

A final characteristic of QDs that will be discussed is blinking. Blinking describes the fluorescence intermittency of a fluorophore in which it switches between a bright fluorescent state and a dark state [22]. This phenomenon was first observed in QDs by Nirmal and colleagues [22]. It has been proposed that fluorescence intermittency is a result of surface traps at the QD surface [23].

A number of factors can influence blinking. Firstly, as described earlier, the effect of surface defects can be minimized by coating QDs with a passivating higher band gap material [24]. Organic molecule coatings have a similar effect of suppressing blinking [3]. Reducing environments [25], as well as inert gaseous environments [3], can also suppress blinking. In addition, minimizing excitation intensities has been shown to reduce the effects of blinking [24].

The distribution of times over which a QD exists in either a fluorescent or a dark state follows a power law distribution, with the consequence that blinking occurs over a very large range of time scales from 200μs to 100s [1, 26]. This is in contrast to organic

dye molecules which experience blinking due to trapping in a single dark state, such as a triplet state, resulting in exponential statistics.

1.2 Quantum dots for bio-imaging

1.2.1 Bio-imaging applications of quantum dots

The superior fluorescence properties of QDs make them attractive probes for bioimaging. Studies of QDs in biological environments have demonstrated that QDs are good fluorophores for immunofluorescence labeling of fixed cells, as well as for targeting cellular components such as nuclei, mitochondria, microtubules and actin filaments [8, 27]. We will consider now a few of the applications that have exploited QDs' unique optical properties. These include applications for which QDs were used to track the motion and dynamics of single molecules, to applications involving QDs for potential diagnostic and therapeutic purposes.

1.2.1.1 Quantum dots for single-cell studies

One study has highlighted the advantages of using lifetime imaging for QDs [19]. Silanized CdSe/ZnS QDs were incubated with mouse fibroblasts and imaged using lifetime imaging. It was shown that in comparison to standard confocal imaging, lifetime imaging allowed enhanced signal to noise, eliminating autofluorescence.

Nuclear transport with QDs has been demonstrated [28]. Homemade silanized CdSe/ZnS QDs were conjugated to a nuclear localization signal (NLS) through a streptavidin-biotin bridge and were successfully targeted to the nucleus. The entire QD-NLS complex was 15-20nm. It was also observed that QDs conjugated to non-NLS peptides were excluded from the nucleus. These results encourage the possibility of exploiting QDs' resistance to photobleaching for single particle tracking of NLS conjugated QDs.

The brightness and photostability of QDs have provided researcher with a new tool for single molecules investigation. QDs have allowed the dynamics of membrane [8]

and neurotransmitter [29] receptors, as well as kinesin motors [29], to be studied with single molecule sensitivity. The motion of QD labeled nerve growth factor was studied with much greater detail than was allowed previously by organic dye labeling [30]. These studies also showed that blinking can be exploited as a means of distinguishing single QDs from aggregates [29].

1.2.1.2 Quantum dots for diagnostic and therapeutic applications

The potential of QDs for in vivo imaging has been demonstrated. In one study, QDs with four different coatings were injected into mice for noninvasive imaging of superficial vasculature as well as of the liver and bone marrow [31]. Circulation times as well as localization were found to be dependent on the coating. QDs with a high molecular weight coating of polyethylene glycol (PEG) circulated for longer and had reduced accumulation in the bone marrow and liver.

QDs such as CdTe may become a fluorophore of choice for near infrared (NIR) deep tissue imaging. Imaging in the NIR region allows for greater penetration depths to be achieved with minimized tissue scattering and absorption [9]. There is currently only one clinically approved organic fluorophore, ICG, that operates in the NIR, but it has low quantum yield and is found to bind to plasma proteins [15]. CdTe QDs have superior quantum yield and a large two-photon action cross-section in this emission region [15]. One study demonstrated their use in deep in vivo multiphoton imaging to study the vasculature and adipose tissue of mice [13]. Imaging with these QDs allowed blood flow velocities to be measured and the heart rate to be detected.

The ability of QDs to target specific tissues in-vivo has been investigated by a number of studies for both diagnostic and therapeutic purposes. Peptides conjugated to QDs have been successfully targeted to the lung, blood and lymphatic vessels in mice [32]. Tumor cells often express cell surface markers that are absent or limited on healthy cells [17]. QDs can be conjugated to antibodies that specifically target these antigens to tumor cells. This has been demonstrated in-vitro with breast cancer cells [8], as well as

in-vivo in mice with prostate cancer [33]. Other studies have shown that imaging QDs at these targeted sights can aid in surgical removal of tumors. It was suggested that in addition to diagnostics agents, therapeutic agents can also be loaded on the same QD [33]. These studies also found that coating with high molecular weight polymers prevents non-specific uptake [32, 33].

It has also been proposed that QDs could be used for photodynamic therapy (PDT) [34]. PDT is a type of cancer therapy in which light is used to excite a photosensitizer, which transfers its triplet state energy to oxygen molecules, which form reactive singlet oxygen, leading to apoptosis of the cell. QDs have been proposed as a potential delivery system for photosensitizers. It was shown that QD based FRET can be used a means to excite the photosensitizer. Using QDs as the initial absorber allows a greater range of excitation wavelengths to be used. Additionally, it was found that the QDs themselves were able to produce singlet oxygen, and ao could potentially itself act as a photosensitizer.

1.2.2 The challenges of using quantum dots for bioimaging applications

1.2.2.1 Making quantum dots biocompatible

In order to make QDs eligible for the applications just discussed, they must first be solubilized. Organic dyes are generally soluble, while achieving this is more challenging with QDs [15]. Although methods of producing CdTe QDs generally yield water soluble QDs, CdSe QDs are usually synthesized in organic solvents, and so need to be made water-dispersible [15]. Methods to do this include exchanging their hydrophobic ligands with hydrophilic ones such as thiol-containing molecules, oligomeric phosphines, dendrons or peptides [8]. Alternatively, the hydrophobic QD can be encapsulated within a layer of amphiphilic diblock or triblock copolymers, or within silica shells, phospholipid micelles, polymer shells, or amphiphilic polysaccharides [8]. Some of the most effective coatings used for commercial QDs, such as phospholipid or

block copolymer coatings, have the undesirable effect of increasing the QD size from 4-8nm to 20-30nm [10].

In addition to making QDs water-dispersible, these solubilizing agents allow the QD to be further attached to biomolecules, which would allow them to target specific markers at the cell, tissue or organ level [9]. Methods of attaching organic fluorophores to biomolecules such as proteins or peptides have been well established. However, there are only a few well known methods of coupling QDs to biomolecules, and they are very much dependent on the QDs' surface functionalization [15]. QD solubilizing agents are often designed to have reactive groups on their surface that can be conjugated to biomolecules, such as carboxyl ($COOH^-$), and amine ($-NH_2$) groups [17]. Binding can also be achieved using an electrostatic bond consisting of biotin-avidin interactions [15]. Alternatively, it can be done covalently, for example, between amine and carboxylic groups. Another method is to directly exchange the surface ligand formed during QD synthesis with the biomolecules of interest. 10-15 linker molecules can be attached covalently or electrostatically to a QD [11]. After coating and conjugation, a QD could be 3 to 4 times the size of the original QD [17], and be comparable to a protein that is 500-750kDa [11]. Compare this to the size of green fluorescent protein (GFP), which is only about 25kDa.

As a result of their relatively small size (~0.5nm), several organic fluorophores can be attached to a single biomolecule of interest without having a significant effect on the biomolecule's function [15]. In contrast, owing to its bulky size, several biomolecules can be attached to a single QD, as depicted in Figure 3. This may interfere with the biomolecule's function [15]. QD bulkiness may also make them less accessible to some locations in the cell.

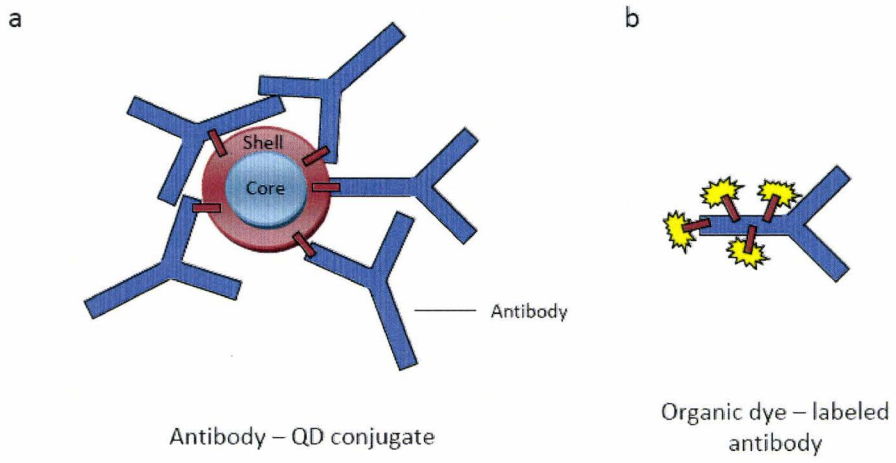

Figure 3. (a) a single QD can be conjugated to several targets; (b) several organic fluorophores can be attached to a single biological target. Adapted from [15]

1.2.2.2 Introducing quantum dots into cells

Intracellular delivery of QDs offers another challenge, again as a result of their size and tendency to aggregate. An early study found that QDs solubilized with mercaptoacetic acid (MAA) and incubated with HeLa cells were not taken up by the cells [24]. Similar results were found in another study that incubated carboxyl coated QDs with NIH 3T3 cells [35]. However, in both of these studies, when the QDs were conjugated to cell binding moieties, transferrin in the first case and Cholera toxin B in the second case, QDs were successfully taken up through receptor-mediated endocytosis.

Nevertheless, in other studies, simply incubating QDs with cells was enough to induce them to take them up through nonspecific endocytosis. For instance, when silanized CdSe/ZnS QDs (10-100nM) were incubated with mouse fibroblasts, QDs were taken up by cells and appeared as aggregates in the cytosol [19]. It was surmised that the QDs were taken up by cells via endocytosis and perhaps stored in lysozomes. In another study QDs coated with dihydrolipoic acid and incubated with cells were found to be taken by the cells in vesicles, presumably again by endocytosis [36].

In the case of receptor mediated endocytosis, it appears that the type of cell binding moiety conjugated to the QD can cause varying degrees of aggregation. For

instance, one study showed that when QDs were conjugated to the cell binding moiety polyarginine, QDs were taken up by endosomes as large aggregates. The QDs were not uniformly distributed between daughter cells [35]. However, when Cholera toxin subunit B was conjugated to the QDs, they were well dispersed, despite also being contained in vesicles.

Electroporation is another technique that has been shown to introduce QDs into the cell. Although one study claimed that electroporation prevented the aggregation of QDs, [28], other studies have shown otherwise [37]. Studies with *Xenopus* and zebrafish embryos used microinjection to introduce QDs [38, 39]. These studies established that QDs may be useful for cell-lineage studies, as well as a means of studying vasculogenesis. A single study has employed a different cell loading technique based on the osmotic lysis of pinocytic vesicles, which prevents the QDs from being trapped in endosomes [40].

Of all of these techniques, microinjection appears to be the most reliable way to introduce QDs into a cell without having them end up in vesicles [8]. However, this is also the most time consuming technique, as each cell has to be individually microinjected. More work is needed in order to develop better techniques to target specific intracellular structures, without having the QDs become endocytosed into vesicles.

1.2.2.3 Other challenges of imaging with quantum dots

A number of these studies have also uncovered other challenges associated with imaging with QDs. Loss of QD fluorescence upon injection into tissue has been observed and attributed to degradation of the surface, or to nonspecific adsorption onto the surface [41]. Solubilization and bioconjugation may also decrease the quantum yield of QDs [15]. The cellular environment itself can affect the stability and photophysical properties of QDs [42]. The extent to which the environment will change a QD's fluorescence properties depends strongly upon how accessible the QD surface is.

Aggregation has been found to be another major obstacle in working with QDs. QDs are susceptible to irreversible aggregation, which could result from long-term storage, changes in pH, heating or freezing [11]. QDs also have a tendency to aggregate with increasing ionic strength [15]. Susceptibility to aggregation can also depend very much on the surface coating of QDs. For instance, MAA was found to desorb from QD surface and cause QD aggregation and precipitation [9]. Coating QDs with high molecular weight polymer coatings has consistently been found to reduce aggregation, but at the cost of increasing their bulkiness.

1.3 The cytotoxicity of quantum dots

If QDs are to be employed in diagnostic and therapeutic applications, their potential toxicity must first be thoroughly investigated. This is one aspect of QDs for which no clear conclusions have been made. Such toxicity may result from a number of sources. (1) Firstly, their nanometer size could be a source of toxicity, allowing them to be ingested by cells, or to stick to their membranes [43]. (2) Another often cited argument is that QDs have an enhanced surface-area to volume ratio compared to their bulk counterparts, which can make them more susceptible to releasing their core contents [43]. (3) The composition of QDs is another major toxicity concern. The most commonly used QDs have cadmium at their core. Indeed, Cd^{2+} is known to be toxic to a variety of cells and is in fact a suspected carcinogen [17]. Corrosion of the CdSe core, for instance, may cause the release toxic ions, resulting in apoptosis [44]. In fact, bulk cadmium oxide, well known for its cytotoxic properties, has been used as a positive control in toxicity studies [45]. Cadmium has a half life of 20 years in humans and there is no known mechanisms for the body to get rid of this element [17].

A number of investigations have looked into the issue of toxicity. The majority of these studies have considered the effects of QDs on cell cultures. There are a few groups that have investigated the effects of QDs on embryo development. Some have also used murine models to study toxicity. Some of these studies will be reviewed here, in order to give the reader an idea of the range of results on toxicity that have been found.

1.3.1 In vitro studies

1.3.1.1 Toxicity Markers

The simplest method to assess toxicity in cells is by visual inspection. However, more objective colorimetric methods are also available [46]. These methods include tests of plasma membrane integrity or mitochondrial function, both of which are measures of the health of a cell. The release of certain chemicals such as lactate dehydrogenase (LDH) can indicate cell damage. Oxidative stress levels in a cell can be assessed with glutathione assays. There are also assays that determine whether cells are dead or alive based on the presence of certain chemicals that only exist in healthy cells, as well as on membrane integrity. Inflammation is sometimes used as an indication of toxicity, and can be measured using enzyme-linked immunosorbant assays (ELISA). Flow cytometry can be used to determine if cells have undergone apoptosis based on cell shrinkage and chromatin condensation.

A range of cell types have been used to test QD toxicity, although in most cases no reason is given for the choice of cells used. One study justified its use of primary hepatocytes to study QD toxicity by stating that the liver is a major target of cadmium accumulation [47].

1.3.1.2 Influence of a passivating layer on toxicity

In addition to enhancing the optical properties of QDs, passivation has also been found to protect the QD core from degradation. Passivating CdSe QDs with ZnS was found to dramatically reduce toxicity, almost eliminating it in some cases [43, 47, 48]. All of the studies that found that QDs induced no toxicity used CdSe QDs passivated with ZnS [19, 28, 35, 36].

1.3.1.3 Influence of hydrophilic surface coating on toxicity

Although passivation has been found to be the most dramatic method of reducing toxicity, the choice of the solubilizing layer also has an impact on toxicity. The addition of bovine serum albumin (BSA) has been found to reduce toxicity of both passivated and unpassivated QDs [47, 49, 50]. In general, the use of short solubilizing ligands has been found to offer less protection than high molecular weight coatings such as PEG [43, 50, 51]. In some cases it was reported that the reduced toxicity of QDs coated with high molecular weight polymers was a result of reduced uptake into the cell, rather than a result of additional protection offered inside the cell.

1.3.1.4 Influence of dose on toxicity

It can be difficult to compare doses between studies due to the different units used to report them. However, within studies toxicity has been found to be dose dependant. This has been found to be true for both unpassivated CdSe [43, 47] and CdTe [49] QDs, as well as for CdSe QDs passivated with ZnS [43, 50, 52] and CdS [51]. One study observed apoptosis to occur at low QD doses, with necrosis occurring at higher doses [43].

1.3.1.5 Influence of size on toxicity

The effects of QD size on toxicity are not yet well understood. Some studies have found that smaller CdSe/ZnS QDs are more toxic than larger ones, [52], while others have found the opposite to be true [50]. A study with CdTe QDs concluded that smaller QDs were more toxic and attribute this to the difference in distribution of large and small QDs inside the cell [49]. Larger QDs showed punctuate distribution in the cytoplasm and binding to the cell surface, but were not present in the nucleus, while smaller ones were found predominantly in the nucleus.

1.3.1.6 Sources and Mechanisms of inducing toxicity

Most studies that found QDs to be toxic attributed this toxicity to the release of Cd^{2+} from the QD core [43, 47, 49, 51], possibly leading to the binding of Cd^{2+} to sulfhydryl groups of mitochondrial proteins [47]. It has been speculated that this release could be caused by the acidic and oxidative environment of the lysosome, in which QDs are generally taken up into the cell [51]. Such conditions have been observed to cause a blue shift in QD emission, indicating core degradation.

Precipitation of QDs on the surface of cells has been found to be another source of toxicity at high QD concentrations [43]. Additionally, it has been speculated that the QD solubilizing coating may be a source of toxicity[50, 52]. One study found that carboxylic acid coated QDs promoted pro-inflammatory cytokine release while PEG coated QDs did not [50]. However, in this case it is not clear if toxicity resulted from the actual coating, or from the reduced protection offered by carboxylic acid compared to PEG.

Some studies have tried to elucidate the mechanisms of toxicity caused by Cd^{2+} release from QDs. One of these observed that CdTe QDs caused a loss of plasma membrane integrity, which is associated with late apoptosis or early necrosis [53]. Additionally, aggregation of mitochondria and breakdown of the tubular mitochondrial network were observed, also associated with death by apoptosis. Nuclear deformation and shrinkage was also detected, again indicative of apoptosis. QDs were also found to stimulate the release of cytochrome c from mitochondria, a known amplifier of apoptotic signals. It was concluded that CdTe QDs induced non-classical apoptosis caused by reactive oxygen species, presumably through electron or energy transfer to nearby oxygen molecules.

Similar conclusions were reached in another study with CdSe QDs [48]. It was shown that the QDs induce apoptotic markers such as c-Jun N-terminal kinase activation, loss of mitochondrial membrane potential, mitochondrial release of cytochrome c and activation of caspase-9 and caspase-3 in cell culture. Reactive oxygen species production

was increased. In addition, anti-apoptotic survival signaling was inhibited. However, when CdSe QDs were passivated with ZnS, these apoptotic markers were not detected.

1.3.1.7 Counteracting the toxic effects of quantum dots

The effects of the antioxidants N-acytlcycteine (NAC) and Trolox on QD toxicity was investigated in cells exposed to CdTe QDs [49]. Trolox was found to be ineffective, but NAC was successful at reducing toxicity. Treating cells with BSA also provided protection. It was suggested that NAC may be adsorbing to QD surface, thereby minimizing oxidation, or that it could be initiating anti-apoptotic pathways. BSA, which has metal binding sites, could be preventing toxicity by binding to cadmium ions.

1.3.2 Developmental Studies

Only so much can be concluded from in vitro toxicity studies. Although they may be useful for elucidating the mechanisms by which a single cell will respond to an environmental insult, these studies do not reflect the complex interactions and responses of an organism. In vivo studies can more realistically reveal how QDs are be absorbed, distributed, metabolized and excreted [54]. A number of studies have looked at this, including some that have studied the toxicity of QDs on embryos. In one of these studied, QDs were encapsulated in phospholipid block-copolymer micelles and microinjected into *Xenopus* embryos [38]. It was found that the QDs could be still be imaged at the tadpole stage with no obvious aggregation of QDs. At early stages, QDs were quite evenly distributed in cells, but at later stages they concentrated in the nucleus. No toxicity was observed at injections concentrations of $2*10^9$ QDs/cell. However, when injections introduced more than $5*10^9$ QDs/cell, abnormalities started to become apparent. It was posited that it may have been due to changes in osmotic equilibrium of the cell.

Another study investigated the effects of streptavidin conjugated CdSe/ZnS QDs on the development of zebrafish embryos [55]. 1.7nL of 100nM QDs were injected into

one cell at the two-cell stage. At injections of 100nM, about 85% of embryos were viable. At 200nM injections, this reduced to 73%.

The mouse embryo has also been used as a model to study the toxicity of CdSe QDs. [56]. Early fertilized embryos were incubated with mercaptoacetic acid solubilized QDs for 24hrs. At QD concentrations of 125nM or higher, fewer embryos developed to advanced stages in a dose dependent manner. Of those that did develop, fetal weight was lower. It was found that at 250nM and higher, the CdSe QDs induced apoptosis in blastocysts cells and reduced cell proliferation in a dose-dependent manner. Again, QDs passivated with ZnS were not toxic, suggesting that the release of Cd^{2+} was responsible for toxicity, possibly by promoting the production of reactive oxygen species.

1.3.3 Mouse models

A number of other studied have also used the mouse model to investigate toxicity. These studies have shown that injected QDs tend to deposit in the liver, bone marrow, lymph nodes, kidney, spleen and lungs [31, 32, 46, 57]. However, QD encapsulation with high molecular weight coating reduces nonspecific uptake of QDs by organs [31, 32]. Some of these studies reported that QDs were not detected in the in feces or urine, suggesting that they are not being excreted by the animals [46, 58] . However in one study, an increase of porphyrins was detected in the urine, which is a measure of oxidative stress [58]. Tissue analysis has revealed that QDs localize in the endomsomes of the mice [31, 46]. In one of these studies QDs remained present and fluorescent in mice for at least four months in the liver and lymph nodes [31]. Although this study reflects QDs' exceptional optical properties, it also brings to attention the problem of ridding the body of the QDs once their therapeutic or diagnostic role has been carried out.

1.3.4 Conclusions

The results of these studies are varied, with some concluding no toxic effects, while others observing adverse responses to the foreign nanomaterial. How does one

reconcile the wide spectrum of results? Comparing results from different studies is difficult because of the diverse experimental conditions used. For instance, some of the studies used commercially available QDs, while others fabricated their own in-house. A large range of coatings were used, and QD concentrations used have been reported in various units that are sometimes difficult to compare.

However, some general conclusions can be drawn from these studies. Firstly, toxicity is generally dose dependant, and its major source appears to be the release of Cd^{2+} caused by enzymatic or chemical degradation. Cd^{2+} seems to do its harm by initiating apoptotic pathways, leading to DNA damage, protein damage and loss of membrane integrity. Surface chemistry has a significant impact on toxicity. In addition to enhancing the optical properties of QDs, capping with ZnS has consistently been shown to have the secondary effect of dramatically reducing toxicity. Adding additional solubilizing layers can further reduce toxic effects, with thicker coatings generally offering more protection. Size does appear to play a role as well, as smaller QDs can access more locations in the cell. A major issue that still needs to be addressed is whether or not any of these biological systems have methods of metabolizing and eliminating QDs. The use of potentially less toxic III-V QDs has been considered [9]. However, so far their fabrication is arduous and they have lower quantum yields.

1.4 *Caenorhabditis elegans*

1.4.1 The anatomy of *Caenorhabditis elegans*

Caenorhabditis elegans (C. elegans) is a free living transparent nematode [59]. An adult *C. elegans* is about 1mm in length and can either be hermaphrodite or male [60]. A diagram of an adult *C. elegans* hermaphrodite is shown in Figure 4.

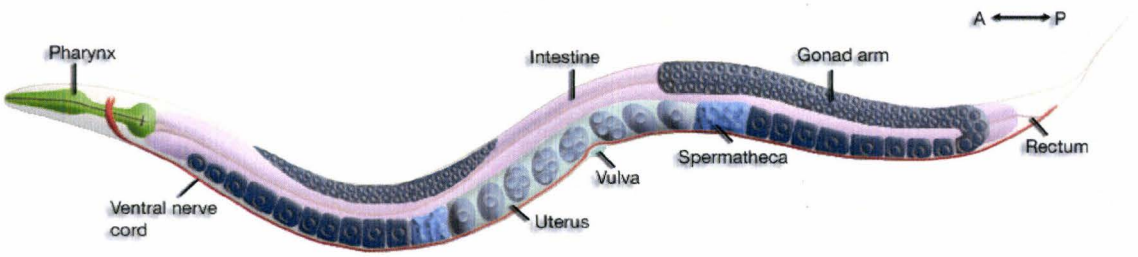

Figure 4. An adult *C. elegans* hermaphrodite [60]

Each adult hermaphrodite has two U-shaped gonad arms that are connected to a uterus via two spermatheca [60]. Germline nuclei surround a central core of cytoplasmic material in these gonad arms. At the gonad loop region, germline nuclei become enclosed by a plasma membrane and are part of an assembly line of oocytes awaiting fertilization [61]. A DIC image depicting this is shown in Figure 5.

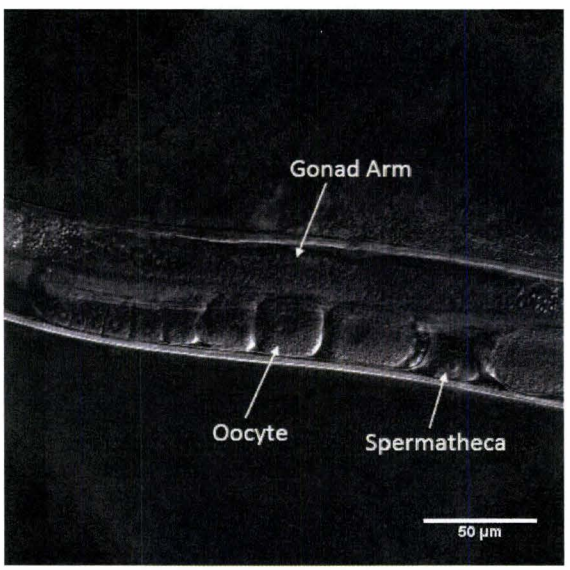

Figure 5. Oocytes form out of the gonad arm in an assembly line and are fertilized in the spermatheca

As each oocyte travels through the gonad arm, it matures. Oocytes are moved along by the contraction of smooth muscle-like cells called gonadal sheath cells [61]. These cells form gap junctions with the oocytes and are involved in the regulation of their maturation and ovulation. As the oocytes grow, they accumulate yolk lipoprotein particles through receptor-mediated endocytosis, and store them in membrane-bounded granules [61]. Oocyte meiotic maturation involves nuclear envelope breakdown,

rearrangement of the cortical cytoskeleton and meiotic spindle assembly, as well as reorganization of the organelles [62]. The different aspects of oocyte maturation are coordinated through intercellular signals.

Sperm associated signals are involved in promoting oocyte fertilization. At ovulation, the largest most proximal oocyte enters the spermatheca and undergoes fertilization [61]. This occurs through contraction of the gonadal sheath cells and dilation of the spermatheca, which pulls the spermatheca over the most mature oocyte. Fertilization occurs in the spermatheca when the spermatozoa and oocyte recognize each other, bind and fuse. This repeats about 23 minutes. Every 6.5 hours a complete turnover of the entire volume of the gonad arm occurs.

1.4.2 Embryogenesis in *C. elegans*

After fertilization, an eggshell is formed that offers protection to the egg [63]. Cell-cell communications are heavily involved in determining the cell fates. A cell may send signals to another cell that determine its polarization or that alter its fate in other ways. Asymmetric cell divisions ensure that daughter cells are formed with different amounts of regulatory molecules and that they therefore have different developmental fates.

The stages of development are summarized in Figure 6. The first cell division occurs about 40min after fertilization [60]. During the first 150min, cell divisions occur to form what are known as the embryonic founder cells. At this stage, approximately the 28-cell stage, the eggs are laid outside the mother. From about 150 to 350min cell divisions continue and gastrulation takes place. At the end of this the embryo is organized into the three germ layers that will give rise to different organs [60]. Morphogenesis begins at the bean stage. The embryo elongates and forms differentiated tissues and organs. Embryogenesis generates 671 cells [59]. In the hermaphrodite, 113 of these undergo apoptosis and the rest differentiate. 12 to 14 hours after fertilization, the worm hatches [60]. It goes through four larval stages before becoming an adult [59].

Approximately 50hrs after hatching, a hermaphrodite will complete the cycle, laying its 1st egg and will continue to do so for 3 to 4 days [60]. A hermaphrodite will produce 300 eggs without mating, but mating will allow it to produce 1200 to 1400 eggs.

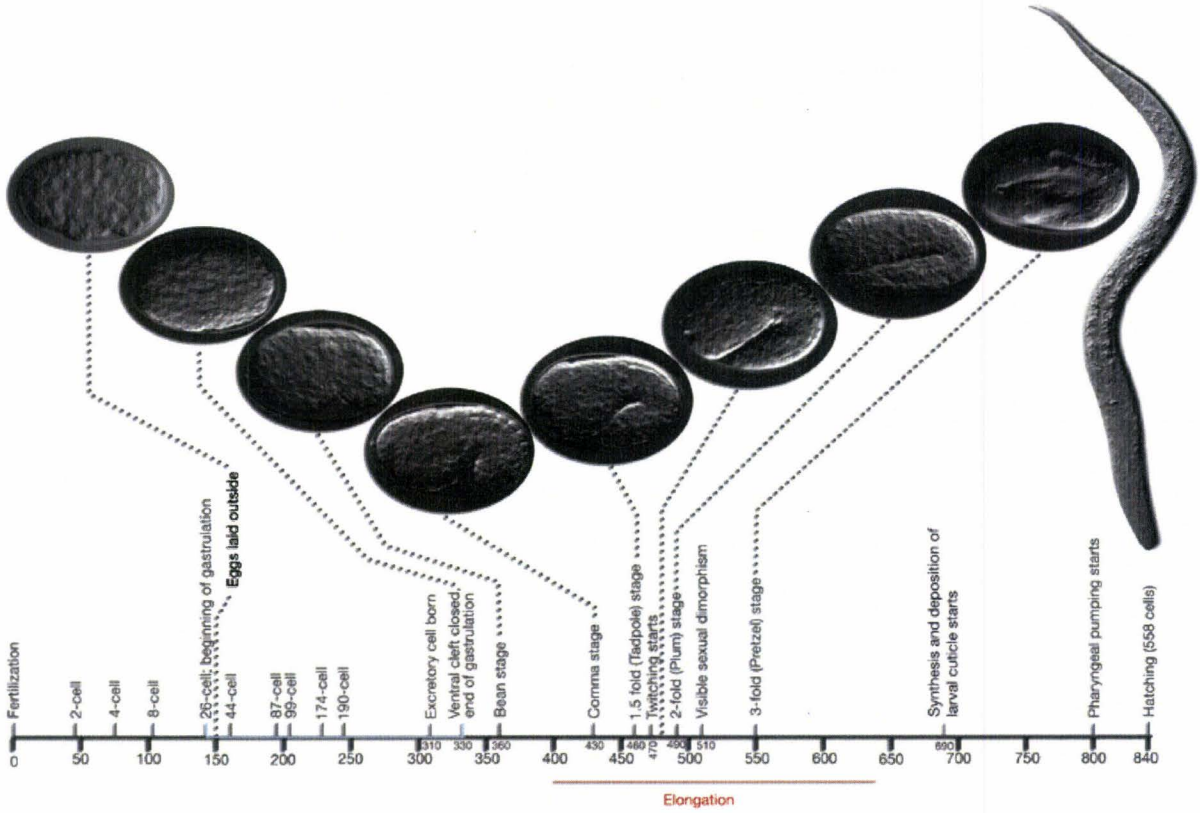

Figure 6. Various stages of embryogenesis and their corresponding time after fertilization in minutes. Adapted from [60]

1.4.3 *C. elegans* as a model organism for toxicity studies

C. elegans has proven to be an important model organism for studying molecular and developmental biology since Brenner introduced it as such in the 70's [64]. It has led to discoveries in the fields of neuroscience, RNA interference and cell death, to name a few. It has been used to study neurodegenerative disorders include Parkinson's Alzheimer diseases [65].

There are a number of features that makes this nematode both a relevant and practical model organism in general [65]. About 99.95% of them are hermaphrodites that produce 300 or more progeny over their short life cycle of about 3 days. These nematodes are also inexpensive and easy to maintain. Their small transparent bodies allow for easy observation of cells. The *C. elegans* genome has been completely sequenced, and its entire cell lineage is known. Genetic techniques such as mutagenesis, transgenesis and RNA interference are well established for *C. elegans*, allowing it to be studied at the molecular level. Transgenic worms are easy to generate that allow the effects of single genes to be understood.

Would toxicity studies in *C. elegans* be indicative of effects in higher eukaryotes? Evidence exists that would suggest that the results of toxicity studies in *C. elegans* do have value in predicting toxicity in humans [65]. This is based on similarities in genetics, physiology and on actual results from toxicity studies. *C. elegans* homologues have been found for 60-80% of human genes. Furthermore, many stress responses that occur in humans are conserved in *C. elegans.*

A number of signal transduction pathways are conserved in both *C. elegans* and vertebrates [65]. Some of these that are relevant for toxicity studies include apoptosis and the oxidative stress responses. Genes and pathways that are involved in DNA repair in mammals are in general also well conserved in *C. elegans* [65]. This has led to the use of *C. elegans* as a model for studying the effects of toxicity on DNA damage, as well as processes associated with DNA damage. Electrophysiology studies on both live worms and cultured worm neurons have determined that *C. elegans* neurons and vertebrate neurons respond similarly to a number of drugs, triggering its use a model for studying the effects of pesticides on neurological pathways [65].

The *C. elegans* model has also been used to investigate the toxicity of a number of heavy metals including cadmium and arsenic. Studies have found that exposure to Aluminum and Lead reduce worms' learning abilities [65]. The antioxidant Vitamin E was able to reverse these effects, suggesting that oxidative stress was involved in

inducing toxicity. Others have suggested that toxicity may be caused by the replacement of essential metals on protein active sites by toxic metals [66].

Growth, reproduction, and mortality were all found to be affected to varying degrees by lead, cadmium, chromium and arsenic [67]. Metals including lead and cadmium were found to impair worm locomotion [68]. Some studies have investigated the ability of worms to adapt their behavior to the presence of toxins. One of these made plates with a concentration gradient of different heavy metals. It was found that worms were able to somehow detect and avoid the presence of cadmium and copper, but not nickel [65].

To understand how worms are able to avoid certain toxins, GFP has been expressed in neuron populations. Using this technique, it has been found that the genes responsible for resistance to cadmium were upregulated in worms exposed to cadmium [65]. Other studied have found similar results. When transgenic worm lines that expressed stress-genes coupled to GFP were exposed to a number of heavy metals, it was found that only cadmium exposure increased expression levels of these stress related genes, and only at high concentrations [67]. This suggests that *C. elegans* has defense mechanisms in place involving these stress-genes that specifically helps prevent damage by Cd. These types of findings have prompted some investigators to attempt to produce a *C. elegans* strain that is supersensitive to heavy metal toxicity, and that can act as a bioindicator to heavy metals [66].

1.5 Fluorescence Correlation Spectroscopy

1.5.1 Introduction to fluorescence correlation spectroscopy

Fluorescence correlation spectroscopy (FCS) is a technique that converts spontaneous temporal fluorescence fluctuations from fluorophores into useful information about the underlying molecular process [69]. Such fluctuations are generally considered to be unwanted noise, but useful information about the dynamics of fluorophores can be derived from them [70]. In principle, any physical process that

creates fluorescence fluctuations can be characterized by FCS. Access to these processes is obtained by temporally autocorrelating the fluorescence signal [70]. The autocorrelation function basically looks for patterns in the fluctuations and quantifies them. The main parameters that can be characterized by FCS are mobility coefficients, concentrations, molecular brightness, the rates of chemical reactions, as well as the characteristic times of photophysical processes [71]. FCS has the potential to identify processes that have characteristic times ranging from nanoseconds to a few seconds.

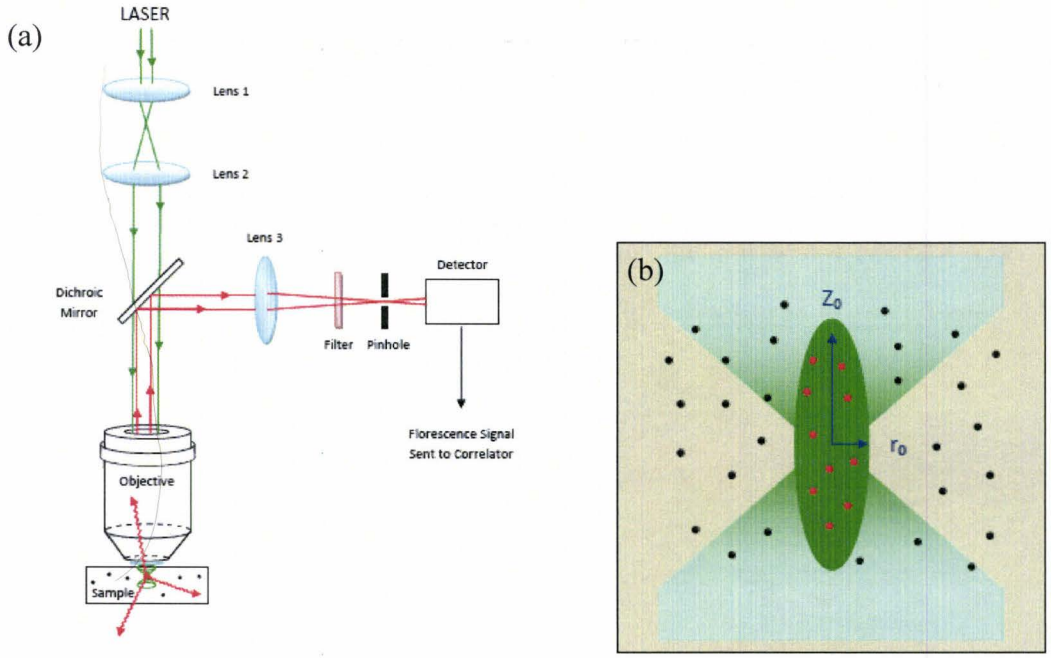

Figure 7. (a) A typical FCS setup adapted from [72]. (b) The focal volume with excited fluorophores

An example of an FCS setup is shown in Figure 7. FCS employs a confocal microscope with a high numerical aperture objective. Laser light is focused on a diffraction limited spot that has a volume of about one femtoliter. The laser can be focused on a solution or a cell for instance. This setup allows just a few fluorophores to be illuminated within the confocal volume. Limiting the number of particles in the detection volume is important for suppressing background noise [73].

As depicted in Figure 7, the excited sample emits fluorescence that is collected by the same objective and then reflected by a dichroic mirror, which provides some separation between excited and emitted fluorescence. Next, the fluorescence is focused

and sent through an emission filter that ensures that no excitation light is collected. The focused light passes through a pinhole which provides axial resolution by eliminating any out of focus light that does not originate from the observation volume. After being detected, the fluorescence is sent to a correlator that computes the autocorrelation curve.

1.5.2 The autocorrelation function

Mathematically, the autocorrelation (AC) function correlates the intensity signal at time t, F(t), with the signal after a short time τ has passed, F(t+τ) [72]:

$$G(\tau) = \frac{\langle \delta F(t) \cdot \delta F(t+\tau) \rangle}{\langle F(t) \rangle^2} + 1$$

In Equation 1, δF(t) is the fluctuation in F(t) about the mean value <F(t)> such that $\delta F(t) = F(t) - \langle F(t) \rangle$. A typical fluorescence signal that may be collected by a detector is shown below in Figure 8, along with its corresponding AC curve.

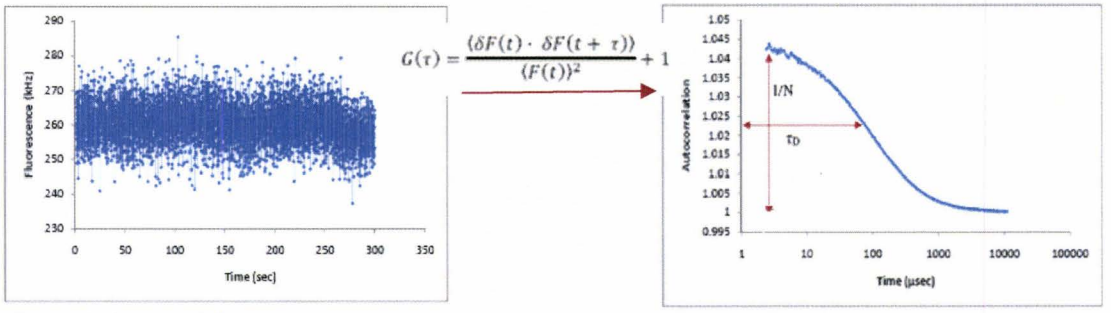

Figure 8. A typical fluorescence signal and its corresponding AC curve

Models that can be used to fit autocorrelation curves are discussed in Chapter 2.6.

1.5.3 Deriving information from the autocorrelation curve

As depicted in Figure 8, the average number of fluorescent molecules in the confocal volume can be calculated from the zero-time correlation value $G(0) = \frac{1}{N}$ [72]. The half maximum of the AC curve's amplitude corresponds to the diffusion time τ_D which is equal to the average time that a fluorophore spends in the detection volume. This observation volume is assumed to have a 3-D Gaussian ellipsoid profile, which

decays to $1/e^2$ at r_0 in the lateral direction and z_0 in the axial direction, as shown in Figure 7 (b).

The AC curve shown in Figure 8 is for a fluorophore undergoing Brownian translational motion. When the type of motion deviates from this, the shape of the AC function changes and can provide information about the type of transport being experienced by the molecules [74]. Molecules undergoing anomalous diffusion, which is diffusion in a crowded environment such as a cell, will have an AC curve with a more gradual decay compared to molecules undergoing free diffusion. This difference is depicted in Figure 9.

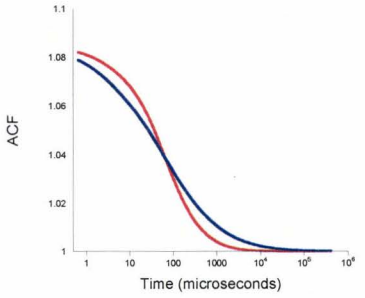

Figure 9. The shape of the AC curve depends on the type of motion. The shallower decaying curve in blue represents anomalous diffusion here, while the more steeply decaying curve in red results from simple diffusion

In simple diffusion, the mean-squared molecular displacement is a linear function of time: $\langle(\Delta x)^2\rangle \sim Dt$. But in anomalous diffusion, the mean-squared displacement is non-linear with time and this results in the relation $\langle(\Delta x)^2\rangle \sim Dt^{\alpha}$ where the anomalous diffusion exponent, α, is less than 1. Similarly, if a molecule is undergoing active transport, such as in the case of motion along a microtubule, then its AC curve will have a much steeper decay. So it may be possible to distinguish between different types of motion undergone by a particle based upon the shape of its AC curve.

Besides motion of fluorescent particles into and out of the detection volume, photophysics such as blinking can also result in fluorescence fluctuations [74]. Such photophysics would contribute an additional component to the autocorrelation curve.

1.5.2 Fluorescence correlation spectroscopy in cellular environments

The relative non-invasiveness of FCS makes it a good technique for studying the dynamics of in vivo systems. Unlike techniques such as fluorescence recovery after Photobleaching (FRAP), FCS does not employ high powers or require high fluorophore concentrations. On the contrary, FCS works better with a very low fluorophore concentration, on the order of nanomolars.

After FCS was combined with confocal microscopy in the early nineties, a wide range of in vivo studies employing FCS began to be reported. Mobility measurements were successfully taken in the cytosol, nucleus and cell membranes with temporal resolutions ranging from nanoseconds to seconds [75]. FCS has been used to characterize the types of motion that take place in different areas of the cell. For instance, the motion of EGFP was found to be strongly anomalous in the nucleus, while being much closer to simple diffusion in the cytoplasm [76]. Differences in viscosities between different cells or cell compartments have also been determined by measuring the changes in the diffusion coefficients of a fluorophore in these different locations [75]. In addition, FCS has been used to study active transport along tubular structures in plants using GFP as a fluorophore [77].

Membranes have proven to be a good environment for FCS, since there is little autofluorescence there [72]. For instance, studies have been performed to understand lipid diffusion across membranes [72]. FCS has also been used for accurate measurements of diffusion coefficients for DNA in live cells. [78].

1.5.3 Challenges of fluorescence correlation spectroscopy in vivo

Photobleaching, which is necessary in FRAP, is extremely undesirable in FCS. When a molecule is photobleached in the observation volume, it results in erroneous mobility calculations, because it appears as if the molecule has spent less time in the confocal volume than it actually has [75]. Slow processes cannot be characterized due to photobleaching. Even with the development of fluorophores over the last few decades,

photobleaching is still a challenge. It is more of a significant problem in vivo than in vitro, since in vitro the samples are of microlitre volumes, while the volume of a cell is on the order of picolitres [79]. So photobleaching depletes the already small reservoir of fluorescent molecules in vivo. To reduce this effect, the laser powers used should be kept as low as possible, which also has the undesirable effect of reducing signal to noise. However, low intensity power is also important in order to prevent cell damage [75].

Another problem faced is that some fluorophores can interact with cellular structures, reversibly binding to them and distorting the motion of the biomolecules that they are tagged to [75]. For instance, rhodamine is lipophilic and non-specifically interacts with intracellular membranes, which can result in seemingly lower mobility coefficients. This effect could lead to apparent anomalous diffusion on the AC curve. If this is not accounted for, then the deceptively lower mobility coefficients that are derived from these curves can be interpreted to mean increased intracellular viscosity. Alternatively, the AC curve may suggest that two diffusing species exist [75]. The freely diffusing fluorophore would have one decay term and the interacting species another.

In some cases, non-specific interactions can be avoided by binding the dye to a target molecule like DNA or a protein [75]. The target molecule can act like a shield for the fluorophore against intracellular membranes, and can dominate the dynamics of the motion. Intracellular interactions are one of the reasons why genetically incorporating fluorescence, such as with green fluorescent protein (GFP), is favored. GFP does not undergo non-specific interactions [75]. It is therefore crucial that the appropriate fluorescent labels be chosen carefully depending upon the environment they will be in.

Sometimes long acquisition times, on the order of minutes, are required to increase the S/N. This is especially true for in vivo applications which use low laser powers to reduce photobleaching, autofluorescence or photodamage. Long acquisition times are also needed to track slowly diffusing molecules such as transmembrane receptors. However, it can be difficult to take long measurements in vivo. This is because during the long acquisition times, the cell or plasma membrane may move, changing the measurement conditions [74].

Another challenge associated with analyzing FCS data is knowing which model to choose to fit the curve. There are cases when a model is used that appears to fit the AC curve well, but in reality does not describe the type of motion or photophysics accurately. This is especially true when new fluorophores are used, or old fluorophores in new environments.

Chapter 2 Materials and Methods

2.1 Fluorophores Used in this Study

CdSe QDs capped with a ZnS shell and functionalized with carboxyl were purchased from Invitrogen. As measured by FCS, these QDs had an approximate radius of 9nm, and they emitted at a peak wavelength of 605nm with a FWHM of about 30nm. Bovine serum albumin (BSA) (BioShop, Burlington ON) was adsorbed onto the QDs in order to minimize their aggregation. The QDs were diluted to concentrations ranging between 4nM and 1.6μM using a mixture of phosphate-buffered saline (PBS) and BSA as a buffer, such that BSA was present at a concentration of 0.5mg/ml.

BSA-Alexa Fluor 555 conjugate (BSA-Alexa 555) (Invitrogen) was diluted in PBS to concentrations between 15nM and 1.5μM. This fluorophore had a radius of about 3nm, as measured by FCS. All fluorophores were centrifuged at 4°C for 20 minutes at 13000rpm before injection. The diagram below depicts the absorption and emission spectra of the QDs and BSA-Alexa 555 used in this study:

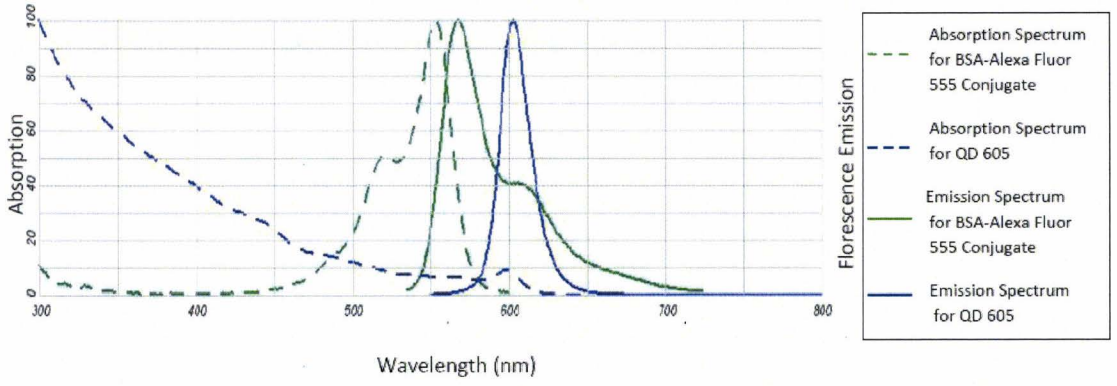

Figure 10. The absorption and emission spectra of QD 605 and BSA-Alexa 555. Adapted from [16]

2.2 Microinjection of Fluorophores

The various fluorophores used in this study were injected into adult wild type Bristol strain N2 *Caenorhabiditis elegans* (*C. elegans*). These worms were grown in agar culture dishes seeded with OP50 bacteria as previously described [64]. 24 hrs before each experiment, the *C. elegans* were chunked onto fresh seeded plates.

Microinjection needles were made from Narshige microcapillaries pulled using a vertical Narshige micro-needle puller. Needles were opened using 24.5% hydrofluoric acid and 7000hPa pressure. Pulled microcapillaries were used to transfer a few microlitres of the supernatant from the centrifuged fluorophore into the back of the microinjection needle.

After being filled, the microinjection needles were loaded into an Eppendorf FemotJet Microinjector connected to a Zeiss Axiovert 200 microscope. Adult worms were picked for microinjection from the culture dish using a platinum pick and then immobilized on their sides in a drop of halocarbon oil on 2% agar pads. Agar pads were positioned on the microinjection microscope stage and worms injected at 4000hPa in one or both gonad arms with the fluorophore of interest. QD injection concentrations ranged from 80nM-1.6μM. After injection, worms were rescued by placing a drop of M9 buffer on them, thereby releasing them from the agar pad. Using a mouth pipette, worms could then be transferred to a new seeded plate and left to recover.

2.3 Imaging Embryo Development

Worms injected with the CdSe QDs or BSA-Alexa were given 6 to 8 hours to recover and to fertilize oocytes that incorporated the fluorescent material into them. To prepare the fertilized eggs for imaging, a thin layer of 2% agar would be formed on a microscope slide, which prevented dehydration of the embryos. 3-4 μL of M9 buffer would then be placed in the centre of a No. 1½ 18mm x 18mm cover slip. Next, a recovered worm would be transferred to the drop of buffer. Using two 30G ½ needles the worm would be dissected in order to release its fertilized eggs. This would be repeated

with one or two more recovered worms. After dissection was complete, the microscope slide containing the agar layer would be placed on top of the cover slip containing the embryos. Wax was used to seal the edges of the cover slip.

Development of the embryos was tracked using a Leica TCS SP5 fluorescence confocal microscope system. A 561nm diode-pumped solid-state laser was used to excite the QDs. Green laser excitation was chosen to minimize autofluorescence. Images of embryos containing QDs were taken using 95% of the laser power (9.5mW). Fluorescence was collected with a 63x 1.3NA objective. The system employed a prism spectrometer which allowed the collection of emitted fluorescence to be limited between 575nm and 650nm. A Hamamatsu photomultiplier tube (PMT) was used for detection. The system was set to take confocal fluorescence scans and corresponding differential interference contrast (DIC) images of 512x512 pixel format with a scanning speed of 400Hz. Images of embryos containing BSA-Alexa 555 were taken under similar conditions, except that the laser power was set to 2mW and emitted fluorescence was collected between 565nm and 650nm. All images were analyzed using Image J. The diagram below illustrates the collection range for emitted fluorescence in relation to the emission of the two fluorophores.

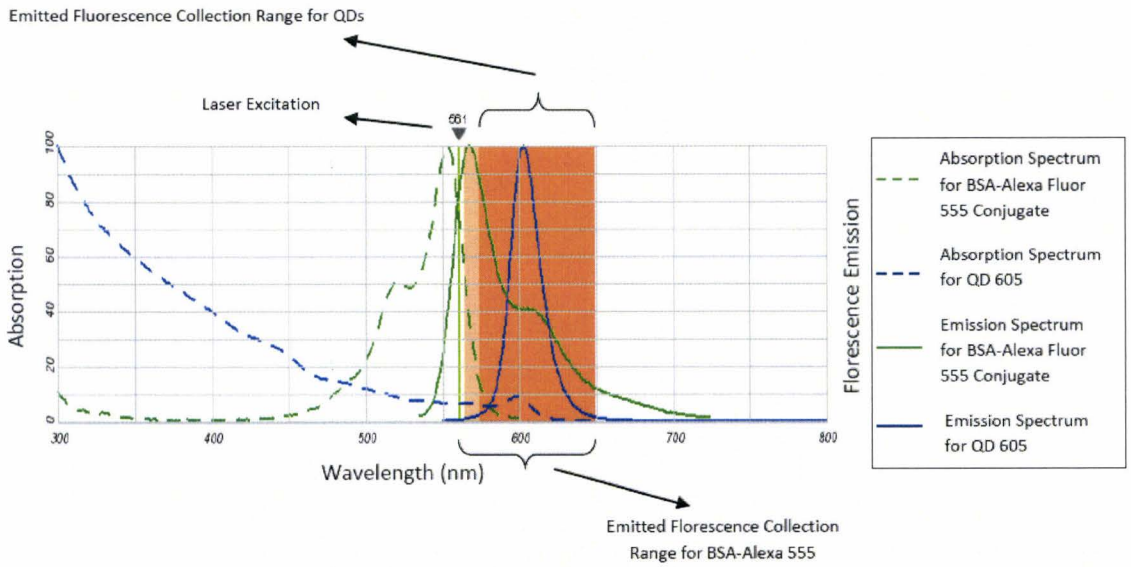

Figure 11. The graph shows the range over which emitted fluorescence was collected relative to the spectra of QD 605 and BSA-Alexa 555. Excitation was provided at 561nm. Adapted from [16]

2.4 Determining the Concentration of Fluorophores in the Embryo

A calibration curve was constructed in order to determine the concentration of quantum dots in the imaged embryos. To achieve this, several dilutions of QDs in PBS were prepared at concentrations ranging from about 4nM to 60nM. The exact concentration of the QD samples imaged was determined using FCS. The FCS setup used is described in section 2.6.

Images were taken at 2.5μm intervals over the entire depth of the sample. Imaging was performed on the same SP5 microscope used to image the embryos, using the same imaging conditions. A typical fluorescence profile over the depth of a diluted QD sample is shown on the next page:

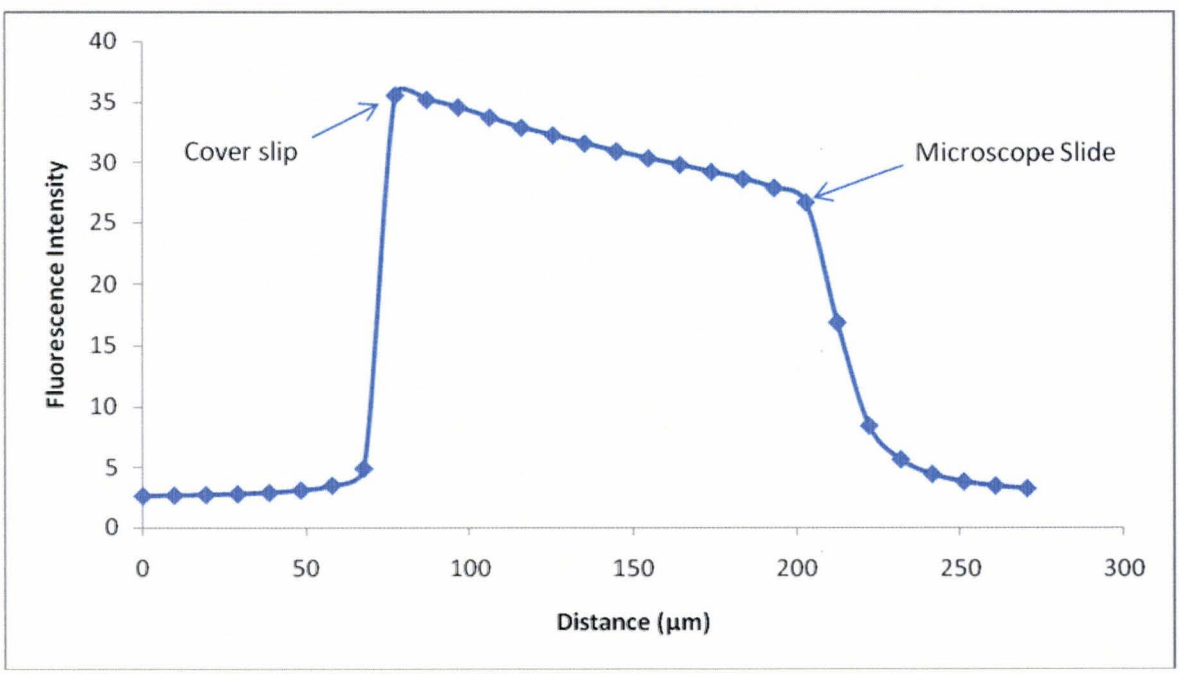

Figure 12. The graph illustrates how the fluorescence collected from the QD sample decreases with increasing distance from the objective

The graph indicates that the measured fluorescence of the sample drops as the distance from the objective increases. There is about a 1-2% decrease every 10μm. This is a result of the refractive index mismatch between the sample and the glycerol used with the oil-immersion objective, which causes a reduction in the resolution and intensity as light is focused deeper and deeper into the sample [80].

The embryos imaged were approximately 35μm thick. A stack of images was collected over the entire depth of each embryo, at about 5μm intervals. QD concentrations were calculated based on fluorescence measured from the brightest plane in each embryo, which was usually the mid plane. The distance of an embryo from the cover slip was estimated to be between 0 and 20μm. It follows then that an embryo's mid plane was at an approximate distance of 17.5-37.5μm from the cover slip. Consequently, the calibration curve was constructed for fluorescence measured at a distance of 27.5μm from the cover slip:

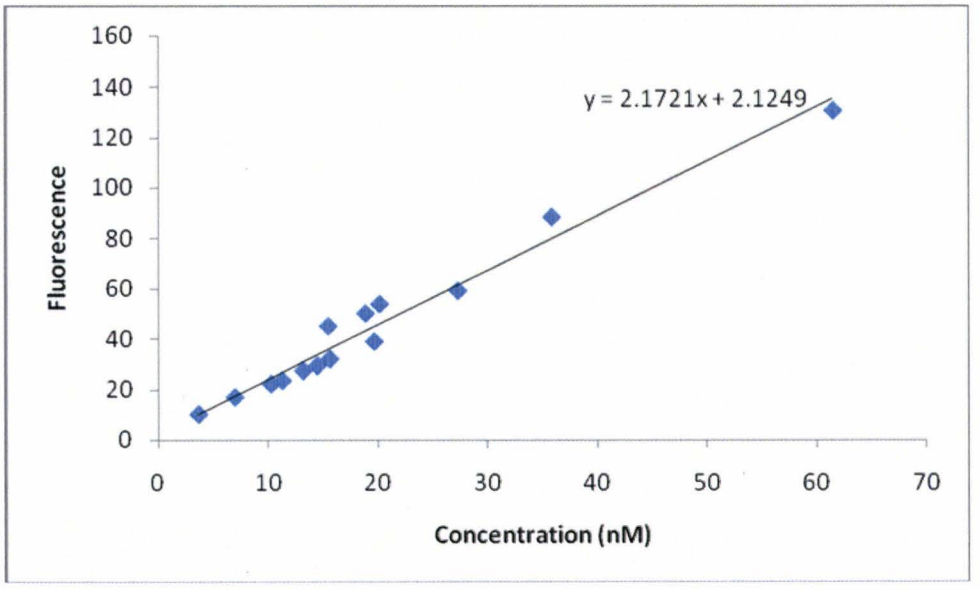

Figure 13. The fluorescence collected from a sample containing QDs is directly proportional to the concentration of those QDs

A calibration curve was similarly constructed for BSA-Alexa 555, as shown on the next page:

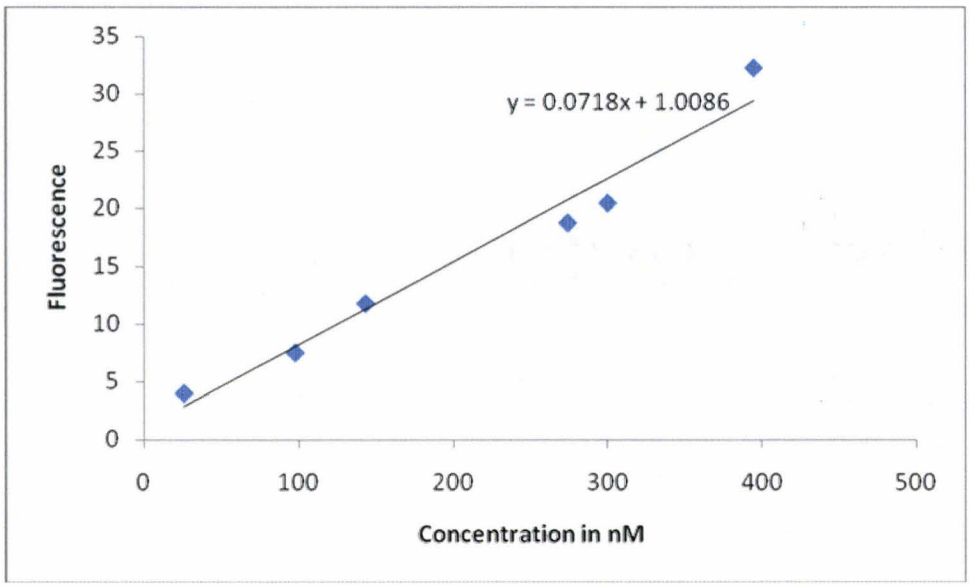

Figure 14. The fluorescence collected from a sample containing BSA-Alexa 555 is directly proportional to the concentration of the BSA-Alexa 555

2.5 Image Analysis

The distribution of fluorophores in the embryos was characterized over their development by calculating the autocorrelation function of images taken of the embryos: [81]:

$$G(r) = \frac{\langle I(r') \cdot I(r+r') \rangle}{\langle I(r') \rangle^2} - 1 \qquad (1)$$

Here, I(r') and I(r+r') are the intensity values associated with pixels r' and r+r' respectively. $\langle I(r') \rangle^2$ is the average intensity of the image being analyzed. From this autocorrelation, the characteristic size of the aggregates can be determined. An Image J plug-in was written to calculate this function for images of embryos taken at various stages of development. The script for this plug-in can be found in Appendix A. For each image analyzed, the autocorrelation function was calculated for 5 different regions within the embryo, and the resulting 5 curves were averaged. The immobile contributions of the average autocorrelation curves were fit with the following two-component Gaussian model:

$$G(r) = g_1 e^{-\left(\frac{r}{r_1}\right)^2} + g_2 e^{-\left(\frac{r}{r_2}\right)^2} + g_0 \qquad (2)$$

Here, r_1 and r_2 correspond to the half maximum values associated with curve's two components. They correspond to two characteristic sizes associated with features of the fluorescence image. g_1 and g_2 correspond to the proportion of the curve associated with each of the two components. g_0 is the baseline offset.

2.6 Fluorescence Correlation Spectroscopy in Oocytes

2.6.1 Experimental setup

Injections were performed as described in section 2.2. The concentration of injected CdSe QDs ranged from 8nM to 80nM. BSA-Alexa 555 was injected at about 200nM. Worms were left to recover for one to two hours after injection, to allow sufficient time for them to incorporate the nanomaterial into newly forming oocytes. Worms were immobilized on a layer of 2% agar mixed with 40nM NaN_3. A cover glass was placed on the agar and its edges sealed with wax.

Experiments were performed with an Insight Fluorescence Correlation Spectroscopy system (Evotec). The confocal FCS setup used is similar to that depicted in Figure 7. A 532nm NdYVO continuous laser was used to excite the samples. Attenuation of the laser was controlled with neutral density filters. The laser light was first passed through a dichroic mirror and then focused onto the sample by a 40x 1.15 NA water immersion objective. The fluorescence emitted from the sample was then collected by the objective, reflected off the dichroic mirror, and sent through a 590nm/60nm band-pass filter, before being focused through a 40μm pinhole onto a dual avalanche photodiode detector. This collected fluorescence was then sent to an autocorrelator. Evotec Acapella software was used to acquire the data. All experiments were performed at room temperature. The laser power used varied between 0.7μW and 10μW.

Before each experiment, the system was calibrated with Alexa 546 (Diffusion Coefficient= 341$\mu m^2/s$ [82]) to determine the dimensions of the confocal volume and to

ensure optimal alignment. Once a fluorescent oocyte was found, a confocal scan of the oocyte would be taken with the system's confocal scanning apparatus. The precise positions at which FCS was desired to be taken could then be specified on the confocal image. An average 5 curves were taken at each position. Between 5 and 7 positions were selected in the cytoplasm, and between 2 and 5 positions were selected in the nucleus of each oocyte. The curves taken in each position were averaged and analyzed with the data analysis program KaleidaGraph.

2.6.2 Analysis of FCS curves

2.6.2.1 Diffusion models

In order to make accurate conclusions from an AC curve, it has to be fit with the appropriate model. If the sample of interest consists of just one species of diffusing fluorophores, then fluorescence fluctuations are caused by the diffusion of the species into and out of the observation volume. In this case, the AC fit would be derived from Fick's second law of diffusion [74]. It would take the following form [72]:

$$G_D(\tau) = \frac{1}{\left[N\left(1+\frac{\tau}{\tau_D}\right)\left(1+\frac{\tau}{\tau_D \cdot \omega^2}\right)^{0.5}\right]} \qquad (3)$$

N is the number of molecules in the detection volume, τ_D is the characteristic diffusion time and ω is the aspect ratio of the confocal volume. It is defined as $\omega = \frac{z_0}{r_0}$, where z_0 is the axial dimension of the observation volume and r_0 is the lateral dimension as seen in Figure 7 (b). The diffusion coefficient, D, can be determined from τ_D using the following relation [72]:

$$D = \frac{r_0^2}{4\tau_D} \qquad (4)$$

Typical values for D can range from about 300 $\mu m^2/s$ for a small freely diffusing dye to about 0.01 $\mu m^2/s$ for a fluorophore tagged receptor. The fluorophore's hydrodynamic radius r_H can be calculated from τ_D using the Stokes-Einstein relation [7]:

$$r_H = \frac{2kT\tau_D}{3\pi\eta r_0^2} \quad (5)$$

Here k is Boltzmann's constant, T is the absolute temperature and η is the viscosity of the medium. From the 3-D Gaussian profile assumption for the detection volume, V can be determined from $V = \pi^{\frac{3}{2}} \cdot r_0^2 \cdot z_0$ [78]. Knowing the confocal volume, V, the concentration of fluorophores, C, can be deduced from the simple relation $C = \frac{N}{V}$.

The brightness per fluorescent particle, BPP, can also be calculated from the relation $BPP = \frac{\langle F(t) \rangle}{N}$ [78]. The BPP can be influenced by the environment, and so can convey information regarding how the environment affects the quantum yield of a fluorophore [74]. BPP can also act as an indicator of how well an FCS system is aligned. So at the beginning of an FCS experiment, alignment can be checked by acquiring FCS curves of a calibration sample for which the photophysical and diffusional properties are known, and calculating the BPP value.

In order to account for anomalous diffusion, Equation 3 would be modified to the following [83]:

$$G_{D(anom)}(\tau) = \frac{1}{N\left(1+\left(\frac{\tau}{\tau_D}\right)^{\alpha}\right)\left(1+\frac{s}{\omega^2}\left(\frac{\tau}{\tau_D}\right)^{\alpha}\right)^{\frac{1}{2}}} \quad (6)$$

2.6.2.2 Accounting for quantum dot blinking

A number of approaches have been taken to model the photophysical term of the autocorrelation curve for QDs. Early studies used Monte Carlo simulations [84], as well very complex models that required large number of fitting parameters [85]. A recent study proposed the following model to account for QD blinking [1]:

$$G(\tau) = G_D(\tau) \cdot \left(1 + \frac{F \cdot g_{blink}(\tau)}{1-F}\right) \quad (7)$$

In these equations, $G_D(\tau)$ is the fit for the portion of the AC curve associated with diffusion, F is the fraction of QDs in the blinking state, and $g_{blink}(\tau)$ is described by the following:

$$g_{blink}(\tau) = A\tau^{\alpha-2} \quad (8)$$

Here α is the power law exponent. It was found that α=1.5 for all of their fits.

One limitation of this model that has been pointed out by another group is that it requires that the curve first be fit at low powers with standard diffusion in order to determine the characteristic diffusion time, and then that this diffusion time be fixed at higher intensities in the equation accounting for blinking [86]. This group used two variations of FCS in order to try to quantify the bias that blinking has on the diffusion component of FCS curves: temporal image correlation spectroscopy (TICS) and k-space imaging correlation spectroscopy (kICS). Using these techniques they showed that if a model accounting solely for diffusion is used to fit a QD AC curve, then the calculated diffusion coefficient will be overestimated. Furthermore, they demonstrated that k-space imaging correlation spectroscopy allows blinking and diffusion dynamics to be completely separated.

Some studies have tried to avoid the task of dealing with QD blinking by fitting AC curves with simple diffusion models [7, 13]. One FCS study reported that no blinking of CdSe/ZnS QDs could be detected, perhaps because of the low excitation powers used [13]. At least one study has accounted for blinking using a single exponential decay [35]. In addition, previous work in our lab has shown that the QDs used in this study exhibited blinking that could be described by exponential kinetics when using 1-photon excitation (Thakur and Fradin, unpublished data). Accordingly, in this study, FCS curves taken in solution were fit with the following equation to account for both diffusion and blinking [72]:

$$G(\tau) = G_D(\tau) \times \frac{1-T+Te^{-\tau/\tau_{trip}}}{(1-T)} \quad (9)$$

$G_D(\tau)$ is defined in Equation 3. T is the fraction of molecules in the triplet state and τ_{trip} is the triplet state relaxation time, which corresponds to the amount of time molecules reside in dark state. Similarly, FCS curves taken in the *C. elegans* cellular environment were fit with the following equation:

$$G(\tau) = G_{D(anom)}(\tau) \times \frac{1-T+Te^{-\tau/\tau_{trip}}}{(1-T)} \qquad (10)$$

Here, $G_{D(anom)}(\tau)$ is defined in Equation 6, and accounts for anomalous diffusion.

2.6.2.3 The effects of background on the autocorrelation curve

The extreme sensitivity of FCS also makes it very susceptible to artifact measurements, which can lead to misleading data [75]. This is especially true in an intracellular environment where the quality of the signal is significantly reduced. For instance, autofluorescence can make it difficult to obtain accurate results. Two major sources of autofluorescence in cells are NADH and flavoproteins, which are mostly located in the mitochondria [79]. If autofluorescence creates a constant background signal, then the concentration of fluorophores will be overestimated, while the brightness per particle will be underestimated [72]. It is also possible for autofluorescent molecules to be diffusable and thus show up as a separate species in the AC curve [72]. However, in many cases the autofluorescent particles are immobile, and so within the first few seconds of exposure to laser light, these particles are photobleached [87]. To minimize the effect of autofluorescence on the AC curves, a control experiment can be carried out to determine the level of background fluorescence F_{BG}. Then the AC function could be accordingly scaled by the factor $\frac{\langle F(t)\rangle^2}{[\langle F(t)\rangle - \langle F_{BG}\rangle]^2}$ [72].

Chapter 3 Results

3.1 Incorporation of quantum dots into the oocytes of *C. elegans*

QDs injected into the *C. elegans* gonad arm were dispersed throughout the arm and incorporated into developing oocytes. An example of this is shown in Figure 15. This worm was anesthetized approximately one hour after injection, and then immediately imaged. From the calibration curve in Figure 13, it was determined that the QDs were diluted by about 10-100 times when injected. This depended upon how much the gonad arm was filled during injection. The average dilution factor of BSA-Alexa 555 was calculated to be about 4.

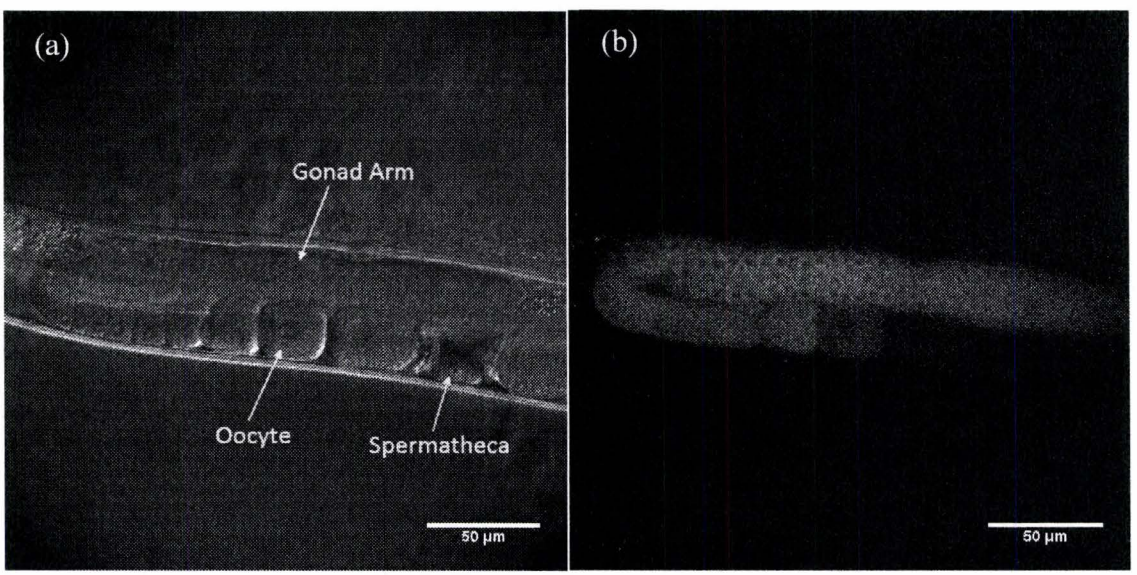

Figure 15. The (a) DIC and (b) confocal fluorescence images of a *C. elegans* worm with QDs injected into one of its gonad arms. The QDs can be seen to be incorporated into developing oocytes

When uncoated QDs were injected, they rarely dispersed as uniformly as the QDs shown in Figure 15. Instead, they would tend to aggregate near the point of injection and would not be incorporated into developing oocytes. An example of this is shown in Figure 16 on the next page.

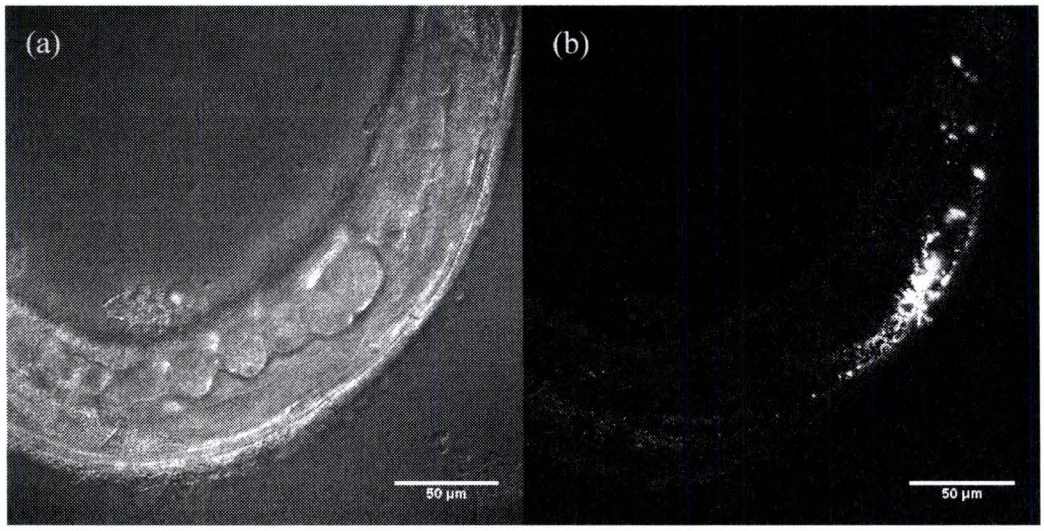

Figure 16. (a) DIC and (b) confocal fluorescence images showing how uncoated QDs aggregate in the gonad arm and are not easily incorporated into developing oocytes

3.2 The cytotoxicity of CdSe/ZnS quantum dots

Oocytes that incorporated QDs into them were observed to successfully undergo fertilization. Figure 17 below shows an example of developing fluorescent embryos dissected out of their mother after fertilization.

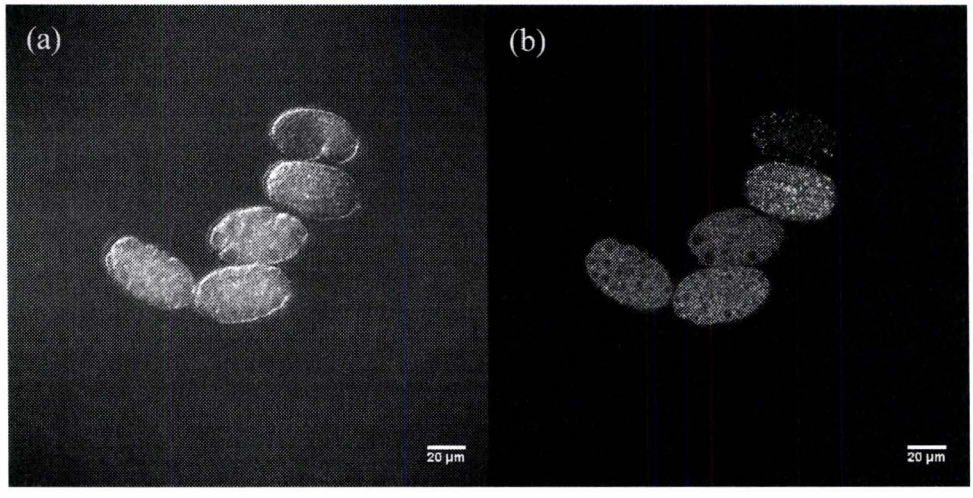

Figure 17. The (a) DIC and (b) confocal fluorescence images of developing embryos containing QDs. These embryos all developed and hatched successfully

Embryo viability was tracked using confocal microscopy. An embryo was considered viable if it developed normally until hatching. As a control, the viability of embryos from BSA-Alexa 555 injected *C. elegans*, as well as the viability of non-injected *C. elegans* embryos was determined. Additionally, the viability of non-fluorescent embryos from QD injected worms was investigated. Table 1 below summarizes the toxicity findings.

Table 1. A summary of the toxicity findings

Material Incorporated into the Embryos	Survival	Number of Embryos Observed	Concentration of Foreign Material
BSA Coated CdSe/ZnS QDs	85%	55	1-83nM
Uncoated CdSe/ZnS QDs	100%	8	1-13nM
BSA-Alexa 555	85%	26	56nM-1.2uM
None (Non-fluorescent embryos from injected worm)	87%	91	
None	76%	82	

Using the Scheffé's multiple pairwise test, it was found that the survival rate of the embryos containing QDs was not significantly different from the survival rate of control embryos ($p>0.05$) (see Appendix B). Non-viable embryos were usually early embryos that appeared to be damaged during the mounting process. In some cases, embryo development continued for a while after mounting before becoming arrested. In rare instances, embryos developed morphological abnormalities. This was true for both embryos containing QDs and control embryos. There was only one clear case of an

embryo abnormality which appeared to result from the QDs. This embryo is shown in Figure 18 below.

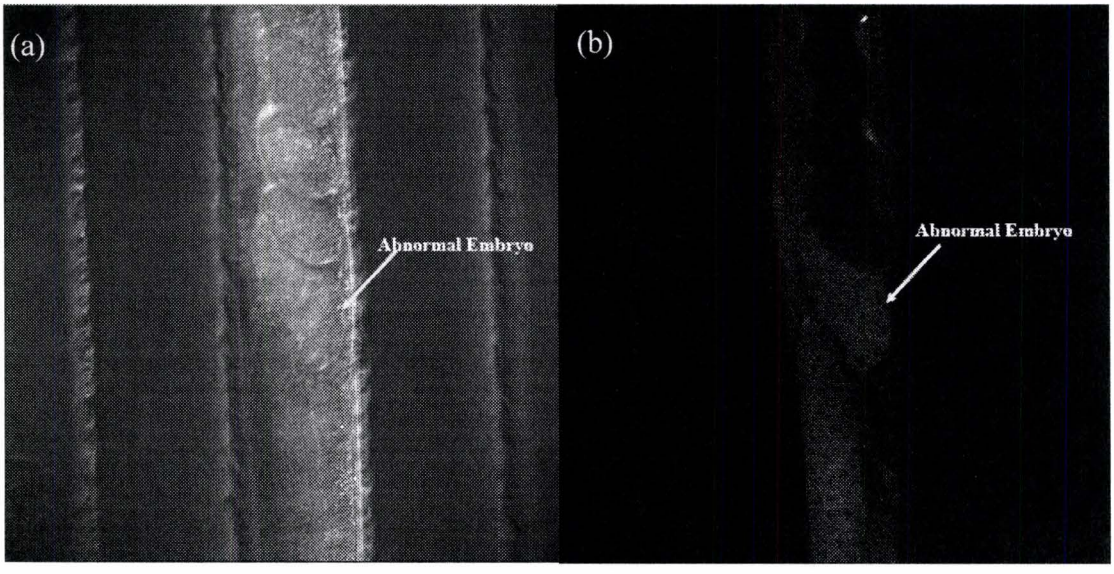

Figure 18. The (a) DIC and (b) confocal fluorescence images of an abnormal embryo containing QDs. Embryos that do not have any QDs incorporated into them can also be seen in this image, above the abnormal embryo

This early embryo was about 70% larger than the other embryos and did not develop any further. It is imaged here still in its mother's uterus. The concentration of QDs in the embryo was determined to be about 15nM.

3.3 Distribution of QDs in the embryo during development

It was observed that as an embryo develops, both the QDs and BSA-Alexa 555 introduced into it is packaged into aggregates. This process can be seen in the embryos depicted in Figures 25, 26, 31 and 32. Image analysis was used to quantify this process, as described in section 2.5.

3.3.1 The different contributions to the spatial autocorrelation function

The autocorrelation function was calculated for images of embryos at various stages of development. An example of an autocorrelation function produced from an image of an embryo is shown in Figure 19.

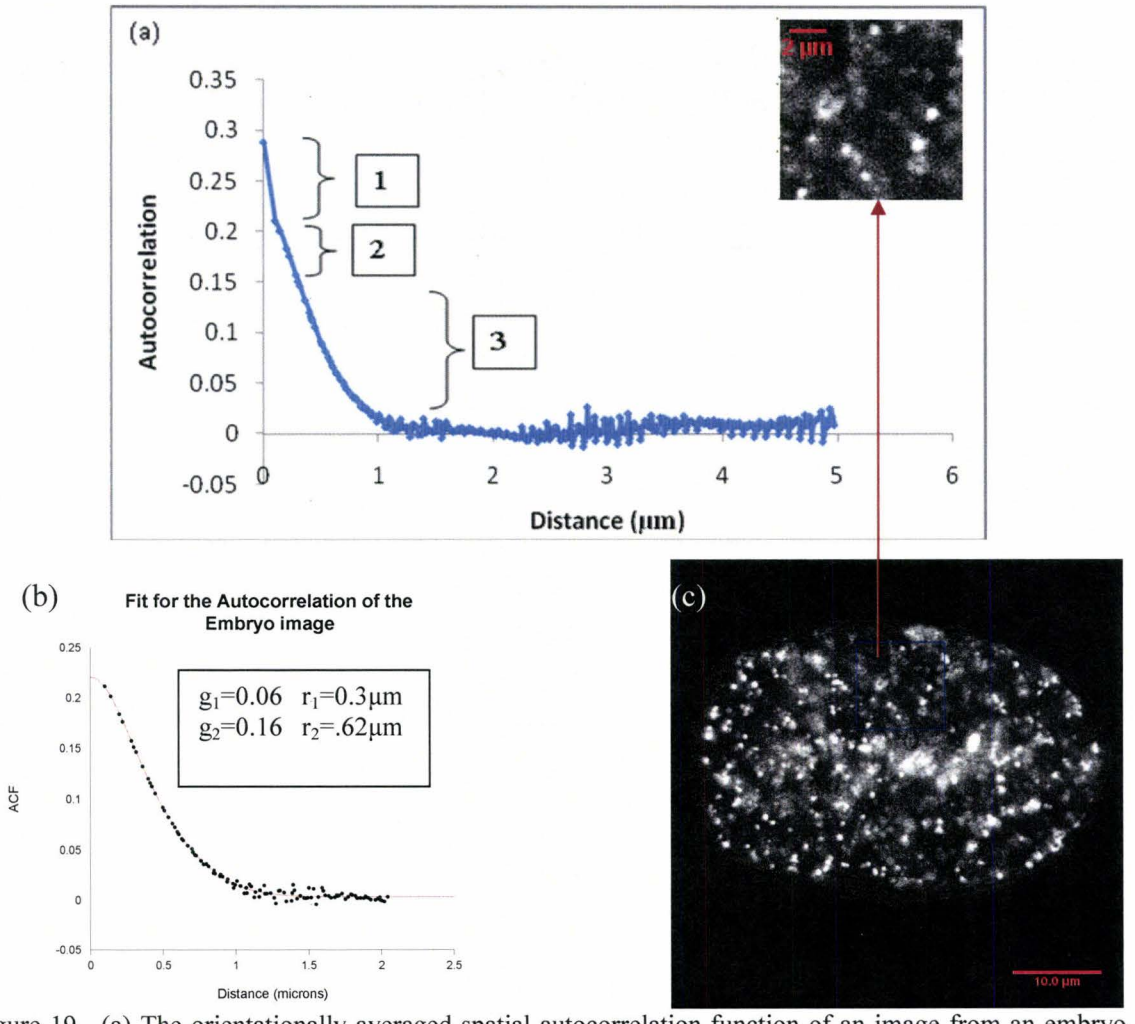

Figure 19. (a) The orientationally averaged spatial autocorrelation function of an image from an embryo containing QDs. (b) A selected part of the curve show in (a) ($0<r<2\mu m$) fit with Equation 2. (c) The region of the embryo from which the analyzed image was taken. In (b) g_1 is the amplitude of the curve corresponding to the population of immobile particles that exist below the resolution limit r_1, and g_2 is the amplitude of the curve corresponding to the population of immobile aggregates with radius r_2.

It was expected that the autocorrelation curve in Figure 19 (a) would result from at least two main contributions: a population of mobile particles and a population of immobile particles. In fact, as can be seen from the fit in Figure 19 (b), at least two components were needed to account the immobile contributions. Hence the graph in Figure 19 (a) resulted from three main contributions. The amplitude of the first component labeled (1) on the graph was proportional to the population of mobile particles in the embryo. (2) was proportional to the concentration of immobile particles

that existed below the resolution limit of the illuminating laser beam. (3) was proportional to the concentration of QDs that existed as immobile aggregates above the resolution limit.

In order to quantify the parameters of the autocorrelation curves associated with the immobile population of fluorophores, the immobile components were fit with Equation 2. The fit for the autocorrelation curve of Figure 19(a) is shown in 19 (b), along with the parameters extracted from the fit. r_1 here is on the order of magnitude of the resolution limit, and therefore represents particles for which $r<r_1$. r_2 is above the resolution limit and therefore represents visible particles. When measured manually, the radii of the visible aggregates in this image was found to range from about 0.6 to 1.3μm.

3.3.1.1 The contribution of mobile particles

To better understand how region (1) of the autocorrelation curve is proportional to the population of mobile QDs, consider Figure 20 below, which shows the autocorrelation of an image of purely mobile QDs in solution.

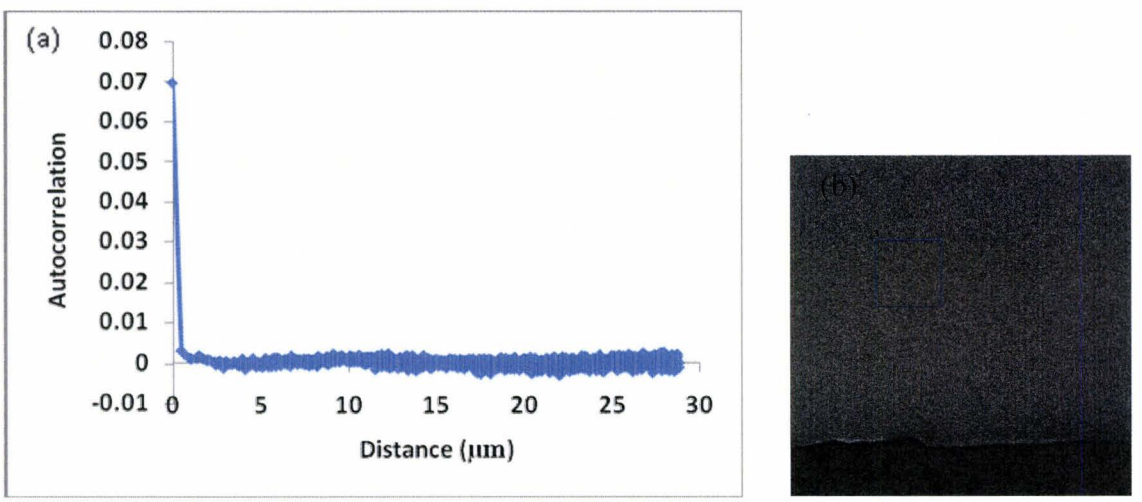

Figure 20. (a) depicts the autocorrelation for purely mobile QDs in solution. (b) shows the sample of the image for which the autocorrelation was calculated.

Since the motion of the mobile QDs is much faster than the scanning speed, a correlation is only seen at a distance=0μm, and the amplitude of this correlation is

inversely proportional to the concentration of the mobile QDs [88, 89]. The relationship between 1/g(0) and the concentration of QDs in solution measured by FCS is shown in Figure 21.

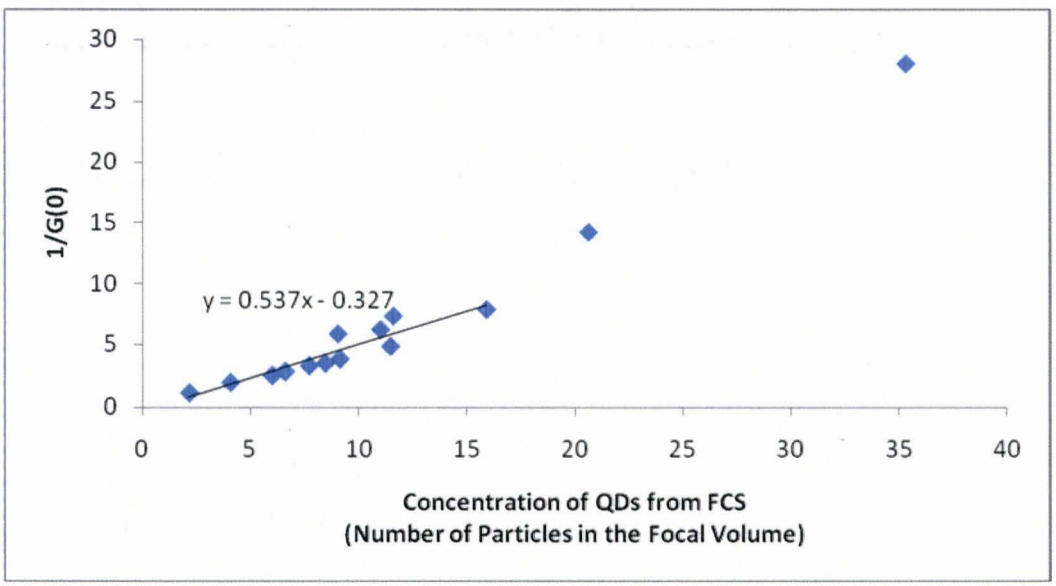

Figure 21. 1/g(0) versus concentration of QDs. A good linear fit was only found at low concentrations

A similar curve was constructed for BSA-Alexa 555:

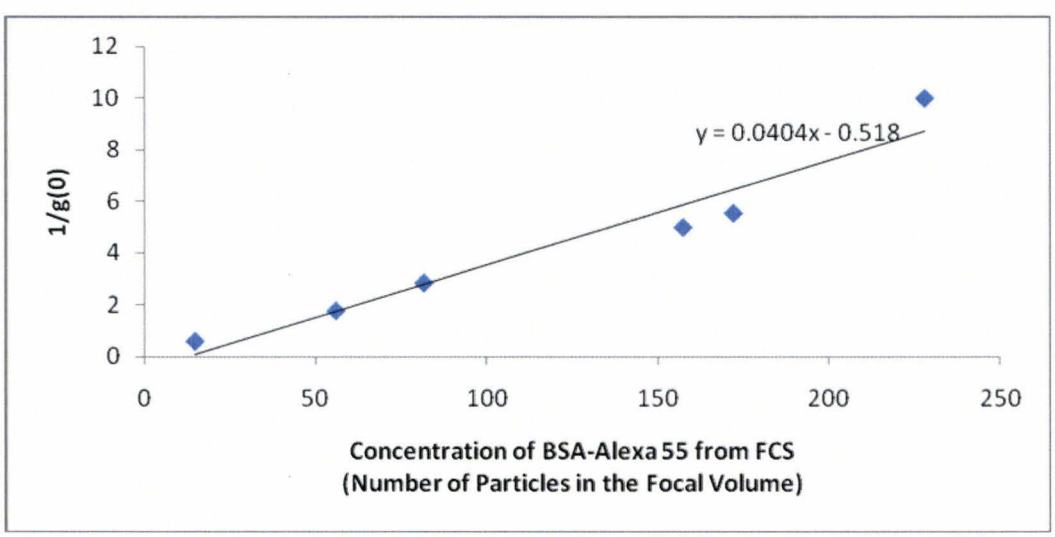

Figure 22. For mobile BSA-Alexa 555, 1/g(0) is proportional to the concentration of fluorophores

3.3.1.2 Large scale spatial features of the embryo

In some images, especially those of early embryos, repeating structural features, such us visible nuclei, resulted in additional components of the autocorrelation curves. An example of this is shown in Figure 23. The portion of the curve centered around 4.5μm represents the distribution of distances between repeating structures, in this case the nuclei.

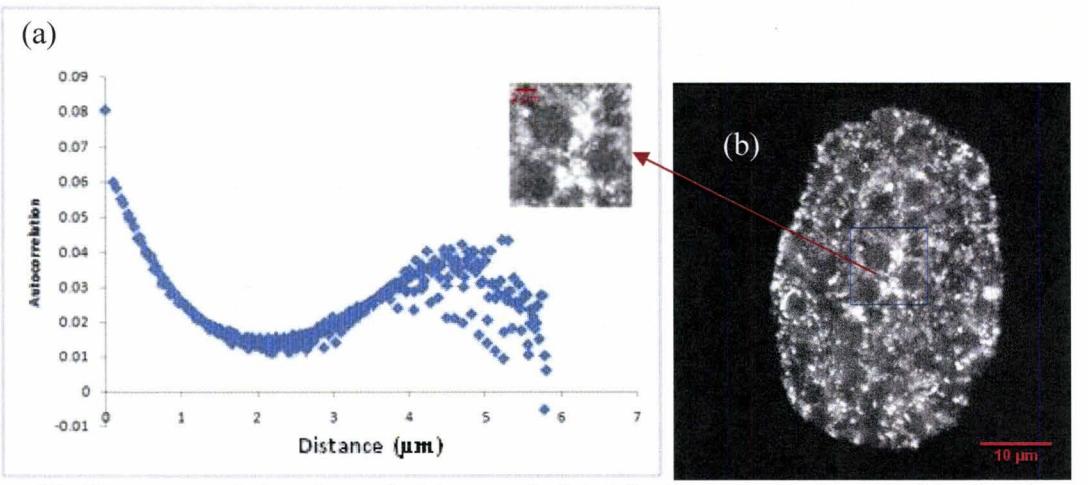

Figure 23. The autocorrelation shown in (a) was calculated for the region outlined in (b) taken from an image of an early embryo containing BSA-Alexa 555. After decreasing to the baseline, the autocorrelation function again increases, reflecting the patterning of the nuclei.

At later stages of development, similar features of the autocorrelation curve are also sometimes seen beyond the baseline, resulting from the patterning of the aggregates. An example of this is shown in Figure 24 on the next page:

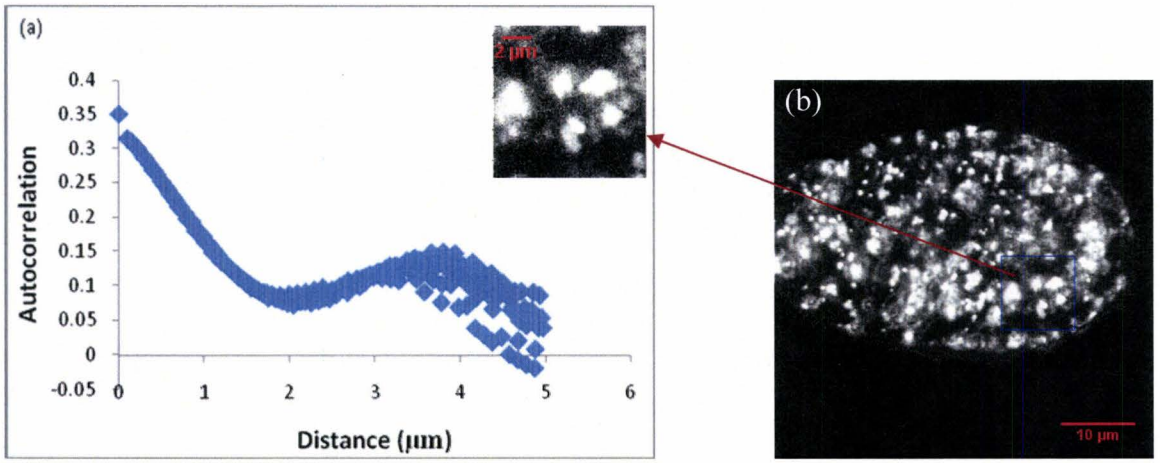

Figure 24. The autocorrelation shown in (a) was calculated for the region outlined in (b) taken from an image of an embryo containing QDs late in development. After decreasing to the baseline, the autocorrelation function again increases, and peaks around 3-4µm, a value close to the typical distance between neighboring aggregates.

Autocorrelation curves were fit for radius values below about 3µm in order to avoid these spatial effects from interfering with the analysis.

3.3.2 Changes in QD distribution during embryo development

To understand how the populations of mobile, diffraction limited immobile and large immobile particles change over embryo development, the amplitudes of contributions (1), (2) and (3) divided by the total amplitude of the autocorrelation function were plotted as a function of time. This analysis was carried out on images of embryos containing QDs and BSA-Alexa 555. Additionally, changes in the radii associated with the immobile components of the autocorrelation curve were also plotted as a function of time. Figures 25 through 32 show examples of these curves for embryos containing two different concentrations of QDs and two different concentrations of BSA-Alexa 555. The images from which the autocorrelations were calculated are also shown.

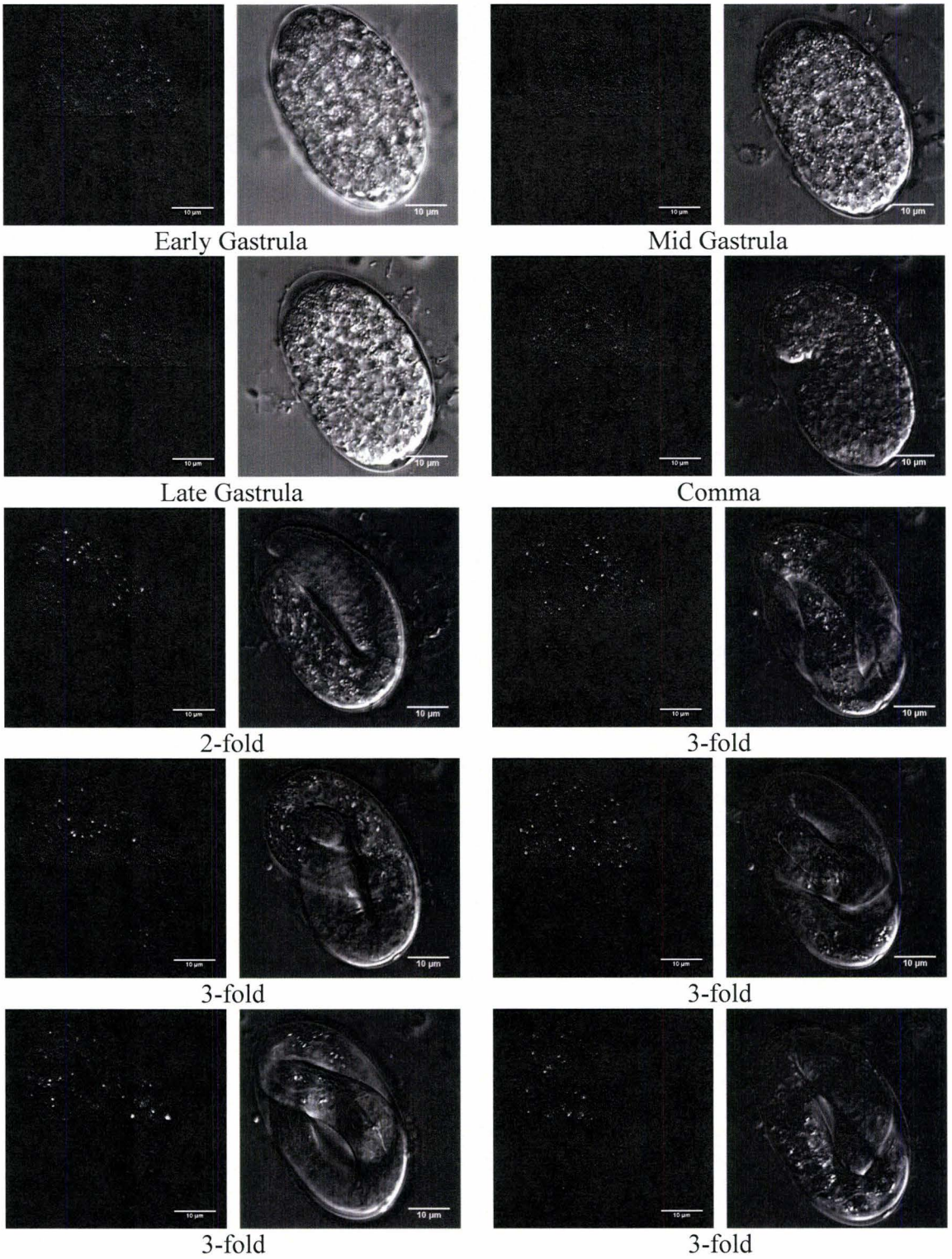

Figure 25. Embryo 1: Confocal fluorescence and DIC images showing various developmental stages of an embryo containing QDs at a concentration of 3nM. The top half of the fluorescence images were enhanced about 3.6 times to make the features more visible

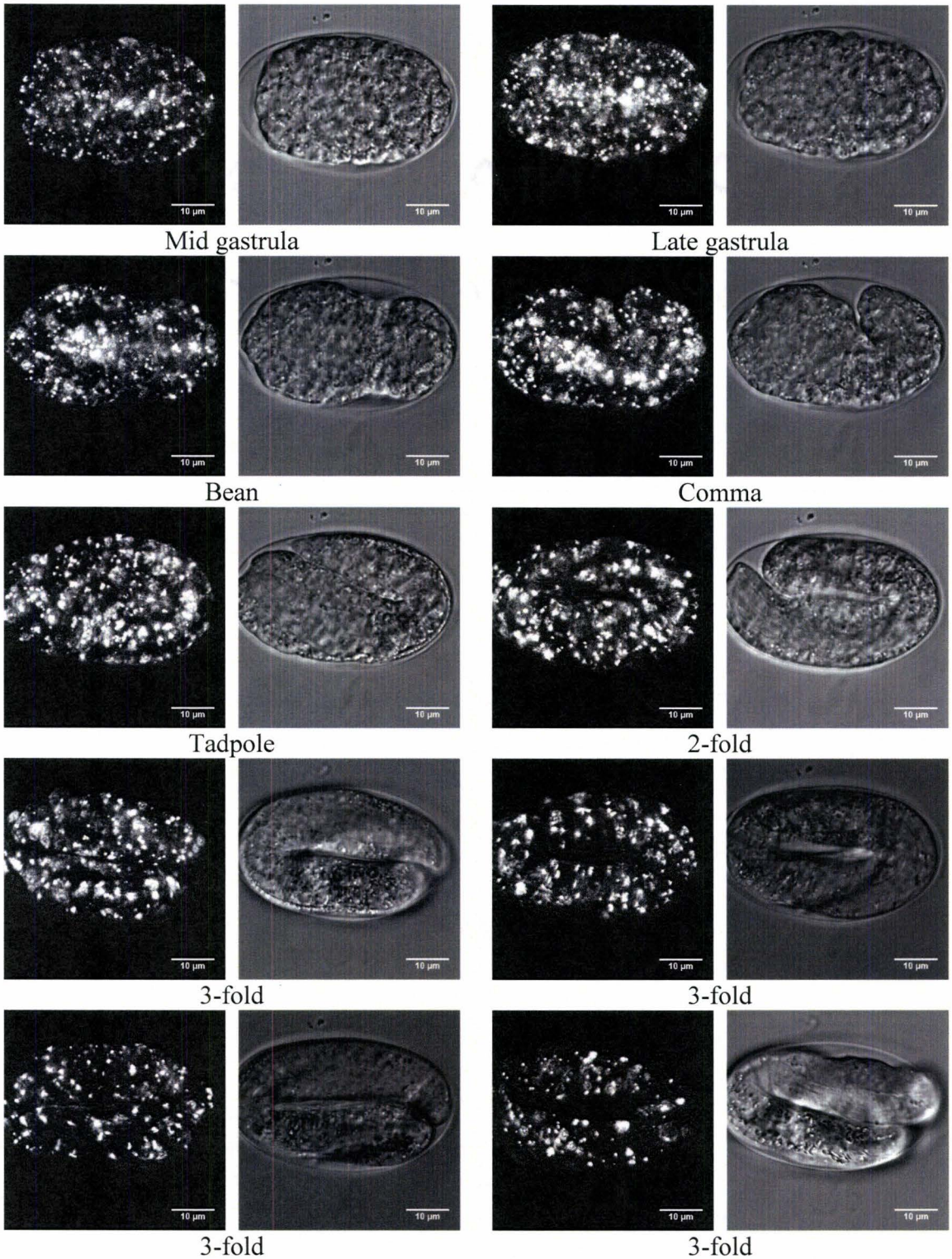

Figure 26. Embryo 2: Confocal fluorescence and DIC images showing various developmental stages of an embryo containing QDs at a concentration of 50nM

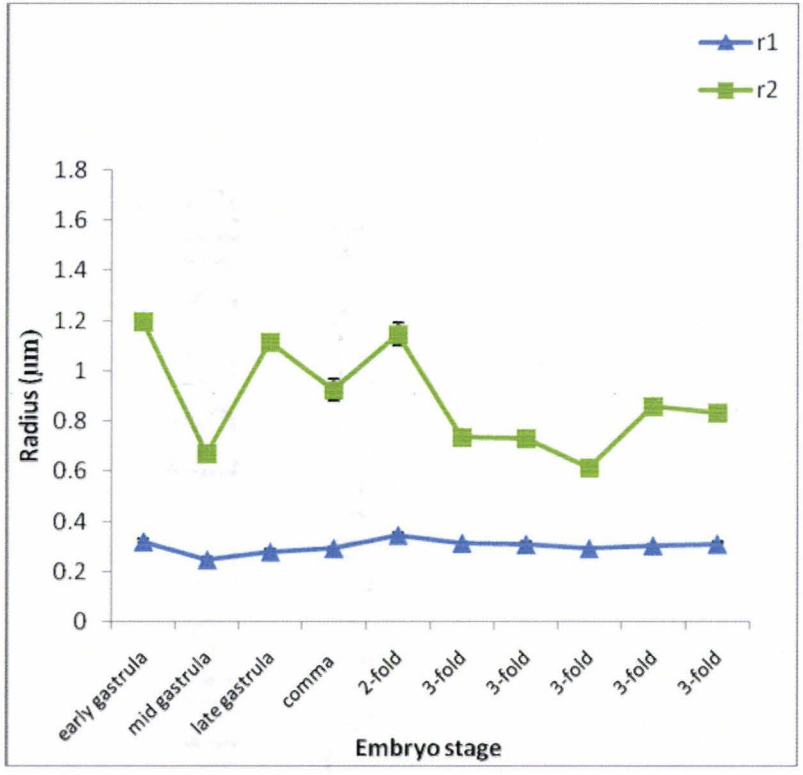

Figure 27. Change in the radii of immobile aggregates over the development of Embryo 1 with QD Concentration= 3nM

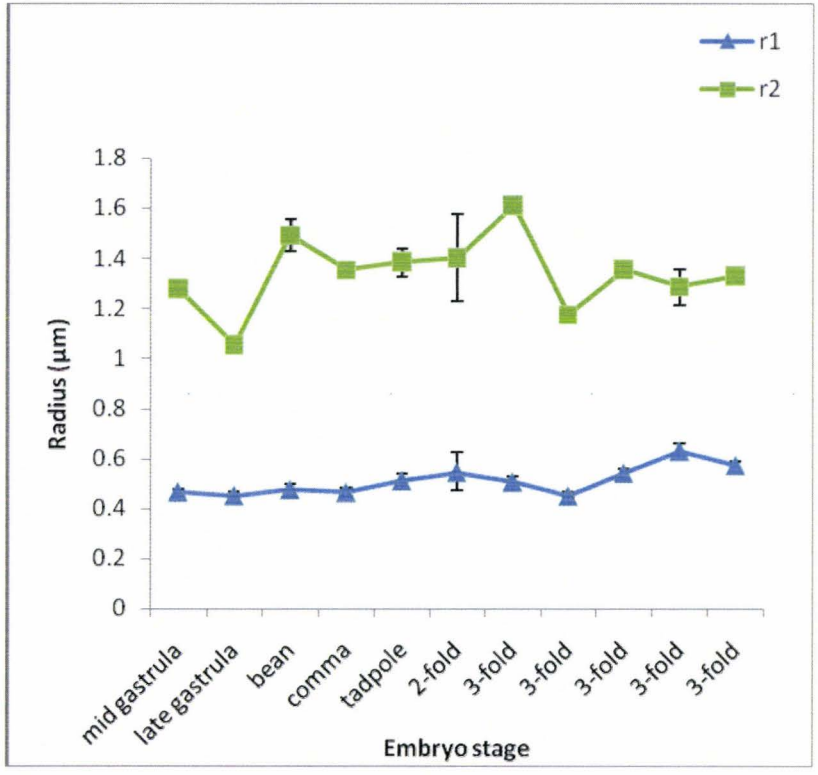

Figure 28. Changes in the radii of immobile QD aggregates over the development of Embryo 2 with QD concentration=50nM

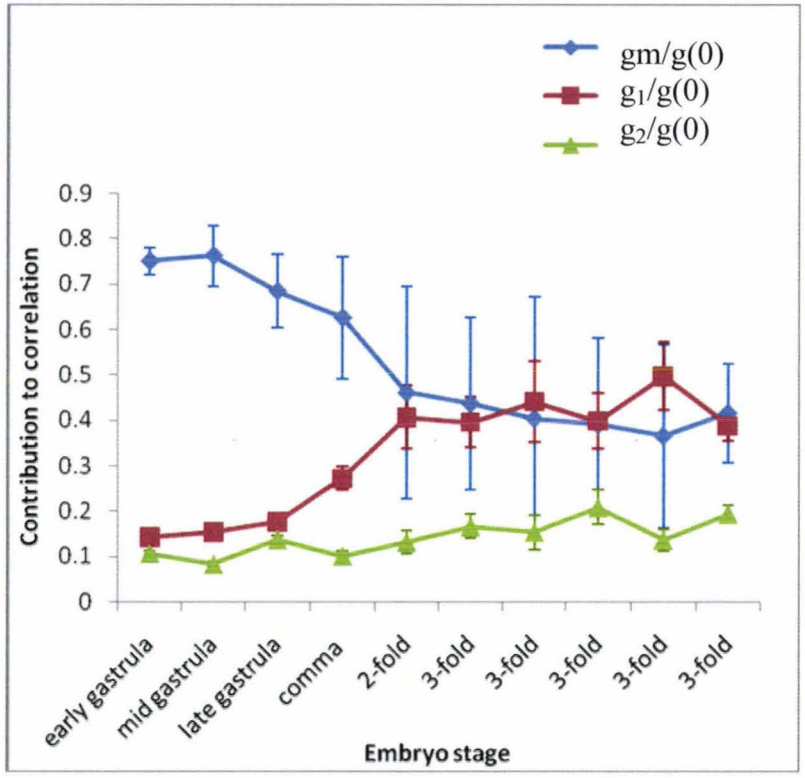

Figure 29. Changes in the proportions of mobile and immobile QDs over the development of Embryo 1 with concentration= 3nM

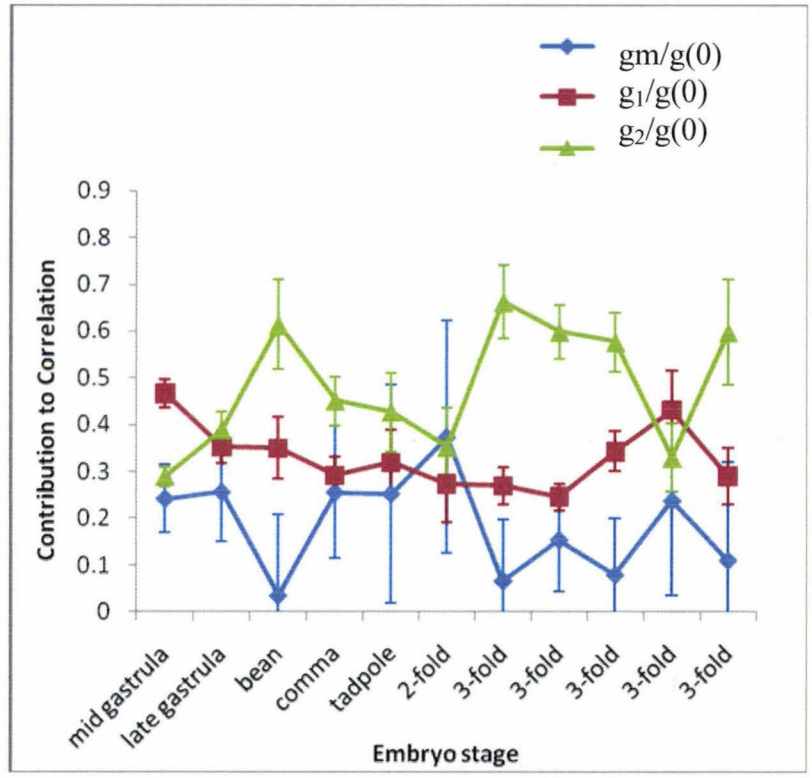

Figure 30. Changes in the proportions of mobile and immobile QDs over the development of Embryo 2 with concentration=50nM

From Figures 27 for Embryo 1 it can be seen that r_1 stays relatively constant throughout development on the order of magnitude of the resolution limit. The radius r_2 associated with the larger aggregates shows a general decrease over the course of development. However, visual inspection of the embryo images suggests that the larger aggregates do not significantly increase in size, but rather that they increase in number during development. At first, this does not appear to be consistent with the values of r_2 derived from the AC of the images. However, closer inspection reveals that the large initial value of r_2 in Figure 27 seems to correspond to the distance between nuclei, or the distance between diffuse clusters of QDs that are spaced out by these nuclei. The general decrease in r_2 over time appears to represent a shift from larger diffuse QD clusters to smaller more punctuate aggregates over development. Consistent with this is the trend in mobile and immobile contributions shown in Figure 29. As development progresses and more punctuate aggregates are formed, the concentration of immobile particles associated with those aggregates increases, while the concentration of mobile QDs decreases.

Figure 28 reveals that for Embryo 2, r_1 again stays relatively constant over development. However, its value is higher than r_1 for Embryo 1, suggesting that at higher concentrations, the size of the smaller immobile particles is just above the resolution limit. Figure 28 reveals that the r_2 values for Embryo 2 are larger than those for Embryo 1, and it also suggests that r_2 remains relatively constant throughout development. Visual inspection of the images of Embryo 2 reveals that in fact a range of aggregate sizes exist early in development, as well as over the entire course of development. Early on, there is a large proportion of small aggregates, but as the embryo develops, the proportion of larger aggregates increases. So in the case of high QD concentrations, the r_2 values derived from the AC function seems to represent an average of the range of aggregate sizes that exist.

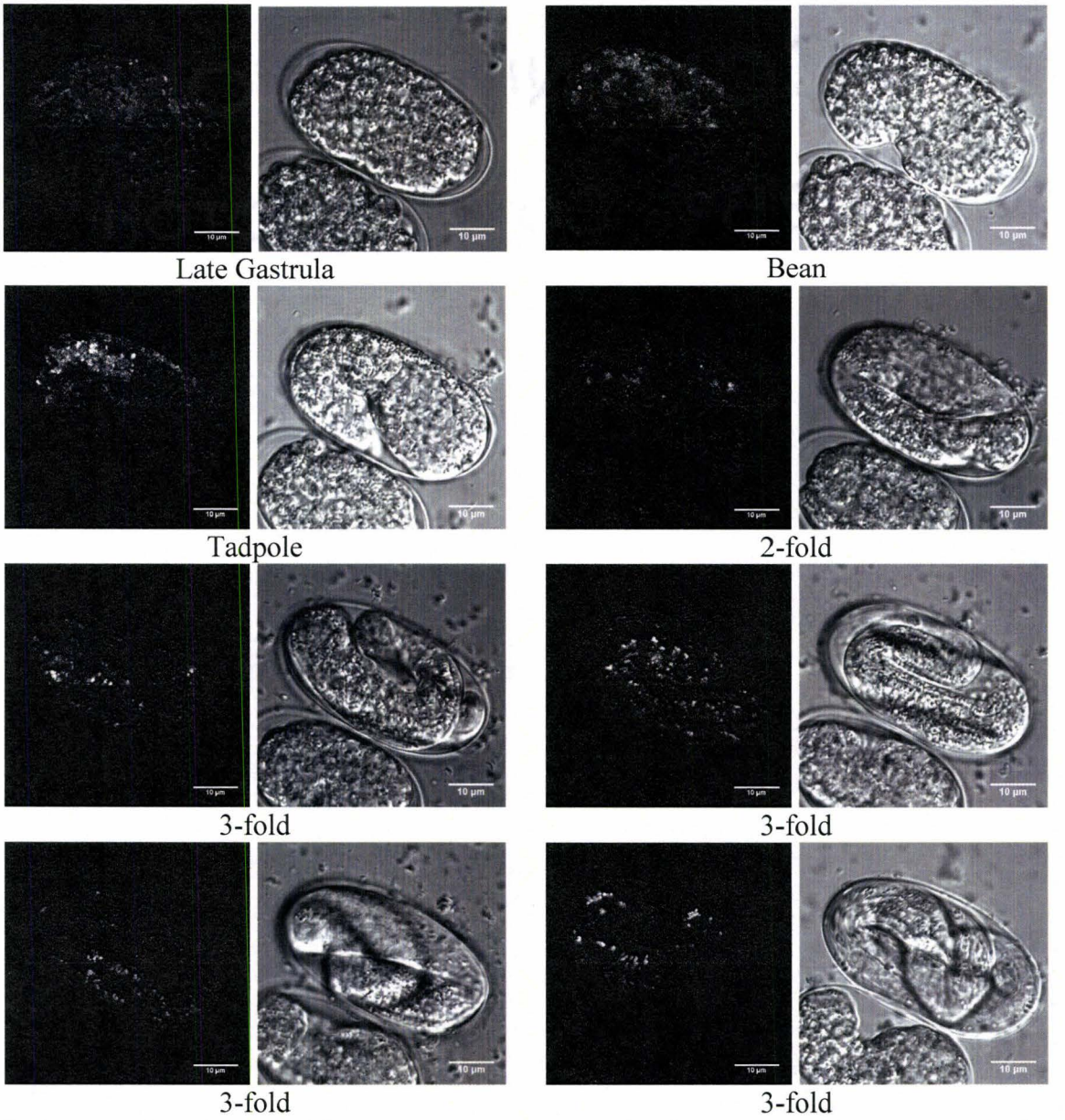

Figure 31. Embryo 3: Confocal fluorescence and DIC images showing various developmental stages of an embryo containing BSA-Alexa 555 at a concentration of 134nM. The top half of the fluorescence images were enhanced about 2 times to make the features more visible

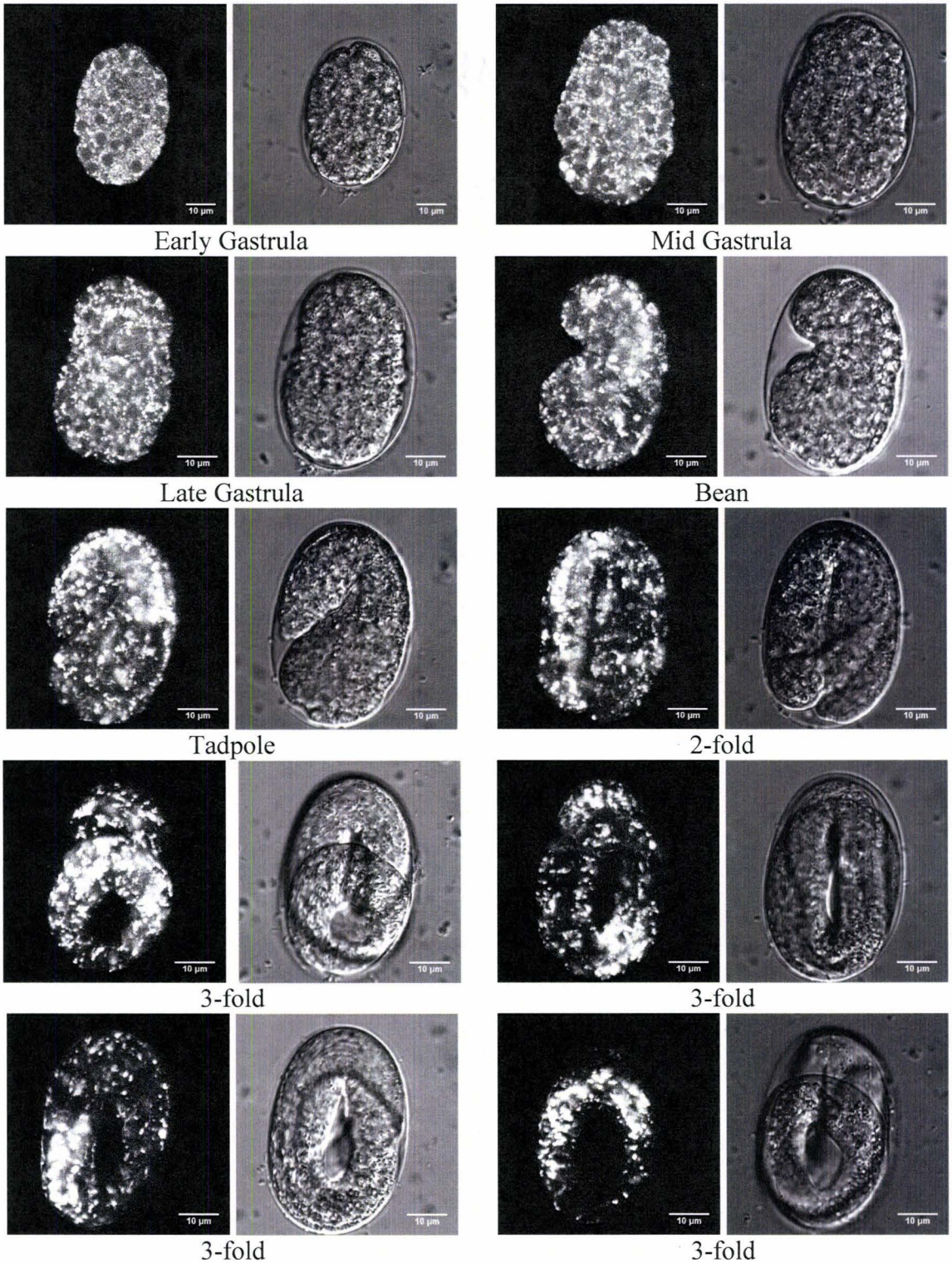

Figure 32. Embryo 4: Confocal fluorescence and DIC images showing various developmental stages of an embryo containing BSA-Alexa 555 at a concentration of 1.1μM

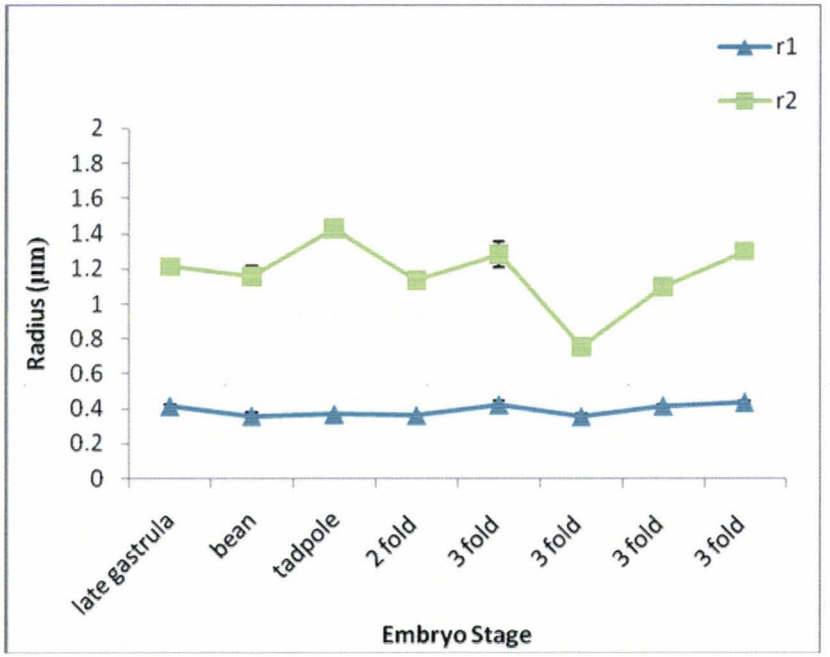

Figure 33. Changes in radii of immobile BSA-Alexa 555 aggregates over the development of Embryo 3 with concentration= 134nM

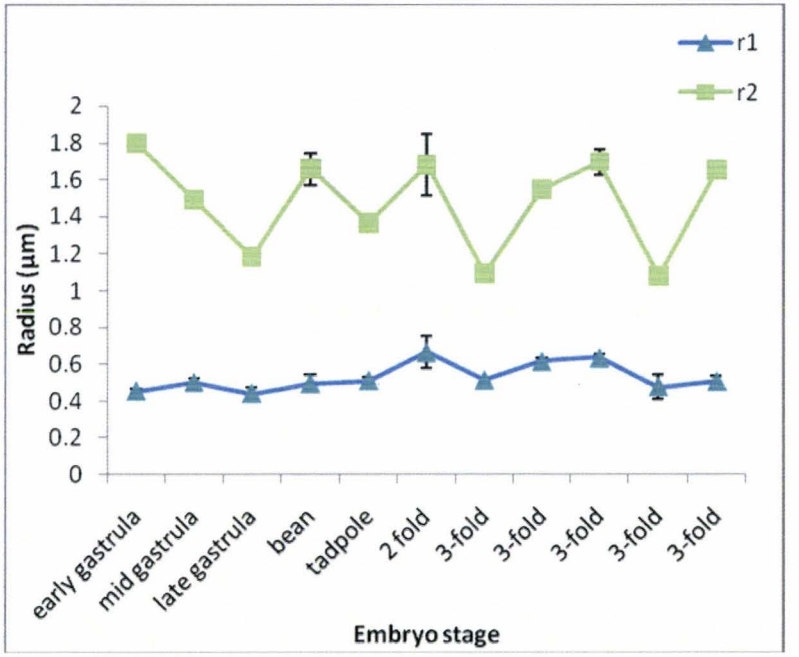

Figure 34. Changes in radii of immobile BSA-Alexa 555 aggregates over the development of Embryo 4 with concentration = 1.1µM

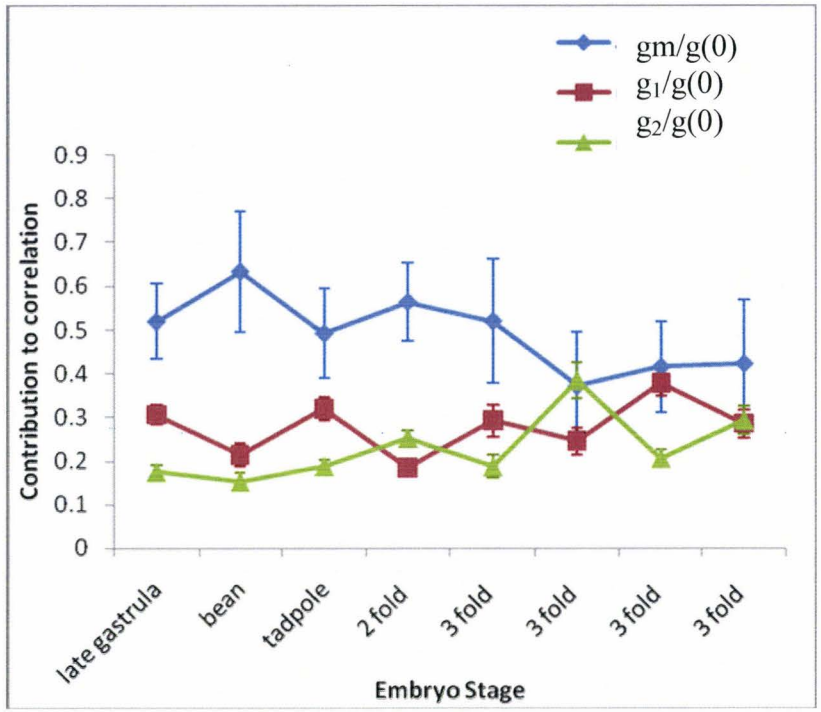

Figure 35. Changes in the proportions of mobile and immobile BSA-Alexa 555 over the development of Embryo 3 with concentration = 134nM. Here gm represents the contribution of mobile QDs, g_1 the contribution of small immobile QD aggregated and g_2 the contribution of large immobile QD aggregates

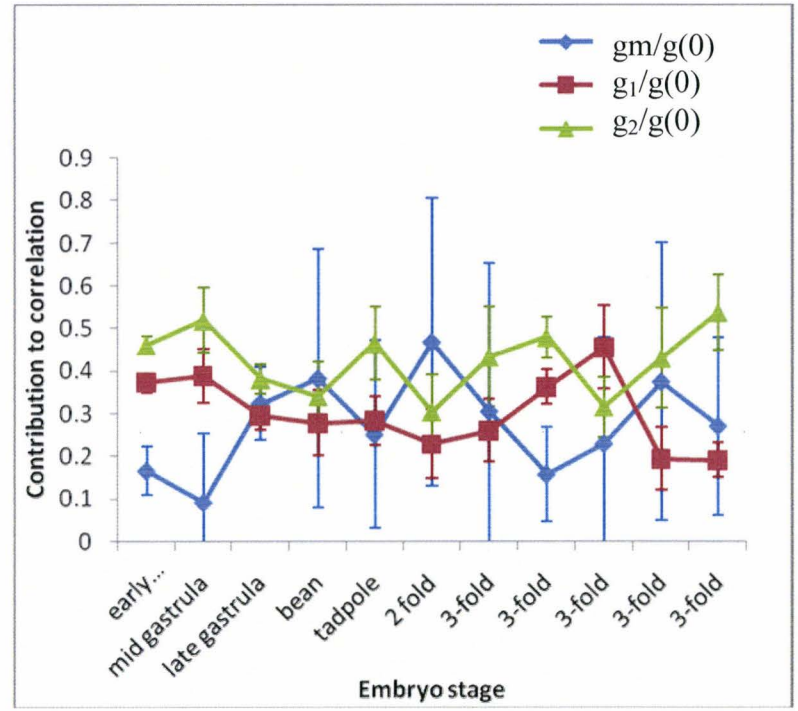

Figure 36. Changes in the proportions of mobile and immobile BSA-Alexa 555 over the development of Embryo 4 with concentration = 1.1μM

Once again, the r_1 values for Embryos 3 and 4 stay quite constant over development. As was seen with the QDs, at the lower fluorophore concentration, the contribution of mobile particles decreases over development, while the contribution of immobile particles increases. The r_2 values calculated for Embryo 4 are generally larger than those calculated for Embryo 3, and again appear to represent the average of a range of aggregate sizes. The initial decrease in the r_2 values for Embryo 4 seen in Figure 34 seems to be linked to the decreasing size of the visible nuclei.

3.4 Fluorescence Correlation Spectroscopy of QDs in *C. elegans* Oocytes

In order to better understand the dynamics of QDs at a cellular level, FCS was studied in unfertilized *C. elegans* oocytes. Measurements were taken in oocytes as opposed to the fertilized embryos, mainly because the internal motion associated with embryo development could confound FCS measurements. A typical FCS curve of QDs in PBS is shown in Figure 37 below:

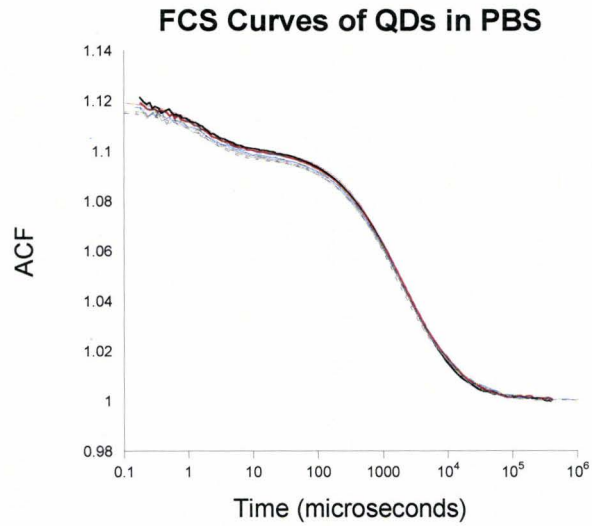

Figure 37. The FCS curves for a solution of QDs at a concentration ~6nM. The curves were fit with Equation 9

Typical FCS curves that were recorded in the cytoplasm and nucleus of oocytes containing QDs are shown in Figures 38 and 39. These curves show complex motion that could not be fit with the diffusion models discussed in section 2.6. In some positions, especially in the nucleus, no correlation of the signal was observed. In order to determine whether this motion was specific to the cellular environment, FCS curves were also recorded in the gonad arm (Figures 40 and 41) and in the space between fertilized eggs where QDs seeped in after injection (Figure 42). Curves recorded in the gonad arm were similar to those recorded in oocytes, but those recorded in the non-cellular region between eggs could be fit with the anomalous diffusion model described by Equation 10.

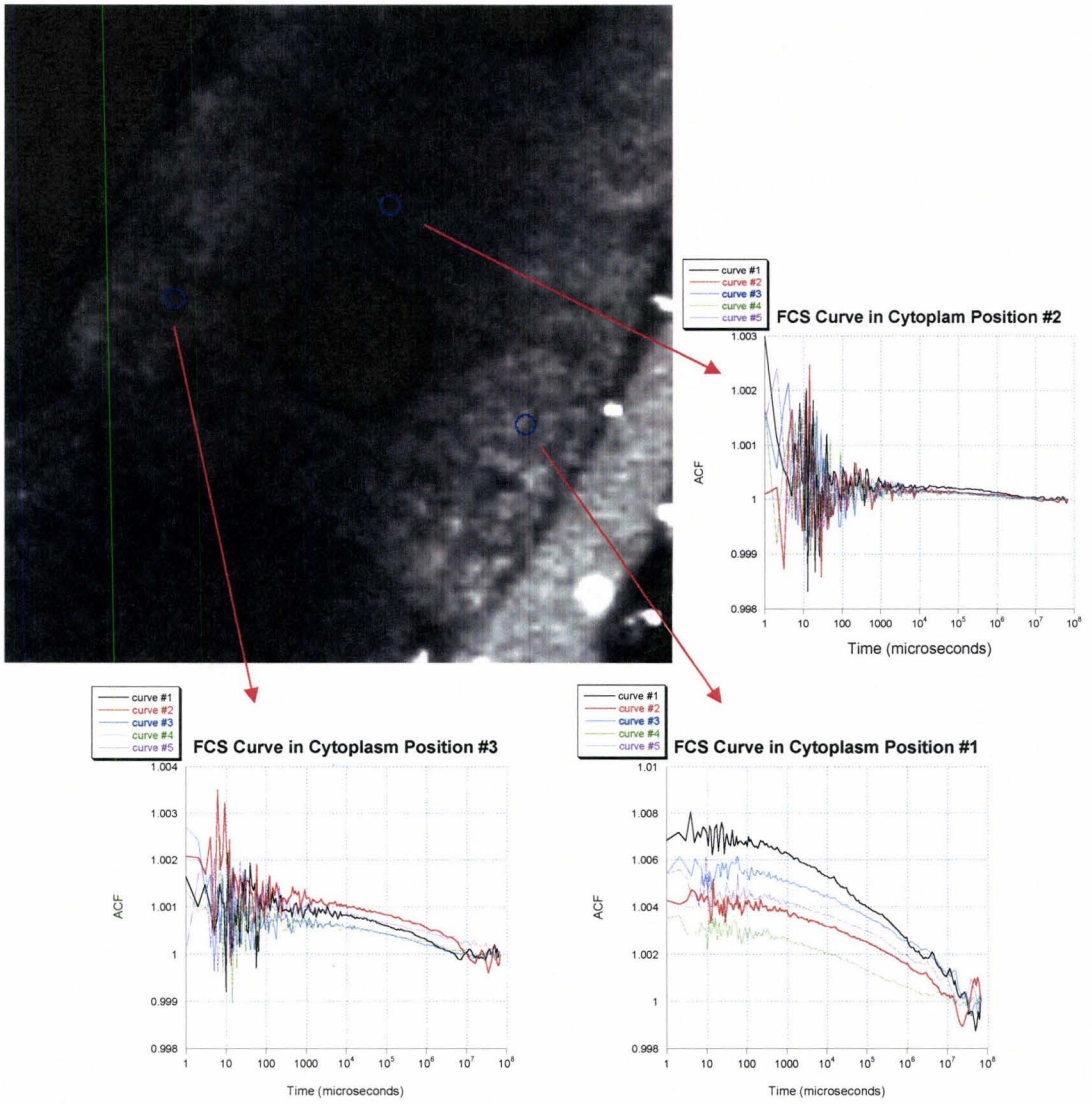

Figure 38. The FCS curves shown here were recorded at the cytoplasm positions circled in blue

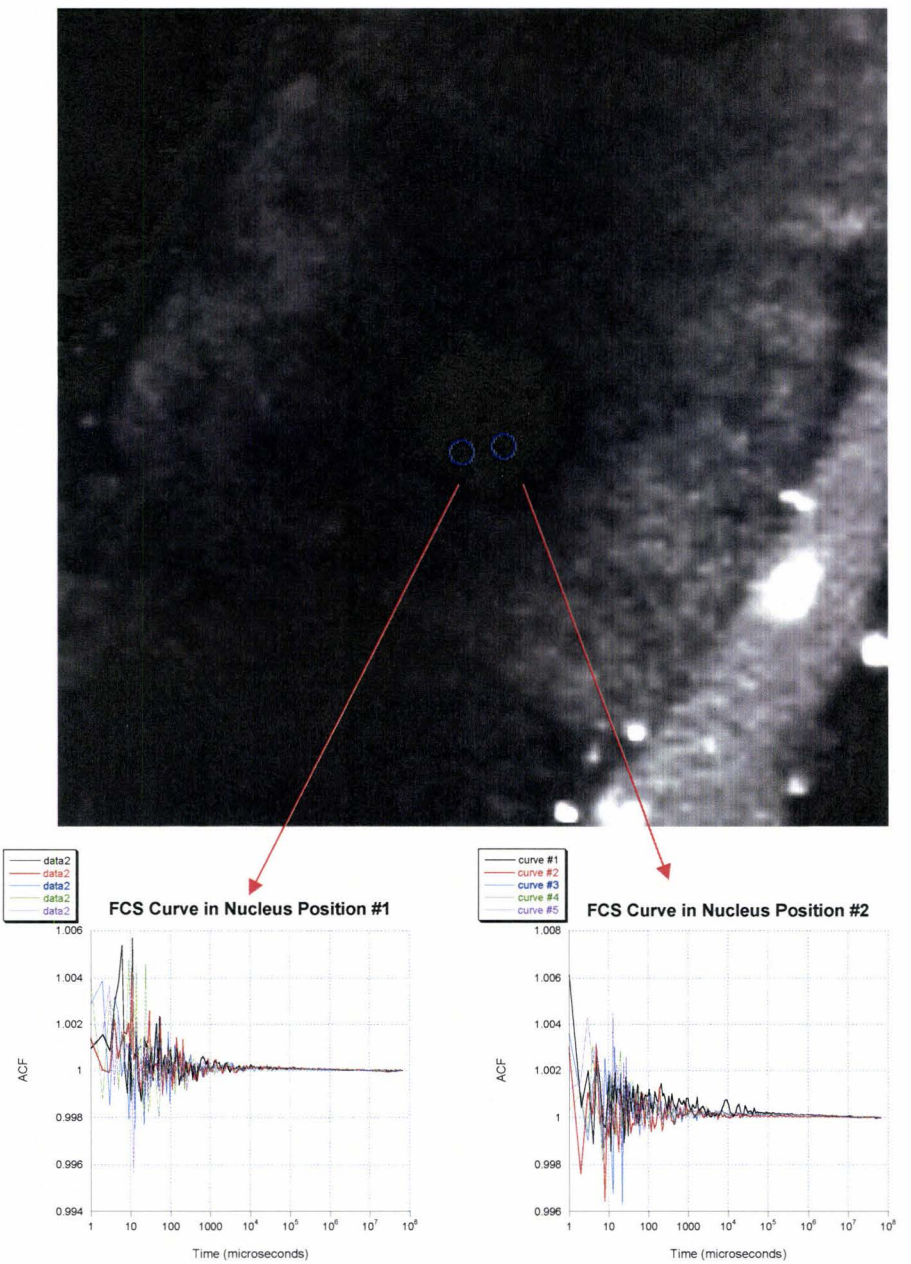

Figure 39. The FCS curves shown here were recorded for QDs in the nucleus of the oocyte shown in Figure 38

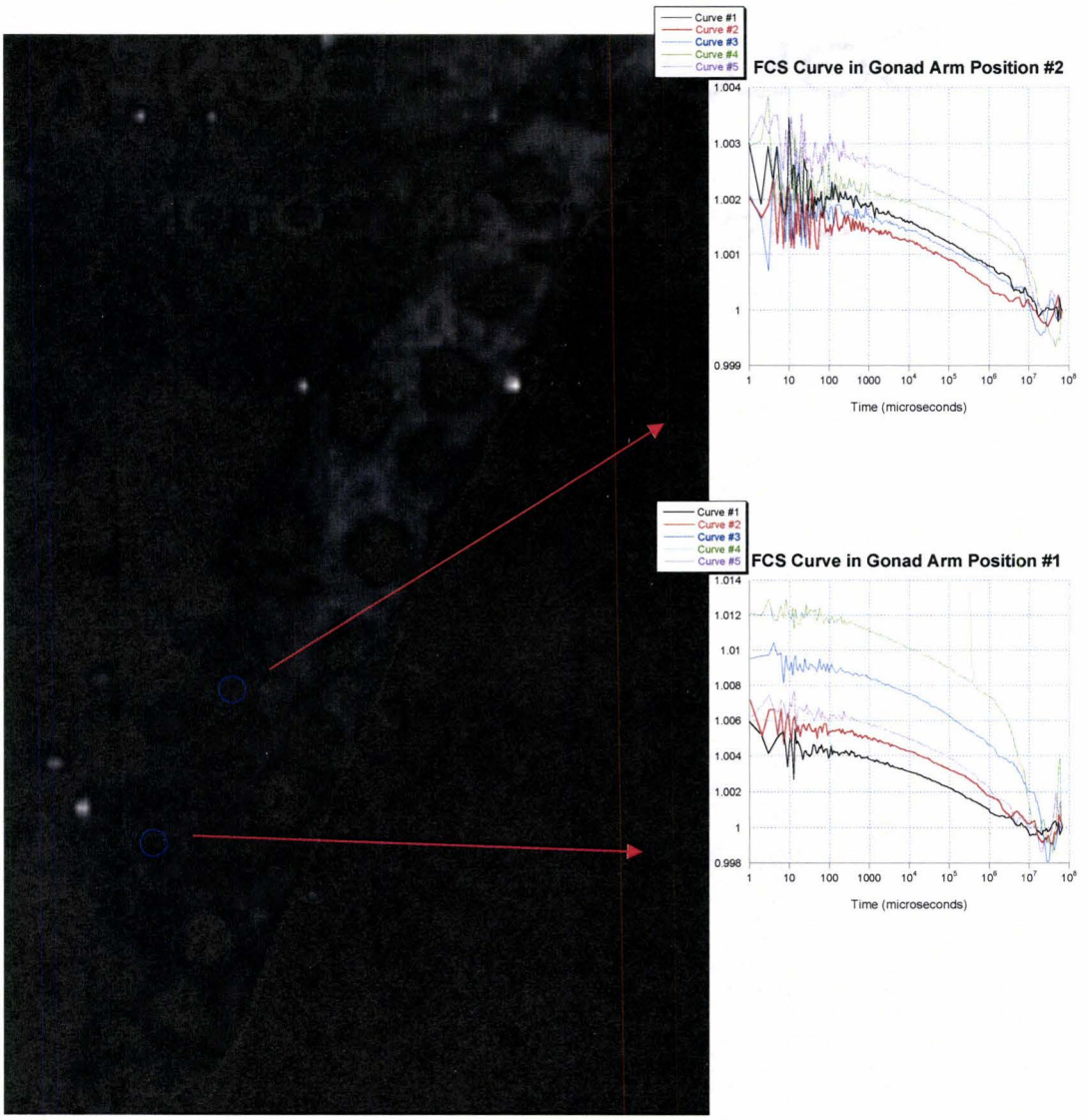

Figure 40. FCS curves recorded for QDs in the cytoplasmic region of the gonad arm

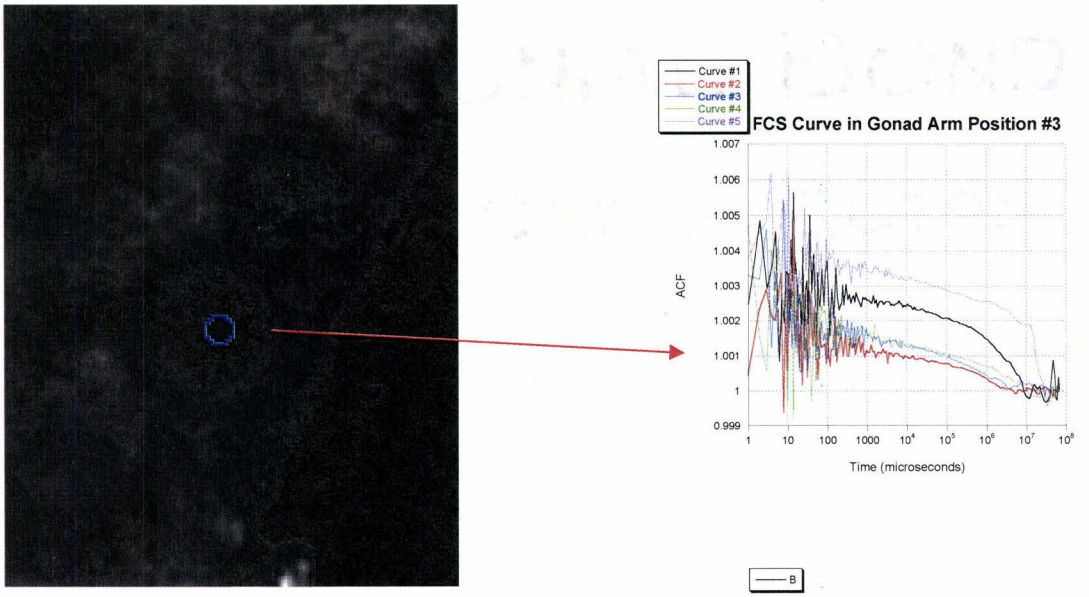

Figure 41. An FCS curve taken in a germline nucleus

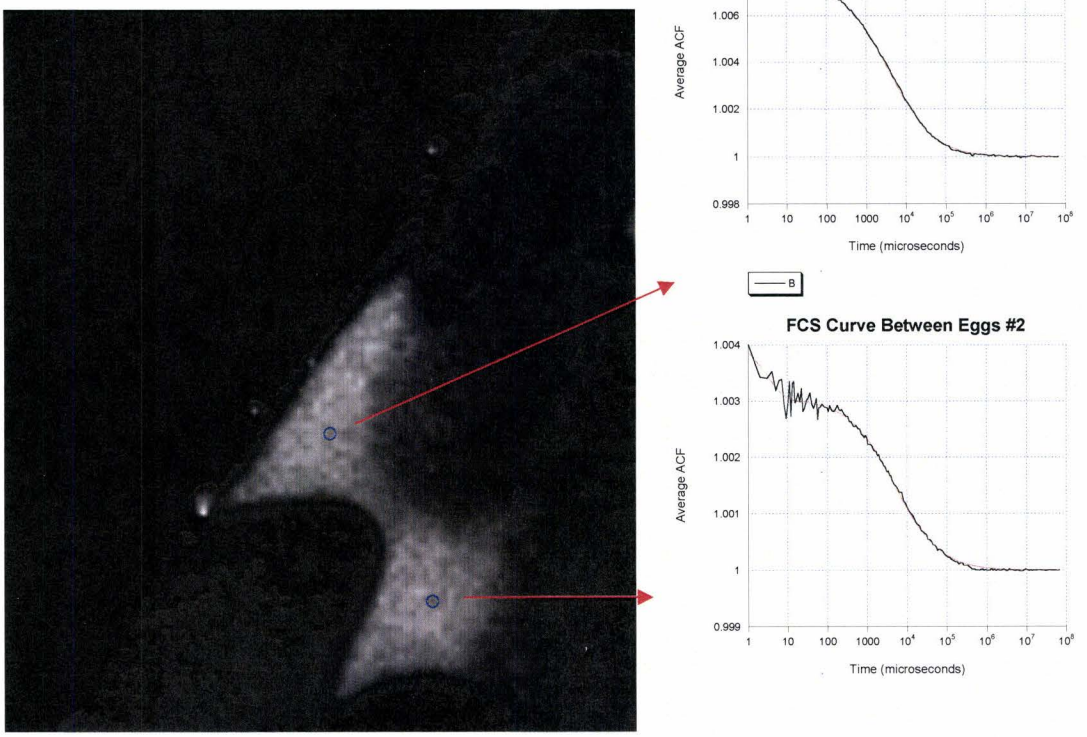

Figure 42. FCS curves of QDs recorded in the space between eggs. Curves were fit with Equation 10

The curves shown in Figures 38-41 are characteristic of those typically recorded in oocytes containing QDs. However, in a single oocyte out of the 18 studied, some curves were recorded that could be described by anomalous diffusion. A few of these curves are shown in Figures 43 and 44. However, as shown in Figure 44, curves recorded at other positions in this same oocyte again showed complex motion. In the oocyte adjacent to the one shown in Figure 43, none of the curves that were recorded could be described by anomalous diffusion.

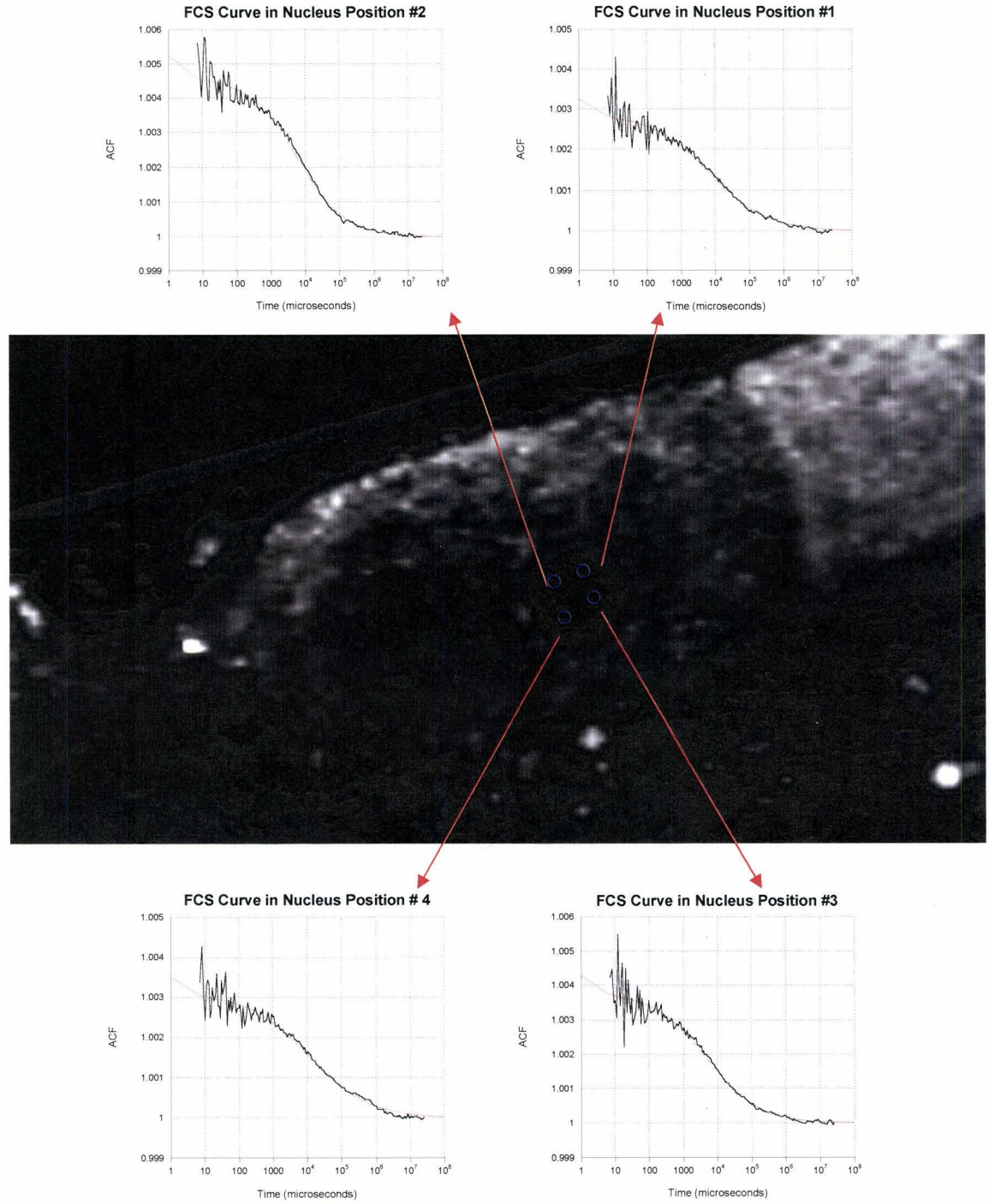

Figure 43. In one oocyte, FCS curves were recorded showing QDs undergoing anomalous diffusion in the nucleus. Curves were fit with Equation 10

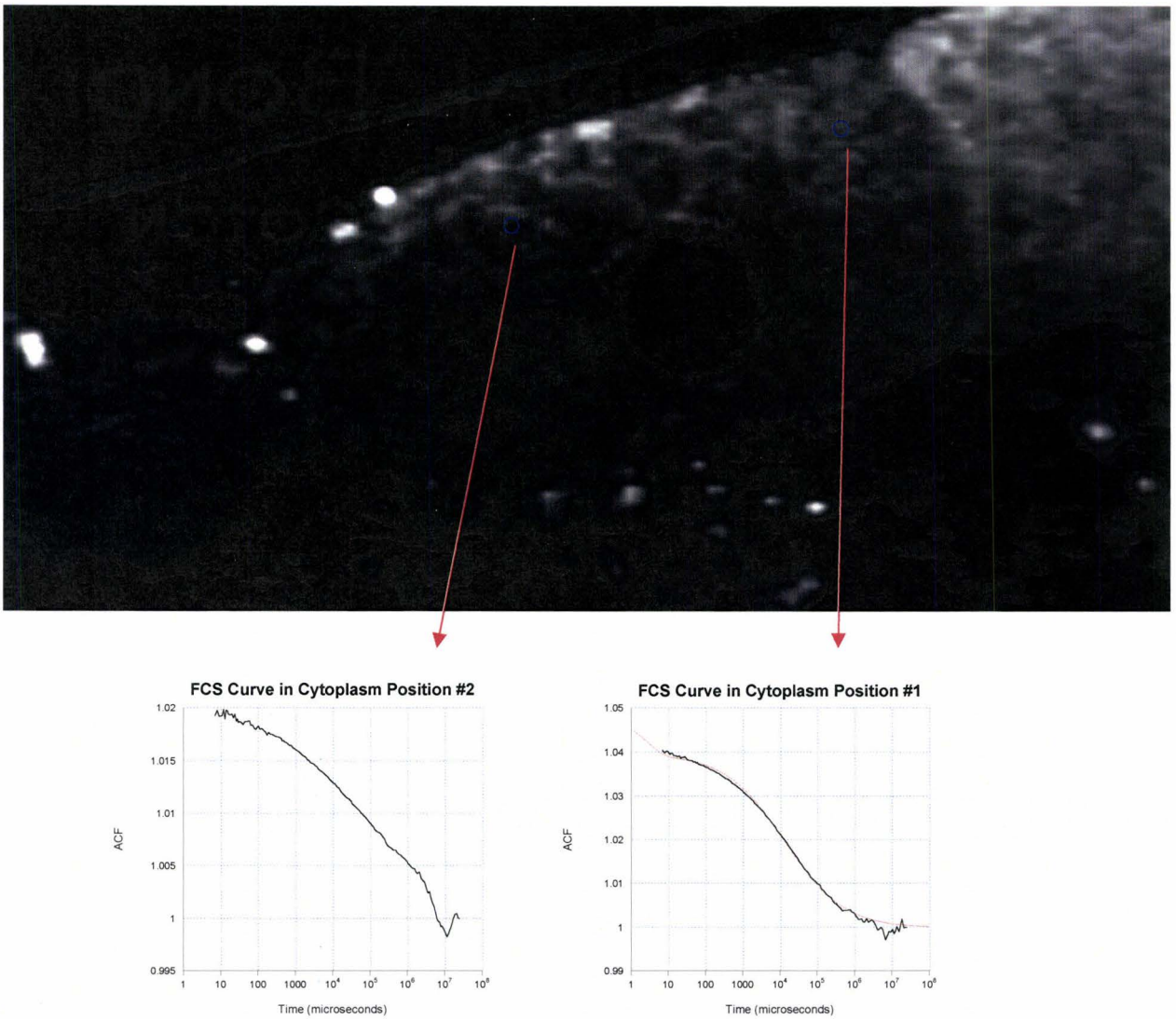

Figure 44. Although FCS curves in some cytoplasm positions indicated anomalous diffusion, in other positions QD motion was found to be complex

In order to determine whether the complex motion that was generally observed for QDs in oocytes was typical of fluorophores in general or if it was characteristic of QDs, FCS was carried out in oocytes containing BSA-Alexa 555. A typical FCS curve of BSA-Alexa 555 in solution is shown in Figure 45.

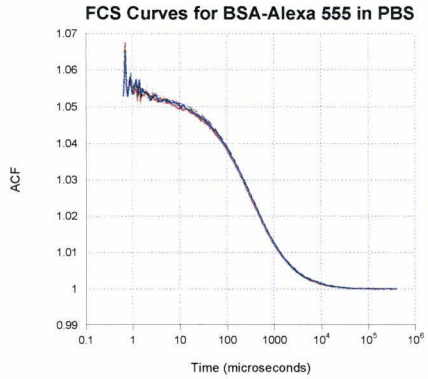

Figure 45. An FCS curve for BSA-Alexa 555 in solution at a concentration of 26nM. Curves were fit with Equation 9

FCS curves recorded for BSA-Alexa 555 in oocytes could generally be well described by anomalous diffusion. Figures 46-49 show typical FCS curves recorded in the cytoplasm, nucleus and gonad arm of a worm injected with BSA-Alexa 555.

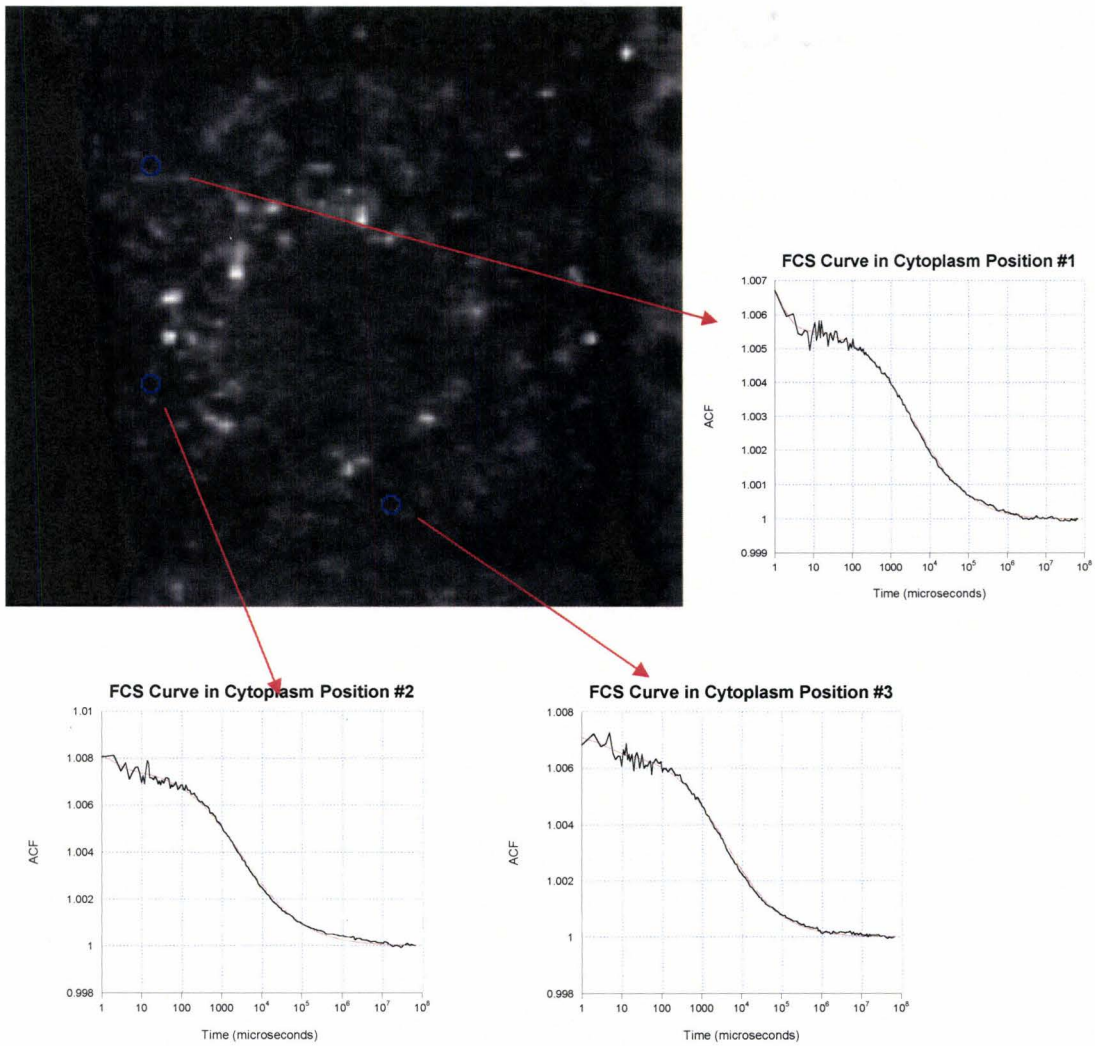

Figure 46. Typical FCS curves recorded in the cytoplasm of oocytes containing BSA-Alexa 555. Curves were fit with Equation 10

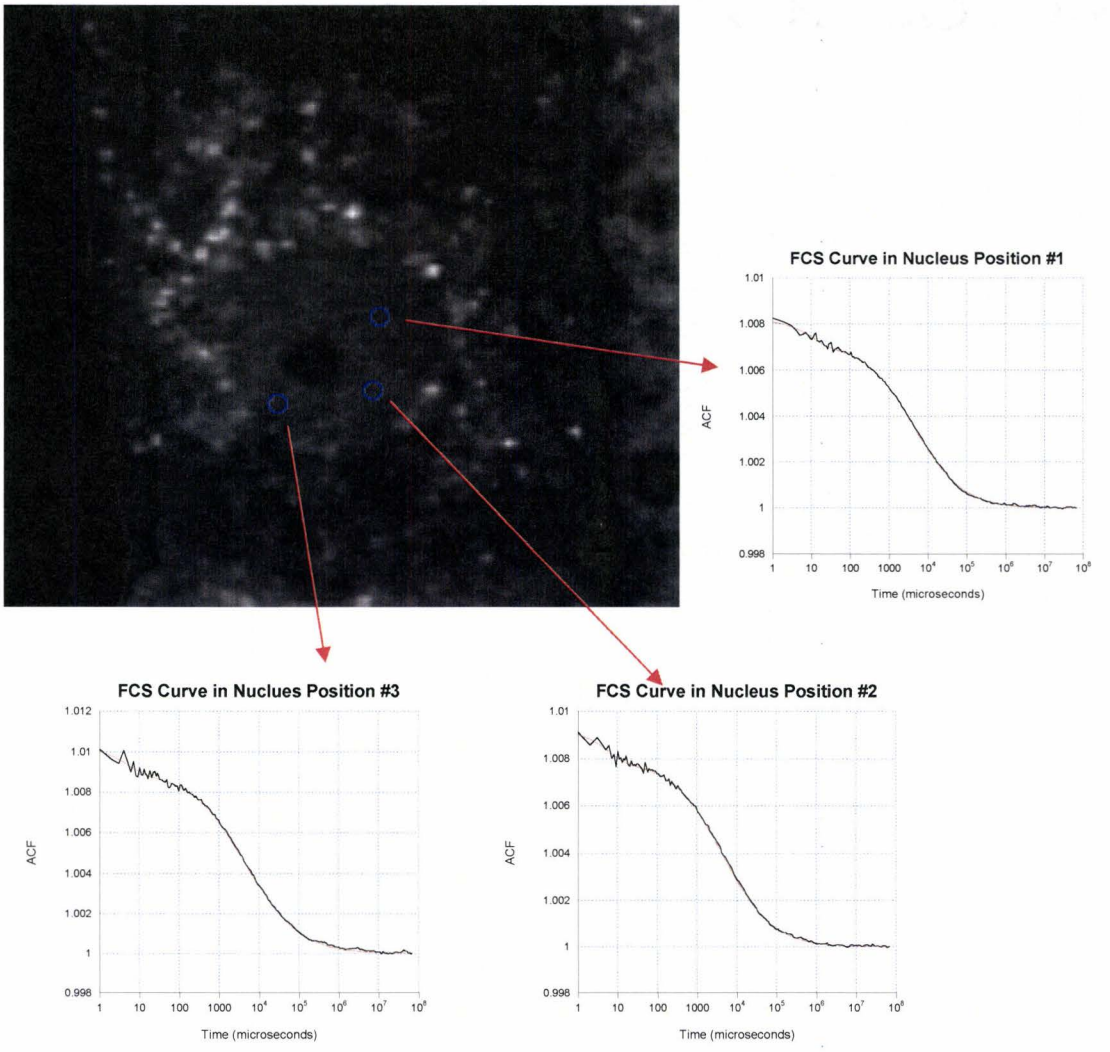

Figure 47. FCS curves recorded in the nucleus of oocytes containing BSA-Alexa 555

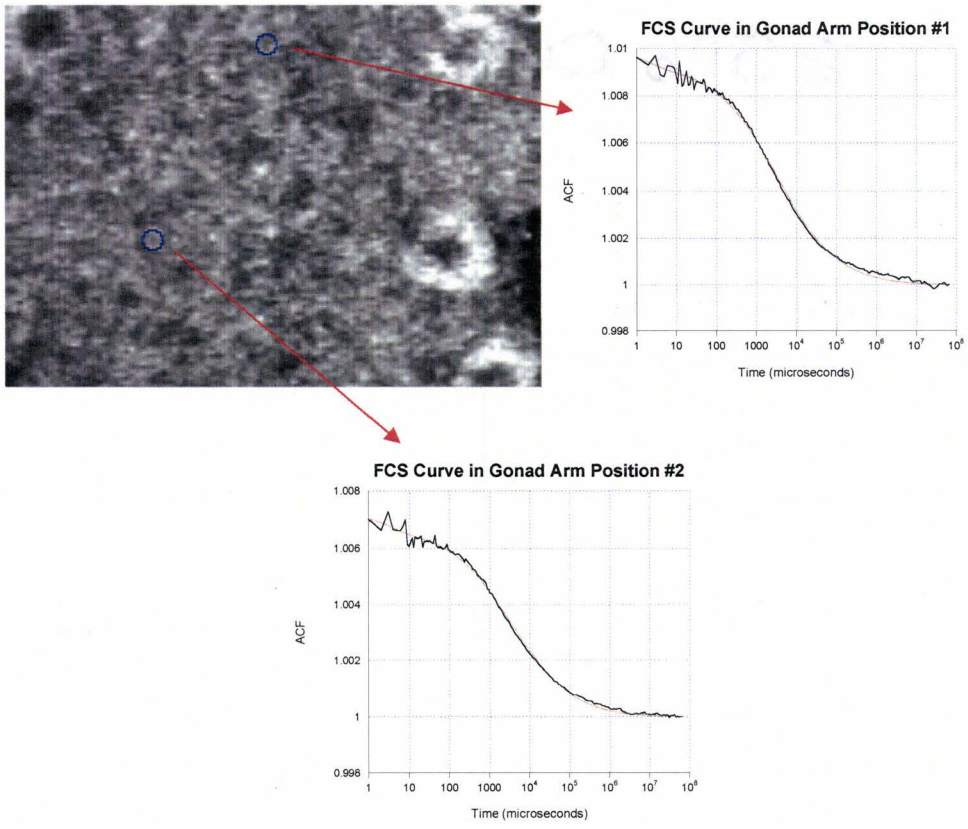

Figure 48. FCS curves recorded in the cytoplasmic region of a gonad arm containing BSA-Alexa 555

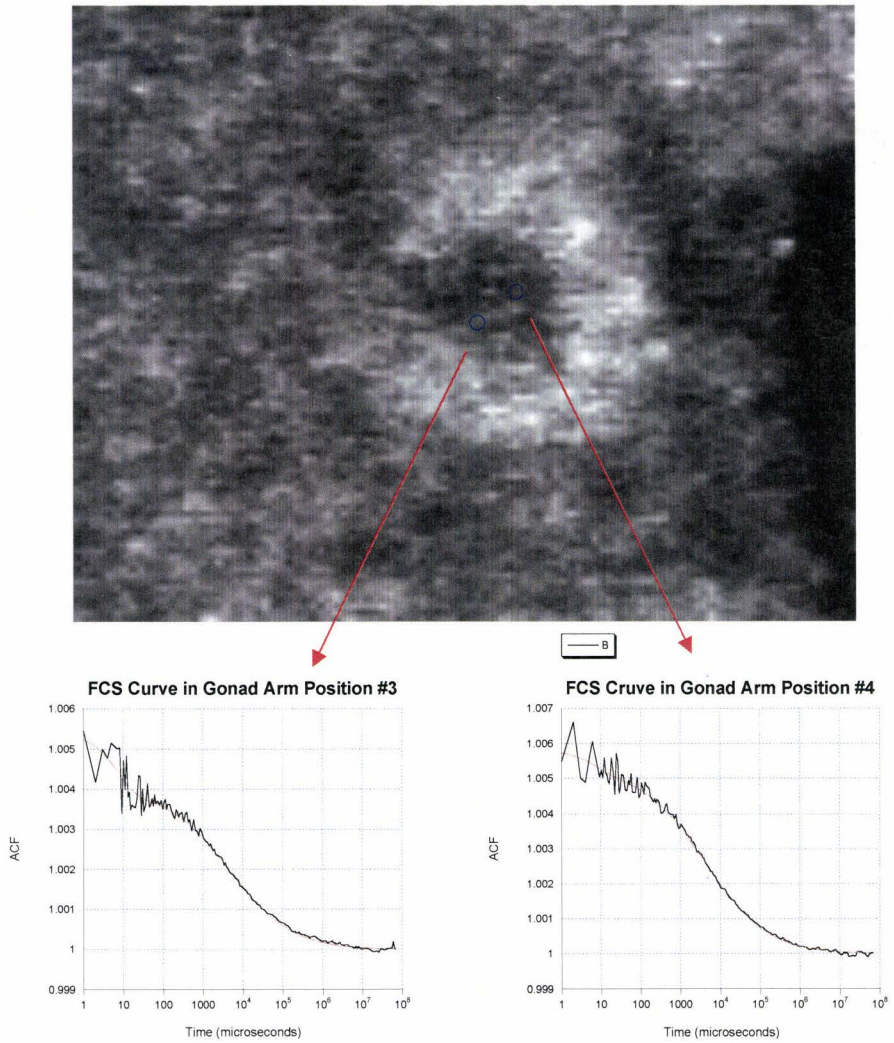

Figure 49. FCS curves recorded in a germline nucleus containing BSA-Alexa 555

A summary of the number and quality of measurements taken in the cytoplasm and nucleus of oocytes containing QDs and BSA-Alexa 555 is shown in Table 2. Curves were only fit if they were reproducible in the same position, and if the fitting program used could successfully find a solution for them using the anomalous diffusion model. Diffusion coefficient and viscosity values were calculated using Equations 4 and 5.

Table 2. A summary of the total number of FCS measurements taken in the nucleus and cytoplasm of oocytes containing QDs and BSA

	# of oocytes studied	total # of positions in cytoplasm	total # of curves taken in cytoplasm	% cytoplasm curves that could be fit	total # of positions in nucleus	total # of curves taken in nucleus	% nucleus curves that could be fit
QDs	18	172	1025	5.3%	82	446	8.7%
BSA-Alexa 555	9	42	155	80%	31	155	92%

Tables 3 and 4 summarize the parameters derived from the autocorrelation curves taken in oocytes and the gonad arms of worms injected with BSA-Alexa 555 and QDs.

Table 3. A summary of the main parameters derived from autocorrelation curves taken in oocytes and gonad arms containing BSA-Alexa 555. These results are the average of measurements taken over 3 days. For an example of the range of measurements recorded during a single experiment or in a single oocyte, refer to Appendix C. CPP=Counts per particle. Viscosity of PBS assumed to be the viscosity of water at 21°C.

	PBS	Cytoplasm	Nucleus	Gonad Arm Cytoplasm	Gonad Arm Nucleus
Anomalous Diffusion Exponent	0.947±.004	0.60±0.02	0.65±0.03	0.55±0.01	0.57±0.02
Diffusion Coefficient (μm^2/sec)	72.3±1.5	4.8±1.5	5.5±2.2	4.0±2.4	3.1±2.1
Apparent Viscosity in vivo					
Viscosity of water	1 [90]	20	20	30	40
CPP in solution					
CPP in cell		5.3	4.8	4.8	15.2

Table 4. A summary of the main parameters derived from autocorrelation curves taken in QD injected worms. The cytoplasm and nucleus results are averages of measurements taken in the oocyte depicted in Figure 43

	PBS	Cytoplasm	Nucleus	interstitial space
Anomalous Diffusion Exponent	0.92±0.01	0.53±0.01	0.57±0.03	0.69±0.03
Diffusion Coefficient (μm^2/sec)	22.6±0.5	3.9±0.4	6.3±0.6	4.7±0.5
Apparent Viscosity in vivo				
Viscosity of water	1	6	4	6
CPP in solution				
CPP in cell		3.5	251	65

From the autocorrelation functions recorded, the concentration of BSA-Alexa 555 was calculated to range from 16→607nM in the cytoplasm and 19→418nM in the nucleus. Injection concentrations ranged from 140→340nM. The count rate for BSA-Alexa 555 was recorded to be about 1.4 times higher in the nucleus than in the cytoplasm.

For the oocyte shown in Figure 43, the concentration of QDs in the cytoplasm was calculated from the autocorrelation curves to be about 11nM in the cytoplasm and 183nM in nucleus. In this case, QDs were injected at a concentration of about 80nM. The count rate for QDs was generally found to be about 4 times higher in the cytoplasm than in the nucleus.

Chapter 4 Discussion

4.1 Quantum dots do not visibly interfere with embryo development

There are a number of considerations that led to our choice of the *C. elegans* embryo as a model for nanotoxicity. Unlike the numerous reports of QD toxicity using cell lines, our model system allows us to look at the response of an entire organism, instead of just the response of single independent cells. As discussed in detail in Chapter 1.4, *C. elegans* has already been used extensively as a model for toxicity, due to its similarities with humans in genetics and stress responses. The embryo in particular is a good environment to test toxicity, as embryogenesis depends on well coordinated, intricate cell signaling that would presumably be very sensitive to environmental insults. Laser cell ablation experiments, in which specific cells in the *C. elegans* embryo were targeted and destroyed, have shown that except at very late stages of embryogenesis, the death of one cell causes the death of the entire embryo [59].

One advantage of using the *C. elegans* embryo as opposed to other embryo models is that is that injection of foreign material need not be carried out directly into the embryo, which in itself can be a damaging process. Instead, foreign material can be injected into the gonad arm and then become incorporated into developing oocytes. At least two other studies have reported on the incorporation of injected foreign material into *C. elegans* embryos. In the first study, calcium green and rhodamine dextran dyes were injected for the purpose of studying intracellular calcium concentrations [91], and in the second study, polyethylene-glycol (PEG) coated carboxyl terminated polystyrene nanoparticles were injected for the purpose of studying cellular viscosity [92]. Although these studies were not directly concerned with toxicity, they did report that embryos incorporating the foreign material were viable.

Our results indicate that CdSe/ZnS QDs of concentrations up to 80nM do not interfere with oocyte development or fertilization. Since cadmium is known to be toxic to adult *C. elegans* [65, 67, 68] , it is likely that both the ZnS and BSA coatings protect the core from degradation. This is consistent with previous studies that found that passivating and organic coatings reduce QD toxicity [43, 47, 48, 56]. For instance, a recent study concluded that CdSe QDs were toxic to mouse embryos, but that this toxicity was significantly reduced when the QDs were passivated with ZnS [56].

At this time it is not clear what caused the case of the abnormal embryo depicted in Figure 18, especially since it had a relatively low concentration of QDs. A previous study that investigated the toxicity of phospholipid micelle encapsulated CdSe/ZnS QDs on Xenopus embryos only observed abnormalities at very high injection concentration, which exceeded $5*10^9$ QDs/cell [38]. It was suggested that this was due to changes in the osmotic equilibrium of the cell. Another study with zebrafish embryos also found dose dependent toxicity [55]. The QDs used in their study were the same as the one used in this current study, except that they were conjugated with streptavidin. At injection concentrations of 100nM, 85% were viable, but when this was increased to 200nM, viability was reduced to 75%. Although the injection concentrations used in our study were greater (up to 1.6μM), it is difficult to compare results since dilution factors between studies could be different.

As can be seen in Table 1, the sample size for the QDs lacking the BSA coating was small. This was due to the difficulty of introducing them into the oocytes, resulting from their inability to disperse freely in the gonad arm, as depicted in Figure 16. Additionally, injection of these uncoated QDs was difficult, as they tended to aggregate and clog the injection needle. A previous study found that carboxyl terminated polystyrene nanoparticles injected into *C. elegans* aggregated at the walls of the gonad arm. The investigators attributed this to the tendency of carboxyl to interact with biomolecules [92]. When these nanoparticles were coated with polyethylene-glycol, this problem was overcome. So it is possible that QDs with a different conjugation, such as streptavidin would not suffer from aggregation in the gonad arm.

4.2 Foreign material introduced into the C. elegans embryo aggregates in both a dose and time dependent manner

Although the QDs show no apparent toxicity to the *C. elegans* embryo, the embryo still responds to the nanomaterial introduced into it by packaging it into aggregates. A new image analysis technique was developed in this study in order to provide insight into this process. As discussed in Chapter 3.3, the technique characterizes the size of aggregates and also quantifies the contributions of mobile and immobile QDs at each stage of development.

From analysis of images of both embryos containing QDs and BSA-Alexa 555, it is clear that the degree of aggregation is dependent upon the dose. At higher concentrations, the aggregates are larger and there are more of them earlier in development.

4.2.1 Trends in the contributions of mobile and immobile particles

At first glance it may appear from Figure 30 that no clear trend exists for the changes in the mobile and immobile QD populations in Embryo 2. However, by considering the total contributions of immobile QDs to mobile QDs, a clearer picture of what is happening emerges:

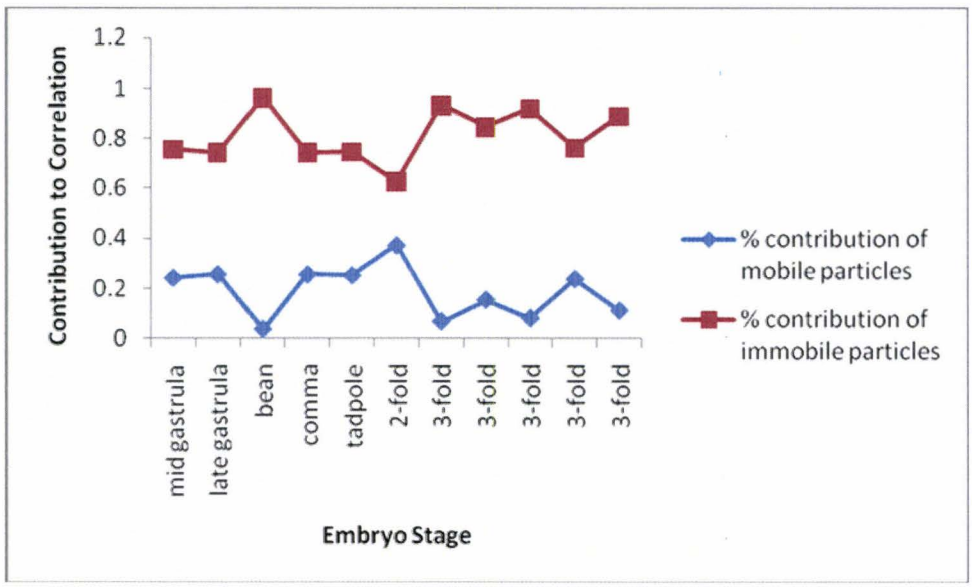

Figure 50. Total contributions of mobile and immobile particles for Embryo 2 containing 50nM of QDs

Contrast this now to the total population of mobile and immobile QDs for Embryo 1:

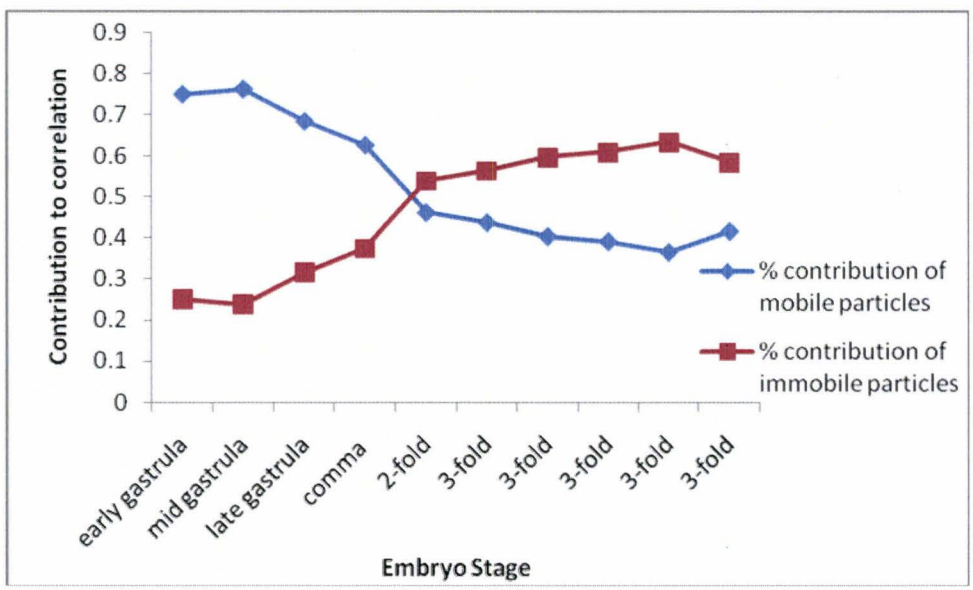

Figure 51. Total contributions of mobile and immobile particles for Embryo 1 containing 3nM of QDs

These graphs suggest that the trend of increasing QD immobility seen for Embryo 1 is not also observed for Embryo 2 because the immobile population of Embryo 2

already dominates from an early stage. This is consistent with the high degree of aggregation that can be seen to occur early in development for Embryo 2.

The contrast in the trends of the total contributions of mobile and immobile particles seen between Embryos 3 and 4 is similar to the contrast seen between Embryos 1 and 2:

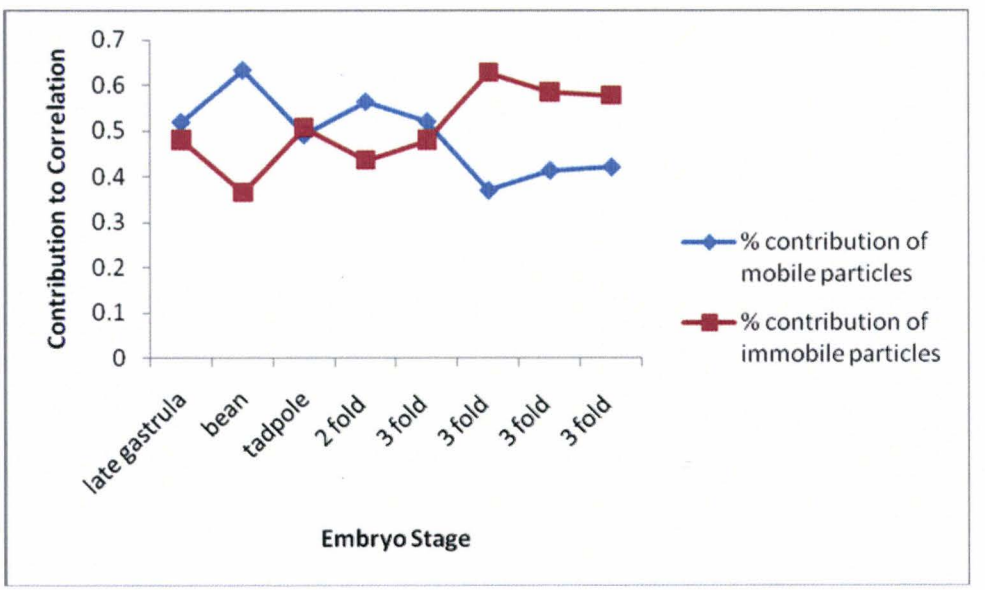

Figure 52. Total contributions of mobile and immobile particles for Embryo 3 containing 134nM of BSA-Alexa 555

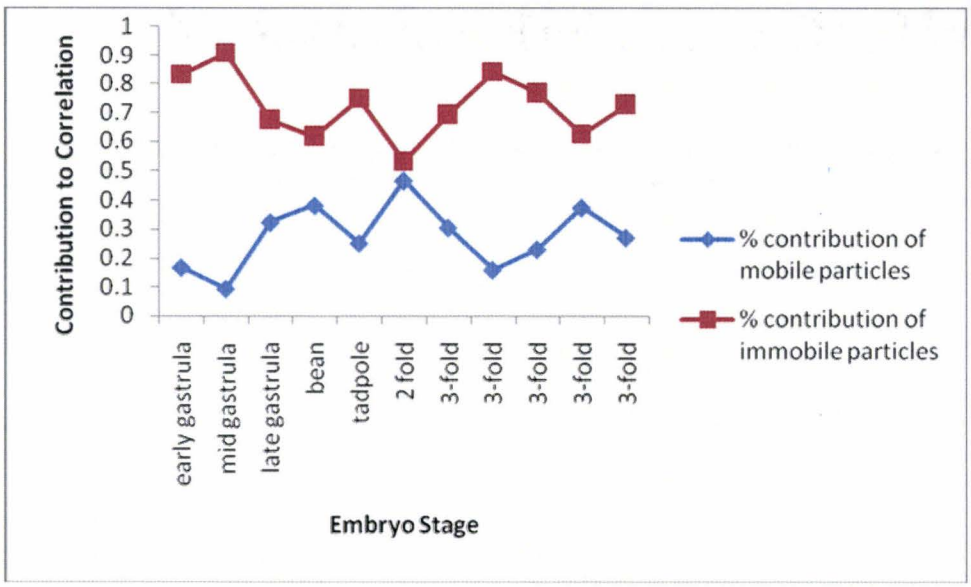

Figure 53. Total contributions of mobile and immobile particles for Embryo 4 containing 1.1μM of BSA-Alexa 555.

In this case the concentration effect is not as pronounced as it is with the QDs, most likely because the difference in concentration is not as great, and the low concentration of BSA-Alexa 555 in Embryo 3 is still significantly higher than the low concentration of QDs in Embryo 1.

4.2.2 General conclusions from the image analysis

Figures 50-53 reveal that the initial population of mobile fluorophores is very much concentration dependent. At the lower concentrations of both of the fluorophores studied the population of mobile particles starts off higher than that of the immobile particles, and then decreases over development until the population of immobile particles dominates at the 3-fold stage. In contrast, when introduced at a high concentration, the population of mobile particles is low when imaging starts and stays lower than population of mobile particles throughout development.

It is not clear if the large initial contribution of immobile particles at high fluorophore concentrations is the result of an upregulated response by the embryo to the foreign material, or if it results from over saturating the small embryo volume with a high concentration of foreign material. What does seem to be obvious is that the embryo

response to the foreign material is not specific to QDs or inorganic material, but rather it is a general response to foreign material introduced into it. Fluorophore aggregation was not observed to occur over time in early embryos that were damaged by the mounting processes. This further suggests that the aggregation process results from active sequestering of the foreign material into isolated complexes by the developing embryo, rather than by passive aggregation of the material.

The *C. elegans* embryo may be using a detoxification technique to isolate the foreign material introduced into it. This may be comparable to detoxification processes used by other cells, such as hepatocytes, which have known methods of isolating toxins such as Cd^{2+} into inert complexes [47].

Other studies have observed aggregation of QDs in cellular environments. However, in these cases the QDs were introduced into the cells in vesicles via endocytosis, which was the cause of their aggregation. [19, 24, 49]. Aggregation was seen in some of the developing tissues of zebrafish embryos injected with QDs [39]. However, this did not appear to be an embryo response, since when QDs were sonicated before injection, aggregation was avoided. One study observed that exposing QDs to a saline solution results in their aggregation [85]. So if the *C. elegans* embryo has high salt concentrations, then it is possible that this is contributing to the QD aggregation.

4. 3 Results from Fluorescence Correlation Spectroscopy

One of the biggest limitation of FCS is photobleaching [87]. The use of more photoresistant fluorophores, such as QDs, may help to overcome this limitation. This would make FCS capable of detecting much slower events, such as the dynamics associated with very slowly moving proteins.

However, FCS on QDs has its own challenges. QD blinking behavior has complicated the analysis of their AC curves. This is because unlike organic fluorophores that have well defined exponential photophysics attributed to their triplet state transitions, QD blinking occurs over a wide range of time scales ranging from 200μs-100s [1]. This

results in a time scale overlap between blinking and diffusion, which can make fitting FCS curves for QDs challenging [84].

It has been observed that as the power is increased, the effects of blinking of the CdSe/ZnS QDs also increases, resulting in FCS curves with decreased amplitude and a more anomalous shape [1, 93]. A number of fitting models have been developed to account for this, and are discussed in section 2.6.2. However, at low excitation power, the effects of blinking are not pronounced [1]. In our study, low powers below 10μW were typically used, and as discussed in section 2.6, an exponential decay fit was determined to be the most appropriate to account for the photophysical term of the QDs used here.

Despite the challenges involved in fitting QD data, the potential for using QDs for FCS studies in a biological context has been demonstrated in one study. This study used two-photon cross-correlation FCS to study the biotin-streptavidin ligand-receptor system [64, 94]. Cross-correlation allowed the issue of blinking to be avoided, as it was found that blinking was not synchronized between QDs. QDs' narrow emission and well separated spectra eliminates the problem of cross-talk that occurs with traditional dye pairs. In addition, QDs with different emissions can be excited by a single laser due to their broad emission. Their superior brightness allows for the interaction of very low concentrations of the species of interest, compared to the concentrations accessible by traditional dyes. However, the relatively large size of QDs compared to organic fluorophores may interfere with the biological interactions being studied. The results of this study concluded that the streptavidin-biotin binding constant was about 5 orders of magnitude less when bound to CdSe/ZnS QDs. This can be explained by considering that the forward reaction rate for binding was reduced due to the QD bulkiness and the fraction of the QD surface that was bioactive.

4.3.1 FCS reveals aggregation of QDs in the oocyte environment

As exemplified in the AC curves shown in Figures 38 and 39, FCS curves recorded in the oocyte environment could rarely be described by established diffusion models. The curves suggest aggregation and possibly strong interactions with biomolecules in the cellular environment at several different time scales. The lack of any correlation in some locations, especially in the nucleus (Figure 39), indicates complete immobility at these locations. At this time it is not known whether these strong interactions originate from the QD itself or from its coating. However, it is clear that they are related to interactions with the cellular environment, since curves recorded in the space between eggs (Figure 42) could all be described well by anomalous diffusion.

As mentioned earlier, a previous study found that carboxyl terminated polystyrene nanoparticles interacted strongly with biomolecules in the gonad arm, but that coating the particles with PEG minimized this effect [92]. Another study found that carboxyl-terminated QDs could not be efficiently loaded to oligonucleotides and suffered from non-specific binding to oligonucleotides as well as other biological tissues, but that hydroxyl-terminated quantum dots did not suffer these problems [95]. So it is possible that the carboxyl coating on the QDs is the source of the non-specific interactions that are observed. Although the QDs used in this study were coated with BSA, there is no way of knowing whether or not they retained their coating after injection.

As already mentioned, high salt concentrations have been observed to cause QD aggregation, and this may be happening in the oocyte. The group that observed this used FCS to study CdSe/ZnS QD properties in a saline solution, as an indication of what their behavior would be like in a cellular environment [85]. It was found that the average fluorescence count rate decreased by about 16- fold due to quenching, the diffusion time increased, and the number of QDs detected in the focal volume dropped by about 12-fold, all indicative of aggregation. Something similar may be happening to the QDs in the oocyte environment, and this may be contributing to the reduced mobility of FCS curves recorded in the oocytes.

In the single oocyte in which FCS curves were recorded that could be fit (Figures 43-44), these curves indicated that the diffusion of the QDs was anomalous, and that the motion was more anomalous in the cytoplasm than in the nucleus. The motion of the QDs was also slower in the cytoplasm compared to the nucleus. It is important to note that less than one quarter of the curves recorded in this oocyte could be described by anomalous diffusion, and that the rest showed the complex motion seen in all of the other oocytes. Thus the behavior of the QDs in this cellular environment is very heterogeneous.

As indicated in Table 4, it appears that the CPP is lower in the oocyte compared to in solution, but much more so in the nucleus than in the cytoplasm. One obvious explanation for this is that the concentration in the nucleus is being overestimated even more so than in the cytoplasm. This can be understood by comparing the amplitudes of the ACF in the cytoplasm (Figure 44) and the nucleus (Figure 43). As mentioned earlier, the concentration is proportional to the inverse of the amplitude of the autocorrelation. Although the amplitude of the autocorrelation function in the nucleus is about ten times lower than that in the cytoplasm, the concentration of QDs is clearly less in the nucleus, since the count rate is about four times lower there. Another indication that the concentration in the nucleus is overestimated, is that it is even higher than the concentration of injected QDs. Using the calibration curve in Figure 13, the actual concentration of QDs in this oocyte was calculated to be about 10nM in the cytoplasm, which is close with the concentration calculated from the AC curves taken in the cytoplasm.

This overestimation of concentration results from the presence of a high background against which fluorescence fluctuations are recorded. The main contributor to this background is the fluorescence from immobile QDs. With a traditional fluorophore this would not be a big problem, since the immobile fluorophores would quickly photobleach. However, the photoresistance of these immobile QDs allows them to contribute to background over the entire course of the measurement. Autofluorescence is another possible contributor to background, but in this study it was minimized by the

use of a long wavelength green laser for excitation. Another possible contribution to the reduced CPP seen in vivo is absorption by the body of the worm.

4.3.2 FCS curves of BSA-Alexa 555 in the oocyte could be fit with an anomalous diffusion model

In contrast to the results obtained for QDs in oocytes, BSA-Alexa 555 curves recorded in the oocyte could in most cases be well described by anomalous diffusion. These results strongly suggest that the complex QD motion observed was a characteristic of QDs, and not of all fluorophores in this particular cellular environment.

Unlike the QDs, the concentration of BSA-Alexa 555 was higher in the nucleus than in the cytoplasm, as indicated from the count rate. This is probably because BSA-Alexa 555 is about three times smaller than QDs, and so can more easily pass through the nuclear pore complexes and enter the nucleus. In a previous study in which calcium green dextran was injected into *C. elegans*, it was also found that the dye was more concentrated in the nucleus than in the cytoplasm [91]. The authors attributed this to the absence of organelles in the nucleus compared to the cytoplasm, as well as to the larger quantity of yolk particles in the cytoplasm. In contrast, studies with QDs have found that they preferentially accumulate in cytoplasm and are often excluded from the nucleus of cells [28], and that the ability of QDs to get into the nucleus indeed depends on their size [49].

The AC curves recorded for BSA-Alexa 555 in the oocyte suggest that the motion of the fluorophores in the cytoplasm is both slower and more anomalous than in the nucleus. In this respect, the results from the QDs and the BSA-Alexa 555 are consistent. Previous FCS studies carried out in cells have also reported anomalous diffusion in both the cytosol and the nucleus [76, 79, 83]. This can be appreciated by considering that the concentration of macromolecules inside a cell can be as high as 400g/l [96]. Anomalous diffusion can be caused, for instance, by binding to cell structures or by the confrontation of obstacles during diffusion, such as organelles and the cytoskeleton [97].

The CPP of BSA-Alexa 555 in both the cytoplasm and the nucleus were calculated to be lower than in solution. In this case it was clear that this resulted at least partially from an overestimation of the concentration derived from the FCS curves, since the calculated concentrations were in many cases higher than the actual injection concentration. Absorption and aggregation may again have also contributed to the decreased CPP.

One disparity between the BSA-Alexa 555 and the QD FCS curves in the oocyte is the apparent viscosity that is derived from them. The BSA-Alexa 555 AC curves suggest an oocyte viscosity that is about 20-40 times higher than that of water, while the QD curves suggest a viscosity that is 4-6 times higher. The viscosity derived from the QD curves are actually more consistent with cell viscosity values determined in other studies. These previous studies have found that the viscosity in cells is 2.6 to 10 fold higher than in aqueous solution [76]. The Xenopus oocyte has been found to have a viscosity about 2 times that of water [98]. One study specifically looked at viscosity of the early *C. elegans* embryo, and found that it was about 100 times more viscous than water [92]. However, this result relied on the motion of nanoparticles that had a radius about 5 times larger than that of the QDs used in this study. Larger particles may experience a higher apparent viscosity due to their restricted ability to maneuver in a crowded cellular environment compared to smaller probes or molecules.

There is at least one study that supports the viscosity values derived from the BSA-Alexa 555 AC curves. This recent FCS study in the one-cell *C. elegans* embryo looked at the diffusion of GFP coupled proteins involved in the first asymmetric cell division [99]. The investigators found that that the diffusion coefficient of a freely diffusing protein, CDC-37, was 4.8μm^2/sec in the cytoplasm, which is the same value that was found in this current study for BSA-Alexa- 555 in the oocyte. CDC-37 is 69kDa in size, comparable to the size of BSA-Alexa 555. However, these results are not completely comparable, as the authors of the study were able to fit their data with a simple diffusion model, as opposed to the anomalous diffusion model used here. They also noted that this diffusion coefficient was lower than what would be expected in a

cellular environment, and suggested that cytoplasmic crowding had an effect on the movement of these proteins, or that transient binding or the formation of large complexes were perhaps occurring.

These explanations may possibly account for the high apparent viscosity observed for the BSA-Alexa 555. It is possible that the motion of BSA-Alexa 555 is actually not anomalous, but rather multi-component in the oocyte. The BSA-Alexa 555 may be forming aggregates of different sizes that move at different rates. In this case, the diffusion coefficient that we calculated would be just an average of the fast and slow components, and would be an underestimate of the true diffusion coefficient of a single BSA-Alexa 555 conjugate. Indeed, from the confocal images of the oocyte seen in Figure 46, the distribution of QDs does not look uniform in the cytoplasm, and aggregation can be seen. This would be consistent with results from image analysis that show aggregates of various sizes from an early embryo stage.

Chapter 5 Conclusions

The *C. elegans* embryo was introduced here as a possible model system for studying nanotoxicity at the organism level. CdSe/ZnS carboxyl terminated QDs were found to have no significant morphological effects on *C. elegans* embryo development. As a next step, it would be interesting to follow viable embryos through to adulthood, to investigate if the worm has any mechanisms to metabolize or eliminate the QDs from its body, and also if life cycle is altered in anyway by the QDs. Preliminary experiments with unpassivated CdTe QDs suggest that these QDs cause abnormal oocyte formation, adding stalk to the argument that the passivating layer is responsible for preventing toxicity. This is worth pursuing further. It would also be interesting to measure the effects of QDs on the expression levels of stress genes in *C. elegans* by coupling these genes to GFP. *C. elegans* would again be an ideal model organism for such studies, since its genes can be easily manipulated.

The main result of this thesis is that foreign particles introduced in the *C. elegans* embryo aggregate in a concentration and time dependant manner. Two methods were used in this study to investigate this aggregation process. The first, an image analysis approach, revealed that the aggregation of QDs in the embryo is concentration dependent, with high concentrations showing a high degree of QD immobility early in development. The embryo appears to have some sort of mechanism of sequestering QDs into aggregates that reduces their mobility over embryo development.

Fluorescence correlation spectroscopy was used to investigate QD dynamics at the molecular level. To our knowledge, this is the first time that this technique has been used to study the dynamics of QDs in a cellular environment. Our results reveal the QDs experience complex motion in the oocyte environment, presumably caused by aggregation and possibly also non-specific interactions with cellular structures. To better understand the source of this interaction, different coatings need to be investigated, as

well as different functionalizing groups such as streptavidin or hydroxyl. It would also be useful to study QD dynamics in other cell types.

Although the superior photostability of QDs could potentially allow them to be used to study the dynamics of slowly moving particles using FCS, the strong interactions that they seem to experience within the cell may limit their capacity to do so. Our results suggest that caution should be observed when using QDs in single particle tracking studies, as their non-specific interactions may interfere with the function of the molecules that they are tagged to.

APPENDIX A. Image correlation plugin

```
import ij.*;
import ij.process.*;
import ij.gui.*;
import java.awt.*;
import ij.plugin.*;

public class density_correlation3 implements PlugIn {

public void run(String arg)
      {
      //check there's an image open
      int[] wList = WindowManager.getIDList();
            if (wList==null)
            {
                  IJ.error("No images are open.");
                  return;
                  }

      //set up analysis objects
      ImagePlus imp = WindowManager.getCurrentImage();
      ImageProcessor ip = imp.getProcessor();

//accessing the number of pixels in the x direction
int Ni= imp.getWidth();
```

```
//accessing the number of pixels in the y direction
int Nj= imp.getHeight();

//calculating the average intensity of the image

double intensity=0;
for (int i=0; i<Ni; i++) // start at i=0 or 1? <Ni or <=Ni?
{
      for (int j=0; j<Nj; j++)
      {
            //IJ.write("intensity at
("+i+","+j+")="+ip.getPixelValue(i,j));
            intensity=intensity+ip.getPixelValue(i,j); //

      }
}

double avgintensity=intensity/(Ni*Nj);
double avgintensity_squared=Math.pow(avgintensity,2);
IJ.write("Ni="+Ni+"  "+"Nj="+Nj);
IJ.write("total intensity="+intensity);
IJ.write("Average intensity=  " +avgintensity);

//part 1 of calculating the density density correlation function
int c=Ni*Nj;// this is the maximum number of radii values that can be
calculated
int counter=0;// this counts how many radius values have been
calculated
double intensity_product[]= new double[c]; // this array will contain
the multiplied intensities
double r[]= new double[c]; // this array will contain the radius values
double N[]=new double[c]; // this array will contain the number of
points at which the same radius occurs for each radius value

for ( int i=0; i<c; i++)
{
      intensity_product[i]=0; //fill array intensity_product with zeros
      r[i]=-1; //fill array r with -1s
      N[i]=1; //fill array N with 1s
}

for (int i=0; i<Ni; i++)
{
      for (int j=0; j<Nj; j++)
      {
            for (int i2=0; i2<Ni; i2++)
            {
                  for (int j2=0; j2<Nj; j2++)

                  {
                        double radius_squared=Math.pow((i-
i2),2)+Math.pow((j-j2),2);
                        double radius= Math.sqrt(radius_squared);
```

```
                        double densityfunc=
ip.getPixelValue(i,j)*ip.getPixelValue (i2,j2);
                        if (radius<=50)

                        {
                              if ((Nj*i2+j2>=Nj*i+j)) // This makes
sure that the correlation for the same two points isn't calculated
twice
                              {
                                    int k=-1;
                                    {
                                          do // this is necessary to
group all of the values that have the same radius value
                                          {
                                                k++;
                                                if (radius==r[k])
                                                {

      intensity_product[k]= intensity_product[k]+densityfunc;
                                                      N[k]=N[k]+1;


      //IJ.write("(i,j)=("+i+","+j+")"+"and
(i2,j2)=("+i2+","+j2+")"+"and radius="+radius);
                                                }
                                          }
                                          while ((radius!=r[k]) &&
(k<counter));

                                          if (radius!=r[k])
                                          {

      intensity_product[k] = densityfunc;
                                                      r[k]=radius;

      counter=counter+1;

      //IJ.write("(i,j)=("+i+","+j+")"+"and
(i2,j2)=("+i2+","+j2+")"+"and radius="+radius);

                                          }

                                    }
                              }
                        }
                  }
            }
      }

}
// part 2 of calculating the correlation function
double correlation[]= new double[counter];// this array contains the
density density correlation function
for (int i=0; i<counter; i++)
```

```
{

      correlation[i]=
((intensity_product[i]/N[i])/avgintensity_squared)-1;
}



//print data
IJ.write("r    " + "Correlation   " + "   N");

for (int i=0; i<counter; i++)
{
      IJ.write(r[i] + "               " + correlation[i]+ "
"+ N[i]); //write in column 1 correlation[]; write in column 2 r[];
write N[] in column 3

}
IJ.write("                                                    ");

}
}
```

APPENDIX B. A statistical comparison between the survival of embryos containing quantum dots and control embryos

Mean Survival (Standard Deviation) [Sample Size] and p-values[1]

Material Incorporated into the Embryos	**BSA Coated QDs**	p-value[2]	**Uncoated QDs**	p-value	**BSA-Alexa 555**	p-value	**None[3]**	p-value	**None**
BSA Coated QDs	0.85 (0.36) [55]	0.900	1.00 (0.00) [8]	1.000	0.85 (0.37) [26]	1.000	0.87 (0.34) [91]	0.682	0.76 (0.43) [82]
Uncoated QDs			1.00 (0.) [8]	0.903	0.85 (0.37) [26]	0.922	0.87 (0.34) [91]	0.540	0.76 (0.43) [82]
BSA-Alexa 555					0.85 (0.37) [26]	0.999	0.87 (0.34) [91]	0.886	0.76 (0.43) [82]
None[4]							0.87 (0.34) [91]	0.423	0.76 (0.43) [82]

[1] All p-values are based on Scheffé's multiple pairwise test.

[2] The p-values reflect the statistical significance between the survival metric in the **first** cell to the left in a row and the survival metric in the cell to the right in the same row. For instance, a survival rate of .85 for the BSA Coated QDs is not significantly ($p = 0.900$) less than a survival rate of 1.000 for the uncoated QDs.

[3] Non-fluorescent embryos from injected worm

[4] Non-fluorescent embryos from injected worm

APPENDIX C. FCS Results for BSA-Alexa 555

Comparison of results from three different worms on three different days

	Cytoplasm Measurements			Nucleus Measurements		
	Alpha	**Diffusion Coefficient**	**Concentration (nM)**	**Alpha**	**Diffusion Coefficient (μm^2/sec)**	**Concentration (nM)**
Day 1 N=2	0.59± 0.02	6.2±0.2	16.5±0.5	0.702± 0.006	9.5±1.5	18.6±0.2
Day 2 N=4	0.65± 0.01	1.8±0.2	600± 100	0.59± 0.04	2.1±0.6	420±60
Day 3 N=3	0.57± 0.01	6.3±0.4	230±30	0.65± 0.04	4.8±0.4	260± 70

Comparison of results obtained from a single worm

		Alpha			Diffusion Coefficient		
		Value	**% Error from Fit**	**S.E**	**Value**	**% Error from Fit**	**S.E**
Cytoplasm Measurements	Oocyte1	0.58	1.0-2.0%	0.02	7.1	3.2-6%	0.6
	Oocyte 2	0.56	1.2-2.3%	0.03	6.1	3.9-8.6%	0.3
	Oocyte 3	0.57	1.5-2.1%	0.02	5.6	4.2-7.1%	0.5
Nucleus Measurements	Oocyte1	.70	1.1-1.3%	0.01	5.4	3.4-3.5%	0.5
	Oocyte 2	.67	0.7-1%	0.02	5.1	2.7-3.2%	0.1
	Oocyte 3	.57	1.5-4.2%	0.02	4.0	5.2-10.9%	0.7

S.E = standard error

REFERENCES

1. RF Heuff, JL Swift, DT Cramb: **Fluorescence correlation spectroscopy using quantum dots: advances, challenges and opportunities.** *Phys Chem Chem Phys* 2007, **9**:1870-80.
2. XH Gao, LL Yang, JA Petros, FF Marshal, JW Simons, SM Nie: **In vivo molecular and cellular imaging with quantum dots.** *Current Opinion in Biotechnology* 2005, **16**:63-72.
3. DE Gomez, M Califano, P Mulvaney: **Optical properties of single semiconductor nanocrystals.** *Physical Chemistry Chemical Physics* 2006, **8**:4989-5011.
4. BO Dabbousi, J RodriguezViejo, FV Mikulec, JR Heine, H Mattoussi, R Ober, KF Jensen, MG Bawendi: **(CdSe)ZnS core-shell quantum dots: Synthesis and characterization of a size series of highly luminescent nanocrystallites.** *Journal of Physical Chemistry B* 1997, **101**:9463-9475.
5. AP Alivisatos: **Semiconductor clusters, nanocrystals, and quantum dots.** *Science* 1996, **271**:933-937.
6. Invitrogen: **Qdot® Nanocrystal Technology Overview.** *http://www.invitrogen.com* 2009.
7. MJ Murcia, DL Shaw, EC Long, CA Naumann: **Fluorescence correlation spectroscopy of CdSe/ZnS quantum dot optical bioimaging probes with ultra-thin biocompatible coatings.** *Optics Communications* 2008, **281**:1771-1780.
8. X Michalet, FF Pinaud, LA Bentolila, JM Tsay, S Doose, JJ Li, G Sundaresan, AM Wu, SS Gambhir, S Weiss: **Quantum dots for live cells, in vivo imaging, and diagnostics.** *Science* 2005, **307**:538-44.
9. AM Iga, JH Robertson, MC Winslet, AM Seifalian: **Clinical potential of quantum dots.** *J Biomed Biotechnol* 2007, **2007**:76087.
10. IL Medintz, HT Uyeda, ER Goldman, H Mattoussi: **Quantum dot bioconjugates for imaging, labelling and sensing.** *Nature Materials* 2005, **4**:435-446.
11. JK Jaiswal, SM Simon: **Potentials and pitfalls of fluorescent quantum dots for biological imaging.** *Trends in Cell Biology* 2004, **14**:497-504.
12. M Warnement, S Rosenthal: **Fluorescent Quantum Dots: Properties and Applications.** In: *Fluorescence Spectroscopy in Biology*, vol. 3. pp. 263-274: Springer Berlin Heidelberg; 2005: 263-274.
13. DR Larson, WR Zipfel, RM Williams, SW Clark, MP Bruchez, FW Wise, WW Webb: **Water-soluble quantum dots for multiphoton fluorescence imaging in vivo.** *Science* 2003, **300**:1434-1436.

14. WCW Chan, DJ Maxwell, XH Gao, RE Bailey, MY Han, SM Nie: **Luminescent quantum dots for multiplexed biological detection and imaging.** *Current Opinion in Biotechnology* 2002, **13**:40-46.
15. U Resch-Genger, M Grabolle, S Cavaliere-Jaricot, R Nitschke, T Nann: **Quantum dots versus organic dyes as fluorescent labels.** *Nature Methods* 2008, **5**:763-775.
16. Invitrogen: **"Fluorescence Spectra Viewer".** In: *Book "Fluorescence Spectra Viewer"* (Editor ed.^eds.). City; 2008.
17. F Pinaud, X Michalet, LA Bentolila, JM Tsay, S Doose, JJ Li, G Iyer, S Weiss: **Advances in fluorescence imaging with quantum dot bio-probes.** *Biomaterials* 2006, **27**:1679-1687.
18. J Conroy, SJ Byrne, YK Gun'ko, YP Rakovich, JF Donegan, A Davies, D Kelleher, Y Volkov: **CdTe Nanoparticles Display Tropism to Core Histones and Histone-Rich Cell Organelles.** *Small* 2008, **4**:2006-2015.
19. M Dahan, T Laurence, F Pinaud, DS Chemla, AP Alivisatos, M Sauer, S Weiss: **Time-gated biological imaging by use of colloidal quantum dots.** *Opt Lett* 2001, **26**:825-7.
20. JA Kloepfer, SE Bradforth, JL Nadeau: **Photophysical properties of biologically compatible CdSe quantum dot structures.** *Journal of Physical Chemistry B* 2005, **109**:9996-10003.
21. HE Grecco, KA Lidke, R Heintzmann, DS Lidke, C Spagnuolo, OE Martinez, EA Jares-Erijman, TM Jovin: **Ensemble and single particle photophysical properties (Two-Photon excitation, anisotropy, FRET, lifetime, spectral conversion) of commercial quantum dots in solution and in live cells.** *Microscopy Research and Technique* 2004, **65**:169-179.
22. M Nirmal, BO Dabbousi, MG Bawendi, JJ Macklin, JK Trautman, TD Harris, LE Brus: **Fluorescence intermittency in single cadmium selenide nanocrystals.** *Nature* 1996, **383**:802-804.
23. MA Hines, P Guyot-Sionnest: **Synthesis and characterization of strongly luminescing ZnS-Capped CdSe nanocrystals.** *Journal of Physical Chemistry* 1996, **100**:468-471.
24. WCW Chan, SM Nie: **Quantum dot bioconjugates for ultrasensitive nonisotopic detection.** *Science* 1998, **281**:2016-2018.
25. S Hohng, T Ha: **Near-complete suppression of quantum dot blinking in ambient conditions.** *Journal of the American Chemical Society* 2004, **126**:1324-1325.
26. M Kuno, DP Fromm, HF Hamann, A Gallagher, DJ Nesbitt: **Nonexponential "blinking" kinetics of single CdSe quantum dots: A universal power law behavior.** *Journal of Chemical Physics* 2000, **112**:3117-3120.
27. WB Cai, AR Hsu, ZB Li, XY Chen: **Are quantum dots ready for in vivo imaging in human subjects?** *Nanoscale Research Letters* 2007, **2**:265-281.
28. FQ Chen, D Gerion: **Fluorescent CdSe/ZnS nanocrystal-peptide conjugates for long-term, nontoxic imaging and nuclear targeting in living cells.** *Nano Letters* 2004, **4**:1827-1832.

29. M Dahan, S Levi, C Luccardini, P Rostaing, B Riveau, A Triller: **Diffusion dynamics of glycine receptors revealed by single-quantum dot tracking.** *Science* 2003, **302**:442-445.
30. BX Cui, CB Wu, L Chen, A Ramirez, EL Bearer, WP Li, WC Mobley, S Chu: **One at a time, live tracking of NGF axonal transport using quantum dots.** *Proceedings of the National Academy of Sciences of the United States of America* 2007, **104**:13666-13671.
31. B Ballou, BC Lagerholm, LA Ernst, MP Bruchez, AS Waggoner: **Noninvasive imaging of quantum dots in mice.** *Bioconjugate Chemistry* 2004, **15**:79-86.
32. ME Akerman, WCW Chan, P Laakkonen, SN Bhatia, E Ruoslahti: **Nanocrystal targeting in vivo.** *Proceedings of the National Academy of Sciences of the United States of America* 2002, **99**:12617-12621.
33. XH Gao, YY Cui, RM Levenson, LWK Chung, SM Nie: **In vivo cancer targeting and imaging with semiconductor quantum dots.** *Nature Biotechnology* 2004, **22**:969-976.
34. ACS Samia, XB Chen, C Burda: **Semiconductor quantum dots for photodynamic therapy.** *Journal of the American Chemical Society* 2003, **125**:15736-15737.
35. SK Chakraborty, JAJ Fitzpatrick, JA Phillippi, S Andreko, AS Waggoner, MP Bruchez, B Ballou: **Cholera toxin B conjugated quantum dots for live cell Labeling.** *Nano Letters* 2007, 7:2618-2626.
36. JK Jaiswal, H Mattoussi, JM Mauro, SM Simon: **Long-term multiple color imaging of live cells using quantum dot bioconjugates.** *Nature Biotechnology* 2003, **21**:47-51.
37. AM Derfus, WCW Chan, SN Bhatia: **Intracellular delivery of quantum dots for live cell labeling and organelle tracking.** *Advanced Materials* 2004, **16**:961-+.
38. B Dubertret, P Skourides, DJ Norris, V Noireaux, AH Brivanlou, A Libchaber: **In vivo imaging of quantum dots encapsulated in phospholipid micelles.** *Science* 2002, **298**:1759-1762.
39. S Rieger, RP Kulkarni, D Darcy, SE Fraser, RW Koster: **Quantum dots are powerful multipurpose vital labeling agents in zebrafish embryos.** *Dev Dyn* 2005, **234**:670-81.
40. S Courty, C Luccardini, Y Bellaiche, G Cappello, M Dahan: **Tracking individual kinesin motors in living cells using single quantum-dot imaging.** *Nano Lett* 2006, **6**:1491-5.
41. T Jamieson, R Bakhshi, D Petrova, R Pocock, M Imani, AM Seifalian: **Biological applications of quantum dots.** *Biomaterials* 2007, **28**:4717-4732.
42. D Maysinger, J Lovric, A Eisenberg, R Savic: **Fate of micelles and quantum dots in cells.** *European Journal of Pharmaceutics and Biopharmaceutics* 2007, **65**:270-281.
43. C Kirchner, T Liedl, S Kudera, T Pellegrino, AM Javier, HE Gaub, S Stolzle, N Fertig, WJ Parak: **Cytotoxicity of colloidal CdSe and CdSe/ZnS nanoparticles.** *Nano Letters* 2005, **5**:331-338.

44. M Kondoh, S Araragi, K Sato, M Higashimoto, M Takiguchi, M Sato: **Cadmium induces apoptosis partly via caspase-9 activation in HL-60 cells.** *Toxicology* 2002, **170**:111-117.
45. L Braydich-Stolle, S Hussain, JJ Schlager, MC Hofmann: **In vitro cytotoxicity of nanoparticles in mammalian germline stem cells.** *Toxicological Sciences* 2005, **88**:412-419.
46. N Lewinski, V Colvin, R Drezek: **Cytotoxicity of nanoparticles.** *Small* 2008, **4**:26-49.
47. AM Derfus, WCW Chan, SN Bhatia: **Probing the cytotoxicity of semiconductor quantum dots.** *Nano Letters* 2004, **4**:11-18.
48. WH Chan, NH Shiao, PZ Lu: **CdSe quantum dots induce apoptosis in human neuroblastoma cells via mitochondrial-dependent pathways and inhibition of survival signals.** *Toxicology Letters* 2006, **167**:191-200.
49. J Lovric, H Bazzi, Y Cuie, G Fortin, F Winnik, D Maysinger: **Differences in subcellular distribution and toxicity of green and red emitting CdTe quantum dots.** *Journal of Molecular Medicine* 2005, **83**:377-385.
50. JP Ryman-Rasmussen, JE Riviere, NA Monteiro-Riviere: **Surface coatings determine cytotoxicity and irritation potential of quantum dot nanoparticles in epidermal keratinocytes.** *Journal of Investigative Dermatology* 2007, **127**:143-153.
51. E Chang, N Thekkek, WW Yu, VL Colvin, R Drezek: **Evaluation of quantum dot cytotoxicity based on intracellular uptake.** *Small* 2006, **2**:1412-1417.
52. A Shiohara, A Hoshino, K Hanaki, K Suzuki, K Yamamoto: **On the cyto-toxicity caused by quantum dots.** *Microbiology and Immunology* 2004, **48**:669-675.
53. J Lovric, SJ Cho, FM Winnik, D Maysinger: **Unmodified cadmium telluride quantum dots induce reactive oxygen species formation leading to multiple organelle damage and cell death.** *Chemistry & Biology* 2005, **12**:1227-1234.
54. HC Fischer, WCW Chan: **Nanotoxicity: the growing need for in vivo study.** *Current Opinion in Biotechnology* 2007, **18**:565-571.
55. S Rieger, RP Kulkarni, D Darcy, SE Fraser, RW Koster: **Quantum dots are powerful multipurpose vital labeling agents in zebrafish embryos.** *Developmental Dynamics* 2005, **234**:670-681.
56. WH Chan, NH Shiao: **Cytotoxic effect of CdSe quantum dots on mouse embryonic development.** *Acta Pharmacologica Sinica* 2008, **29**:259-266.
57. R Hardman: **A toxicologic review of quantum dots: Toxicity depends on physicochemical and environmental factors.** *Environmental Health Perspectives* 2006, **114**:165-172.
58. V Karabanovas, E Zakarevicius, A Sukackaite, G Streckyte, R Rotomskis: **Examination of the stability of hydrophobic (CdSe)ZnS quantum dots in the digestive tract of rats.** *Photochemical & Photobiological Sciences* 2008, **7**:725-729.
59. JE Sulston, E Schierenberg, JG White, JN Thomson: **The Embryonic-Cell Lineage of the Nematode Caenorhabditis-Elegans.** *Developmental Biology* 1983, **100**:64-119.
60. Z Altun, D Hall: **Handbook of C. elegans Anatomy.** *WormAtlas. http://www. wormatlas. org/handbook/contents. htm* 2005.

61. D Greenstein: **Control of oocyte meiotic maturation and fertilization.** *WormBook: online reveiw of C. elegans biology, TCeR Community, ed.(http://www. wormbook. org)* 2005.
62. I Yamamoto, ME Kosinski, D Greenstein: **Start me up: Cell signaling and the journey from oocyte to embryo in C-elegans.** *Developmental Dynamics* 2006, **235**:571-585.
63. LS Rose, KJ Kemphues: **Early patterning of the C-elegans embryo.** *Annual Review of Genetics* 1998, **32**:521-545.
64. S Brenner: **The genetics of Caenorhabditis elegans.** *Genetics* 1974, 77:71-94.
65. MCK Leung, PL Williams, A Benedetto, C Au, KJ Helmcke, M Aschner, JN Meyer: **Caenorhabditis elegans: An emerging model in biomedical and environmental toxicology.** *Toxicological Sciences* 2008, **106**:5-28.
66. KW Chu, SKW Chan, KL Chow: **Improvement of heavy metal stress and toxicity assays by coupling a transgenic reporter in a mutant nematode strain.** *Aquatic Toxicology* 2005, **74**:320-332.
67. JY Roh, J Lee, J Choi: **Assessment of stress-related gene expression in the heavy metal-exposed nematode Caenorhabditis elegans: A potential biomarker for metal-induced toxicity monitoring and environmental risk assessment.** *Environmental Toxicology and Chemistry* 2006, **25**:2946-2956.
68. DY Wang, XJ Xing: **Assessment of locomotion behavioral defects induced by acute toxicity from heavy metal exposure in nematode Caenorhabditis elegans.** *Journal of Environmental Sciences-China* 2008, **20**:1132-1137.
69. O Krichevsky, G Bonnet: **Fluorescence correlation spectroscopy: the technique and its applications.** *Reports on Progress in Physics* 2002, **65**:251-297.
70. S Maiti, U Haupts, WW Webb: **Fluorescence correlation spectroscopy: Diagnostics for sparse molecules.** *Proceedings of the National Academy of Sciences of the United States of America* 1997, **94**:11753-11757.
71. SA Kim, KG Heinze, P Schwille: **Fluorescence correlation spectroscopy in living cells.** *Nature Methods* 2007, **4**:963-973.
72. ST Hess, S Huang, AA Heikal, WW Webb: **Biological and chemical applications of fluorescence correlation spectroscopy: a review.** *Biochemistry* 2002, **41**:697-705.
73. MA Medina, P Schwille: **Fluorescence correlation spectroscopy for the detection and study of single molecules in Biology.** *Bioessays* 2002, **24**:758-764.
74. M Hof, R Hutterer, V Fidler: **Fluorescence Spectroscopy In Biology: Advanced Methods And Their Applications To Membranes, Proteins, Dna, And Cells.** In: *Springer Series on Fluorescence*, vol. 3. pp. 245-262: Springer Berlin Heidelberg; 2005: 245-262.
75. P Dittrich, F Malvezzi-Campeggi, M Jahnz, P Schwille: **Accessing molecular dynamics in cells by fluorescence correlation spectroscopy.** *Biological Chemistry* 2001, **382**:491-494.
76. M Wachsmuth, W Waldeck, J Langowski: **Anomalous diffusion of fluorescent probes inside living cell nuclei investigated by spatially-resolved fluorescence correlation spectroscopy.** *Journal of Molecular Biology* 2000, **298**:677-689.

77. RH Kohler, P Schwille, WW Webb, MR Hanson: **Active protein transport through plastid tubules: velocity quantified by fluorescence correlation spectroscopy**. *Journal of Cell Science* 2000, **113**:3921-3930.
78. K Bacia, SA Kim, P Schwille: **Fluorescence cross-correlation spectroscopy in living cells**. *Nature Methods* 2006, **3**:83-89.
79. P Schwille, U Haupts, S Maiti, WW Webb: **Molecular dynamics in living cells observed by fluorescence correlation spectroscopy with one- and two-photon excitation**. *Biophys J* 1999, **77**:2251-65.
80. MJ Booth, MAA Neil, T Wilson: **Aberration correction for confocal imaging in refractive-index-mismatched media**. *Journal of Microscopy-Oxford* 1998, **192**:90-98.
81. E Keating, CM Brown, NO Petersen: **Mapping Molecular Interactions and Transport in Cell Membranes by Image Correlation Spectroscopy**. In: *Molecular Imaging: FRET Microscopy and Spectroscopy*. pp. 284-301: Oxford University Press; 2005: 284-301.
82. Z Petrasek, P Schwille: **Precise measurement of diffusion coefficients using scanning fluorescence correlation spectroscopy**. *Biophysical Journal* 2008, **94**:1437-1448.
83. M Weiss: **Probing the interior of living cells with fluorescence correlation spectroscopy**. *Fluorescence Methods and Applications: Spectroscopy, Imaging, and Probes* 2008, **1130**:21-27.
84. S Doose, JM Tsay, F Pinaud, S Weiss: **Comparison of photophysical and colloidal properties of biocompatible semiconductor nanocrystals using fluorescence correlation spectroscopy**. *Analytical Chemistry* 2005, **77**:2235-2242.
85. JA Rochira, MV Gudheti, TJ Gould, RR Laughlin, JL Nadeau, ST Hess: **Fluorescence intermittency limits brightness in CdSe/ZnS nanoparticles quantified by fluorescence correlation spectroscopy**. *Journal of Physical Chemistry C* 2007, **111**:1695-1708.
86. AI Bachir, DL Kolin, KG Heinze, B Hebert, PW Wiseman: **A guide to accurate measurement of diffusion using fluorescence correlation techniques with blinking quantum dot nanoparticle labels**. *Journal of Chemical Physics* 2008, **128**.
87. WW Webb: **Fluorescence correlation spectroscopy: inception, biophysical experimentations, and prospectus**. *Applied Optics* 2001, **40**:3969-3983.
88. MA Digman, CM Brown, P Sengupta, PW Wiseman, AR Horwitz, E Gratton: **Measuring fast dynamics in solutions and cells with a laser scanning microscope**. *Biophysical Journal* 2005, **89**:1317-1327.
89. CM Brown, RB Dalal, B Hebert, MA Digman, AR Horwitz, E Gratton: **Raster image correlation spectroscopy (RICS) for measuring fast protein dynamics and concentrations with a commercial laser scanning confocal microscope**. *Journal of Microscopy-Oxford* 2008, **229**:78-91.
90. A Aleksandrov, M Trakhtengerts: **Viscosity of water at temperatures of- 20 to 150° C**. *Journal of Engineering Physics and Thermophysics* 1974, **27**:1235-1239.
91. A Samuel, V Murthy, M Hengartner: **Calcium dynamics during fertilization in C. elegans**. *BMC Developmental Biology* 2001, **1**:8.

92. BR Daniels, BC Masi, D Wirtz: **Probing single-cell micromechanics in vivo: the microrheology of C. elegans developing embryos.** *Biophys J* 2006, **90**:4712-9.
93. S Doose, JM Tsay, F Pinaud, S Weiss: **Comparison of photophysical and colloidal properties of biocompatible semiconductor nanocrystals using fluorescence correlation spectroscopy.** *Anal Chem* 2005, **77**:2235-42.
94. J Swift, R Heuff, D Cramb: **A Two-Photon Excitation Fluorescence Cross-Correlation Assay for a Model Ligand-Receptor Binding System Using Quantum Dots.** *Biophysical Journal* 2006, **90**:1396-1410.
95. S Pathak, SK Choi, N Arnheim, ME Thompson: **Hydroxylated quantum dots as luminescent probes for in situ hybridization.** *Journal of the American Chemical Society* 2001, **123**:4103-4104.
96. RJ Ellis, AP Minton: **Cell biology - Join the crowd.** *Nature* 2003, **425**:27-28.
97. SA Kim, KG Heinze, P Schwille: **Fluorescence correlation spectroscopy in living cells.** *Nat Methods* 2007, **4**:963-73.
98. JV Sehy, JJH Ackerman, JJ Neil: **Apparent diffusion of water, ions, and small molecules in the Xenopus oocyte is consistent with Brownian displacement.** *Magnetic Resonance in Medicine* 2002, **48**:42-51.
99. Z Petrasek, C Hoege, A Mashaghi, T Ohrt, AA Hyman, P Schwille: **Characterization of Protein Dynamics in Asymmetric Cell Division by Scanning Fluorescence Correlation Spectroscopy.** *Biophysical Journal* 2008, **95**:5476-5486.